THE IMPACT OF AEROSOLS ON CONVECTIVE CLOUDS:

A GLOBAL PERSPECTIVE

by

Christina L. Wall

A dissertation submitted to the faculty of
The University of Utah
in partial fulfillment of the requirements for the degree of

Doctor of Philosophy

Department of Atmospheric Sciences

The University of Utah

May 2013

The University of Utah Graduate School

STATEMENT OF DISSERTATION APPROVAL

The dissertation of **Christina L Wall**

has been approved by the following supervisory committee members:

Edward J. Zipser	, Chair	**February 14, 2013** Date Approved
Susan van den Heever	, Member	**February 14, 2013** Date Approved
Gerald G. Mace	, Member	**February 14, 2013** Date Approved
Timothy J. Garrett	, Member	**February 14, 2013** Date Approved
Steven K. Krueger	, Member	**February 14, 2013** Date Approved

and by **Kevin Perry**, Chair of the Department of **Atmospheric Sciences**

and by Donna M. White, Interim Dean of The Graduate School.

ABSTRACT

Many studies have examined both the modeling and observational aspects of aerosol-cloud interactions. The effect of the surrounding environment on individual clouds makes it difficult to isolate the signal of invigoration or suppression by aerosols, particularly at larger spatial and temporal scales. This study uses observations from the Tropical Rainfall Measuring Mission (TRMM), CloudSat, and Aqua satellites to identify convective clouds systems in clean and dirty environments.

The MODerate Resolution Imaging Spectroradiometer (MODIS) aerosol index is collocated with radar precipitation features (RPFs) from TRMM and congestus cloud features (CFs) from CloudSat. Congestus clouds are also defined using Visible and Infrared Scanner (VIRS) infrared brightness temperature and radar-detected surface rainfall from 14 years of TRMM data. Using these definitions, the regional and seasonal variations of the population of congestus are presented globally. General differences are found between the properties of congestus over land and over ocean, especially the shapes of congestus. Ocean congestus are more bell-shaped, while land congestus tend to have flatter sides and larger area above the freezing level. This population of congestus is then used to examine the characteristics of clouds occurring in clean and dirty environments in different parts of the world.

The ERA-Interim, which is paired with RPFs and CFs, is used to examine the environment in which these clouds occur. Aerosols are found to have different effects on clouds in different parts of the world. In some regions, such as Africa, environmental differences could possibly explain "invigoration" that has been attributed to aerosol effects. In other regions, such as the Amazon, environmental differences between clean and dirty cloud features remain small, indicating that aerosols could be causing at least part of the observed differences in cloud properties.

Differences in clean and dirty congestus are very small and are limited to differences in the profiles of maximum reflectivity. The signal of the aerosol indirect effect is so small that it is very difficult to detect confidently using these methods. The environment must be considered in any study of the aerosol indirect effect, as important environmental changes can occur as aerosols are introduced to an air mass.

TABLE OF CONTENTS

ACKNOWLEDGEMENTS

I would like to give profound thanks to my advisor, Dr. Ed Zipser, for his support during the course of this project. His guidance and encouragement has been paramount to my growth as a scientist over the last 6 years. I would also like to thank the other members of my committee, Dr. Jay Mace, Dr. Sue van den Heever, Dr. Tim Garrett, and Dr. Steve Krueger. Their insights on the complex relationships between aerosols and clouds have been immensely helpful. Dr. Chuntao Liu has been an integral part of both learning the data management skills I needed to help produce the CloudSat Database and discussions about ideas. I would also like to thank Dr. Courtenay Strong for his help with choosing appropriate statistical tests for the data. Dr. van den Heever's research group has been incredibly supportive of my results and provided very useful discussion. Emily Riley and Aaron Kennedy have also provided invaluable support by critiquing figures and discussing IDL. Thanks to Dan Tyndall for help with the intricacies of the Word page numbering system.

This work was funded by NASA Grant # NNX07AD61G. CloudSat Data were obtained from the CloudSat Data Processing Center (http://www.CloudSat.cira.colostate.edu/), and MODIS data were obtained from LAADS (http://ladsweb.nascom.nasa.gov/data/).

CHAPTER 1

INTRODUCTION

The impact of aerosols on the microphysical and dynamic properties of clouds has been much debated since the first and second aerosol indirect effects were introduced by Twomey (1977) and Albrecht (1989). The first aerosol indirect effect states that higher aerosol concentrations lead to a larger population of cloud condensation nuclei (CCN), which produce smaller cloud drops for a cloud with a given liquid water content. Albrecht (1989) extended this hypothesis by theorizing that the increase in CCN could lead to a decrease in precipitation through reduced collision and coalescence processes and cause more reflective clouds due to smaller drop sizes and an increase in liquid water path (LWP) caused by precipitation suppression. Many studies have examined both the modeling and observational side of aerosol-cloud interactions. So far the overwhelming result can be summed up in this statement from Khain (2009): "The effects of aerosols on precipitation is a very complicated multi-scale problem."

Effects of Aerosols

This problem can be addressed in a multitude of ways. Aerosols are known to affect the climate through the absorption and scattering of solar radiation and also

through the modification of cloud properties such as cloud drop size distribution, which can increase the reflectance of the cloud (Twomey 1977, van den Heever et al. 2011). The effects of aerosols on microphysical and dynamical processes that affect precipitation production are equally important, particularly when attempting to determine possible changes in the hydrologic cycle due to increasing amounts of aerosols and particulates in the atmosphere. The effects of aerosols on warm rain and shallow clouds have been studied considerably, through both observations and modeling. In most cases, aerosols suppress warm rain (Khain et al 2005, Berg et al. 2008, Rosenfeld et al. 2008, Koren et al. 2012) and reduce liquid water path (van den Heever et al 2011). This phenomenon has been observed in the Amazon due to smoke from biomass burning (Rosenfeld 1999, Khain et al 2008). Unfortunately the effect of aerosols on deep convection is much more complicated. *The objective of this study is to quantify the indirect effect of aerosols on convective clouds using satellite observations, if such an aerosol signal can be observed.*

The theoretical basis of the aerosol indirect effect on the warm rain process is relatively straightforward- greater amounts of aerosol can increase the number of CCN, which changes the drop size distribution (DSD) of the cloud by spreading the available cloud water among a larger number of CCN, creating more cloud drops with a smaller radius. Several global studies have found decreasing cloud drop effective radius to increasing column-integrated aerosol amount (Sekiguchi et al. 2003). This decrease of drop size can alter the autoconversion of cloud droplets to rain or drizzle, thereby suppressing precipitation and increasing the total liquid water content of the polluted cloud compared to a clean cloud, as less water is falling out of the cloud as rain (Gunn

and Phillips 1957, Lebsock et al. 2008, Lee et al. 2008). Activation of CCN is influenced by updraft velocity (Massie et al 2007), and most droplets form in convective updrafts just above cloud base and continue growing with height (Rosenfeld and Feingold 2003). Modeling studies show that the effect of these aerosols that penetrate the cloud from the cloud base via the updraft exceeds that of any aerosols entrained into the cloud from the sides (Khain and Pokrovsky 2004, Khain et al. 2005, van den Heever et al. 2006, Chen et al. 2011), but the effect of entrained aerosols at higher levels likely depends on the width of the storm core. The exact path that aerosols take during ingestion by a deep convective storm remains unknown and is a strong function of the background aerosol concentration (Siegel and van den Heever 2012). Mid-tropospheric aerosol concentrations can influence the properties of the anvils of convective clouds, and in Fridlind et al. (2004) aerosols up to the 10 km level had to be included in simulations to match observations from convective clouds in Florida.

Continental clouds have, on average, cloud droplets with radii 2-3 μm smaller than maritime clouds (Squires 1956, Han et al. 1994) as well as a narrower distribution of drop sizes (Khain and Pokrovsky 2004). Effective radius of the cloud droplets is a function of cloud depth, as long as the cloud is not precipitating: cloud droplets grow by diffusion as they ascend above cloud base, at least until reaching higher levels where ice processes and coalescence can accelerate droplet growth (Rosenfeld and Lensky 1998).. Because of the microphysical differences between continental and oceanic clouds, continental clouds are often used as a proxy for polluted clouds. Continental clouds tend to have a well-developed zone of diffusional growth of cloud droplets, but in maritime clouds, coalescense dominates (Rosenfeld and Lensky 1998). Among clouds with the

same cloud top height, Khain et al (2005) found that single maritime clouds produced larger amounts of accumulated rain when compared to continental clouds. Maritime clouds are affected by a greater amount of water loading in the updraft as the liquid water content of the cloud increases (Khain et al. 2005). The smaller cloud droplets found in continental clouds or clouds in an aerosol-rich environment are inefficient in collision and coalescence due to their narrow size spectrum, correspondingly lower fall speeds, and therefore smaller collision efficiency (Tao et al. 2012), while the coalescence that occurs in maritime clouds is more favorable for producing drops large enough to rain. Clouds with continental characteristics must condense a greater amount of water to produce precipitation (Lebsock et al. 2008).

The duration of convective clouds can also be affected by aerosol amount. Clouds that form in clean environments with a low concentration of CCN can rain out too quickly to develop into long-lasting storms. Formation of clouds in a dirty environment can be suppressed due to reduced surface heating from the aerosol haze layer (Koren et al. 2008, Rosenfeld et al. 2008). If they are not suppressed, polluted clouds can either evaporate too much of their water before precipitation can form (Rosenfeld et al. 2008), or ultimately the greater concentration of cloud condensation nuclei and the increased LWP can lead to more precipitation at the surface (Khain et al. 2005, Berg et al. 2008, van den Heever et al. 2006, van den Heever et al. 2011) and more intense rain rates (Khain et al. 2008, Koren et al. 2012, Storer and van den Heever 2013) later in the cloud's lifetime.

The microphysical changes that occur due to increased aerosol concentration, in turn, produce changes in storm dynamics. As a larger number of cloud drops within a

polluted cloud freeze, more latent heat is released, which strengthens the updraft (Zipser 2003), causing higher cloud tops and a greater likelihood for overshooting tops (Rosenfeld 1999, Andreae et al. 2004, Rosenfeld et al. 2007 Morrison and Grabowski 2011). This dynamic response has been observed in models as increases in both updraft speed and frequency (Khain and Pokrovsky 2004, van den Heever et al. 2006, van den Heever et al. 2011, Storer and van den Heever 2013).

Several observational studies have looked at the effects of aerosols in individual regions of the world, typically during specific time periods. Lin et al. (2006) found that an increase in MODIS aerosol optical depth was correlated with an increase in precipitation, increased occurrence of intense rain events, enhanced cloud cover, elevated cloud top heights, increased water path, and greater formation of ice in the Brazilian Amazon during the burning seasons (August-October) of 2000 and 2003. Rosenfeld (1999) also saw suppression of warm rain in observations of smoky clouds and an abundance of precipitation in observations of relatively smoke-free clouds in the Amazon during biomass burning. Khain et al. (2005) found that increasing the concentration of CCN tends to invigorate convection, increasing cloud top height and cloud lifetime in their numerical model. Jiang et al. (2008) linked polluted clouds during the dry season in South America to suppressed precipitation and reduced effective radius of cloud droplets. Sekiguchi et al. (2003) found that, while summer pollution in China significantly suppresses the growth of cloud particles, the correlation between cloud top temperature and aerosol number concentration can be positive or negative depending on season and location. Heiblum et al. (2012) use TRMM to find invigoration of the vertical distribution of rain with increasing MODIS aerosol optical depth. Berg et al. (2006) and Berg et al.

(2008) attributed differences in rainfall between two products from the Tropical Rainfall Measuring Mission (TRMM) to the effect of aerosols (observed using MODIS and modeled with SPRINTARS). Huang et al. (2009) found significant negative correlations between aerosols and precipitation in both observations and model simulations in Africa. Koren et al. (2005) and Koren et al. (2010) found that higher aerosol concentrations overall influence the distribution of clouds in the tropical Atlantic towards higher clouds and larger cloud fractions.

Effects of Thermodynamic Environment and Shear

What ultimately causes the differences in cloud characteristics and precipitation in clouds in clean and dirty environments? Khain et al. (2008) and Khain (2009) describe the change in precipitation using the following formula:

$$P=\Delta G+\Delta L \quad (1)$$

where G represents the condensate generation from condensation and ice deposition, and L represents the condensate loss from evaporation and ice sublimation. Environment affects these terms via amount of aerosols, instability, wind shear, and cloud structure (Khain et al. 2008). In clouds developing in polluted air, both ΔG and ΔL terms are larger than for clouds developing in clean air (Khain 2009, van den Heever et al. 2011), but whether a cloud will produce more or less precipitation depends on the size of ΔG compared to ΔL (Khain et al. 2008, Lee 2011). Which term increases more with increasing aerosol concentration depends on the environment, particularly humidity. In a

moister environment, ΔG increases dramatically, but ΔL increases less, as fewer drops evaporate (Khain et al. 2005, Khain 2009). A drier environment can increase ΔL due to faster evaporation (Khain et al. 2005, Berg et al. 2008, Khain 2009, Lee 2011). Thus, environment plays a significant role in determining the effect of increased aerosol concentration on convection.

Humidity and shear are two of the most important parameters in determining dynamic differences (Khain 2009). In the case of an isolated deep convective cloud in a relatively dry environment, increasing wind shear can increase entrainment and detrainment, which could increase the evaporation of both cloud droplets and large hydrometeors, decreasing precipitation (Khain et al. 2005, Lee et al. 2008, Tao et al. 2007, Fan et al. 2009). It is well known that CAPE and wind shear are related to storm type (Bluestein 1993), but how does aerosol change the magnitude of the roles of these parameters in storm development? Shear at any altitude in the convective layer has some effect on convective organization (Robe and Emmanuel 2001). As shear increases, convection generally becomes more organized (Rotunno et al. 1988, Bluestein 1993, Robe and Emmanuel 2001), and Robe and Emmanuel (2001) found that without shear, convection in their cloud ensemble model remains randomly organized. Thus, shear affects both the organization of convection, which alone can determine the effects of aerosols (Seifert and Beheng 2006, Khain 2009), and the degree of evaporation and thus condensate loss as hydrometeors are transported to regions of drier air. Lee et al. (2008) found that both reduced wind shear and very strong wind shear in their model resulted in less organized convection with a smaller difference in precipitation between high and low

aerosol runs. Fan et al. (2009) also found suppression (invigoration) of convection by aerosols in strong (weak) wind shear in regimes of both high and low CAPE.

Instability also plays a role in how much convection can change due to increased aerosol loading. All other factors being equal, an increase in instability increases the vertical velocity in the cloud, transporting more cloud water to higher levels (Khain et al. 2008), and activating more aerosols (Massie et al 2007). Lee et al. (2008) use a series of runs of the Weather Research and Forecasting (WRF) model to investigate the roles of CAPE and shear in clouds with and without an increased aerosol concentration and determine that in clouds with high CAPE and weak shear, the transport of cloud liquid to unsaturated areas is less efficient, thus reducing evaporation. Lower CAPE tends to reduce vertical velocity, which reduces supersaturation and results in a smaller cloud droplet number concentration (Lee et al. 2008). Lee et al. (2008) also found that the percent difference in precipitation production between the high and low aerosol runs was largest for very low values of CAPE. Convection with higher CAPE generally extends higher into the atmosphere, allowing hydrometeors to reach greater heights and potentially produce stronger downdrafts due to increased evaporation, which can induce low-level convergence and new convection. Storer et al. (2010) examine the relative impacts of CAPE and aerosol loading in a numerical model and find that properties of the cloud, such as cloud droplet sizes and cloud water path, are more sensitive to CCN concentration, while changes in storm strength and precipitation are more sensitive to CAPE.

Relative humidity affects the relationship between aerosols and convection and can significantly change rainfall amount (Khain et al. 2005, Fan et al. 2007, Fan et al.

2009, Khain 2009, Yuan et al. 2011). Khain et al. (2008) found that a 10% decrease in relative humidity led to a dramatic decrease in precipitation in one of their model runs. A drier environment will result in greater evaporation, while larger values of relative humidity lead to less evaporation (Lee et al. 2008). More evaporation of hydrometeors can lead to stronger downdrafts, more convergence in the boundary layer, and the formation of secondary clouds and convection (Khain et al. 2004, Khain et al. 2005, van den Heever and Cotton 2007, Storer et al. 2010, Lee 2011). Under wetter conditions an increase in aerosol concentration can lead to precipitation enhancement in areas of high instability. A decrease in precipitation was found in dry, unstable environments (Khain et al. 2008). Ultimately, in drier environments it becomes more likely that ΔL will be larger than ΔG as a result of greater evaporation; however, decreasing humidity does not necessarily lead to precipitation suppression (Lee et al. 2011).

The combination of environmental parameters is ultimately what determines the balance between ΔG and ΔL, and therefore, whether precipitation enhancement or suppression will result from an increased aerosol concentration. Lee et al. (2008) state that an increase in aerosol loading leads to an increase in precipitation in the case of high relative humidity, strong shear, and instability. Fan et al. (2009) determine that aerosols have the greatest potential to suppress convection when wind shear is strong in humid areas. Stronger updrafts and greater condensation due to high aerosol concentration is closely linked to the low-level convergence field (Khain et al. 2005, Lee et al. 2008). An increase in aerosol concentration has also been linked to a greater amount of graupel and hail in modeling studies (Khain et al. 2008, van den Heever et al. 2006, Storer et al. 2010). Lee et al. (2008) disclose that interactions between microphysics and dynamics are

stronger in a high aerosol model run because more cloud liquid is transported to unsaturated areas, resulting in more evaporation, stronger downdrafts, more convergence at the surface, and then more updrafts and condensation via secondary convection.

In many cases aerosols are not the most important piece of the puzzle in determining precipitation efficiency and convective properties (Khain et al. 2005, Khain 2009). Van den Heever et al. (2011) found that in their radiative convective equilibrium (RCE) model, large-scale controls associated with radiative cooling and surface heat and moisture fluxes are more significant than aerosol indirect effects in impacting large-scale organization of convection. Jones and Christopher (2010) used principal component analysis to examine a number of different atmospheric parameters and found that atmospheric conditions are more important to rain rate than aerosol-cloud interactions. Koren et al. (2012) determine that conclusions on aerosols depend on location and season, the spatiotemporal scale of the analysis, and the data source and tools used. Understanding the impacts of aerosols and whether changes to convection could alter regional circulations that in turn could lead to greater moisture convergence and precipitation (Rosenfeld et al. 2008) is critical to understanding the potential changes in the global hydrologic cycle.

In all of the studies that have examined the relationship between convection and increased aerosol concentrations, the vast majority use numerical models, which rely on various microphysical parameterizations including bin schemes, convective parameterizations, and other assumptions with varying degrees of uncertainty. These results are invaluable in developing a conceptual model of the effects of aerosols, but observational studies are critical to support the ideas that originate or are tested with

model runs. Obvious problems arise when designing such a study. First, there are no clouds (or cloud systems) in nature that differ only by aerosol amount (Khain 2009). Isolating the effects of aerosols from those of the thermodynamic environment is very difficult, particularly with satellite observations that only see convective features for one moment in time. Causality is impossible to determine from sensors that see a snapshot- did the convection form in the area of enhanced aerosol concentration? Or conversely, is the environment clean because the convection washed out the aerosol? The sensitivity of clouds to aerosol effects can appear weaker due to "buffering": changes in an isolated cloud due to aerosols may be cancelled out by opposing changes from other clouds when a large area is looked at on longer temporal scales (Stevens and Feingold 2009). There is great uncertainty in decoupling the influences of atmospheric dynamics and thermodynamics (Tao et al. 2012). Yet, establishing relationships between aerosols and convection via observations could further help develop parameterizations for cloud models (Lee et al. 2011).

Principal Objectives

Because of some of the difficulties associated with observations of aerosol and convection globally, no study has attempted to look at the relationship between the two on a global level over a long period of time. Thermodynamic and dynamic properties of the environment affect convection in a variety of ways, as described above. The effect of aerosols on the microphysical properties of clouds is one complicated piece of this puzzle. The first goal of this study is to determine whether the indirect effect of aerosols can be quantified (or even detected) using careful analyses of satellite data. The temporal

and spatial scale of the Tropical Rainfall Measuring Mission (TRMM) satellite and the A-Train constellation of satellites allow a climatology of over 14 years of convection in the tropics. *Using these sensors, can we detect the aerosol indirect effect, and if so can we determine how aerosols affect the evolution, vertical structure, and organization of convective clouds in the Tropics?*

CHAPTER 2

DATA AND METHODS

TRMM Satellite

The precipitation radar (PR) on TRMM is the first of its kind in space, and it allows the opportunity to see precipitation in three dimensions in the Tropics (Kummerow et al. 1998). It has a 250 km swath, and its range extends from 36°S to 36°N. The TRMM Microwave Imager (TMI) is a passive microwave radiometer with nine channels. The combination of the PR and the TMI allows precipitation to be observed from two perspectives- that of a radar, an active sensor for which reflectivity is related to particle size, and a microwave imager, a passive sensor that is sensitive to ice scattering at certain frequencies. Ice scattering is related more closely to total ice water content than to ice particle size. Fourteen years of TRMM data help compensate for infrequent sampling and allow the construction of robust climatological statistics. The primary source of TRMM data for this study is the University of Utah Precipitation Feature (PF) database (Liu et al. 2008). Radar Precipitation Features (RPFs) are identified as in Nesbitt et al. (2000) and are classified by contiguous 2A25 near-surface raining pixels (Iguchi et al. 2000). The 2A25 algorithm corrects for attenuation and estimates the rain profile (http://disc.sci.gsfc.nasa.gov/precipitation/documentation/TRMM_

README/ TRMM_2A25_readme.shtml/). For this study, RPFs with a minimum area of four pixels, or around 110 km^2, were used. Some of the properties defined for RPFs in this database include maximum height of the 20-, 30-, and 40- dBZ echoes, volumetric rainfall from 2A25, minimum polarization corrected temperature (PCT) for 37- and 85-GHz as seen by the TMI, area of the RPF, and the geo-center location of the RPF. Mean rain rate was calculated by dividing volumetric rainfall by area, and convective percentage was calculated using 2A25 and the 2A23 algorithm (Awaka et al. 1997). Lightning flash count was determined using the LIS sensor, which is a staring optical imager that identifies changes in radiances in the field of view (Nesbitt et al. 2000). The minimum detectable flash rate is one flash per minute (Toracinta et al. 2002). All TRMM data was obtained from the University of Utah TRMM Database.

CloudSat Database

TRMM is an ideal suite of sensors for looking at intense convection, but a minimum detectable signal of 18 dBZ does not allow for an accurate determination of cloud top. The CloudSat satellite can provide this. CloudSat is part of the A-Train constellation, which includes five satellites flying in formation so that they follow closely behind one another (Stephens et al. 2002). CloudSat carries the Cloud Profiling Radar (CPR), a 94-GHz, near-nadir pointing cloud radar, which measures the vertical structure of clouds, producing a two-dimensional cross section along the satellite track (Marchand et al. 2008). Cloud features have been identified using the 2B-GEOPROF product, which contains cloud mask and reflectivity at a resolution of 1.1 km along track by 1.3 km across track with a minimum detectable signal of -28 dBZ (Stephens et al. 2002, Mace et

al. 2007). All CloudSat data products were downloaded from the CloudSat Data Processing Center (http://cloudsat.cira.colostate.edu). A cloud feature (CF) is defined as 10 or more contiguous pixels with reflectivity greater than -28 dBZ and a cloud mask value of at least 20. Additionally, the bottom of the feature must occur at a height greater than the terrain height. The reflectivity and cloud mask criteria identify clouds, while the area restriction helps filter out noisy pixels.

Many of the database parameters are either taken from the 2B-GEOPROF files or are derived from these quantities. Orbit; year; month; day; hour; minute; second; starting and ending time of the feature; starting and ending latitude, and longitude of the feature; mean latitude and longitude; total number of pixels, and number of pixels along the satellite track are taken from each identified feature. The following parameters were defined using reflectivity: the horizontal distance along each feature (defined using the starting and ending latitude and longitude); cloud top and bottom; profile of maximum reflectivity; levels of the highest echo of -20, -15, -10, -5, 0, 5, 10, 15, and 20 dBZ; number of pixels of each of those reflectivities. Terrain height is included in addition to these parameters.

To add meteorological context to the RPFs and CFs defined using TRMM and CloudSat, data from the European Centre for Medium-Range Weather Forecasts (ECMWF) Interim Reanalysis (ERA-Interim) has been matched to each feature (Simmons et al. 2007). Three hourly data with a resolution of 1.5° were obtained from the ECMWF website. The mean latitude and longitude of each cloud feature was used to find the nearest ERA-Interim grid point, and the data from this point were linearly interpolated to match the time of the CloudSat overpass of the cloud feature. Geopotential

height; relative humidity; U, V, and W winds; and temperature are saved at 10 levels (1000 hPa, 975 hPa, 925 hPa, 850 hPa, 700 hPa, 500 hPa, 400 hPa, 300 hPa, 200 hPa, 100 hPa). Two meter U and V wind speeds, surface pressure, total column ozone, total column water vapor, total column liquid water, and skin temperature are saved for each feature as well.

MODIS Aerosol Products

Obtaining a reliable measurement for aerosol concentration on a global scale is a difficult task. The MODerate Resolution Imaging Spectroradiometer (MODIS) sensor, aboard the Aqua satellite, was launched in 2002 (King et al. 2003). It provides daily coverage on a global level, with overpass times around 0130 and 1330 local time. The aerosol optical depth (AOD) from the MODIS daily aerosol products has a resolution of 1° and can be used to gain some idea of the presence of high aerosol concentrations (Berg et al. 2008).

Aerosol Optical Depth (AOD) has been correlated to CCN concentration on a first order (Nakajima et al. 2001, Rosenfeld et al. 2008). The product of AOD and the Angstrom exponent better reflects aerosol characteristics because it takes into account particle size (Nakajima et al. 2001). Angstrom exponent is derived by representing the wavelength dependence of the aerosol extinction coefficient as $b_{ext} \approx \lambda^{-\alpha}$ where α is the Angstrom exponent (Seinfeld and Pandis 1998). Solving for this term gives

$$\alpha = -\frac{d\log b_{ext}}{d\log \lambda} \cong -\frac{\log(b_{ext1}/b_{ext2})}{\log(\lambda_1/\lambda_2)} \qquad (2)$$

where the subscripts 1 and 2 refer to different wavelengths across the spectral window for which the Angstrom exponent is being calculated.

The Angstrom exponent at a given wavelength reflects the scattering dependence on particle size. For a scene with small particles, the Angstrom exponent will be large. For a scene with larger particles, the Angstrom exponent will be small. In this study the optical aerosol index (AI) is calculated by multiplying the MODIS AOD at 550 nm with the Angstrom exponent calculated between 470 nm and 660 nm. This parameter will be called the optical aerosol index because it reflects aerosols in the visible part of the spectrum. Optically active aerosols are larger than 0.5 μm in radius (Rosenfeld et al. 2006), and aerosols of this size are activated at nearly any supersaturation (Dusek et al. 2006), so aerosols detected by MODIS AI at 550 nm should certainly be able to serve as CCN.

The MODIS Aerosol Algorithms

Separate algorithms are used over land (Tanre et al. 1997) and over ocean (Kaufman et al. 1997, Remer et al. 2005) to process MODIS radiances and obtain values of aerosol optical depth, Angstrom exponent, and other aerosol parameters. The assumptions that are involved in processing these data have critical implications for use of the data, and therefore must be understood. The following section is a brief description of the basic principles of the algorithm. A much more detailed description can be found in the MODIS MOD04 product Algorithm Theoretical Basis Document (Remer et. 2006).

MODIS measures reflectances at 36 channels ranging from 0.415 to 14.235 μm at resolutions from 250 m to 1 km, depending on wavelength (Salomonson et al. 1989). The

ocean aerosol algorithm uses the 0.555 μm, 0.659 μm, 0.865 μm, 1.240μm, 1.640 μm, and 2.130 μm bands, while the land aerosol algorithm uses .470 μm, 0.659 μm, and 1.240 μm (Remer et al. 2005). The basic idea behind the retrievals is that the measured radiance at the top of the atmosphere, ρ* can be written as

$$\rho^*(\theta,\theta_0,\phi) = \rho_a(\theta,\theta_0,\phi) + F_d(\theta_0)T(\theta)\rho(\theta,\theta_0,\phi)/(1 - s\rho') \qquad (3)$$

where θ is the view zenith angle, θ_0 is the solar zenith angle, ϕ is the azimuth of the scattered radiation from the solar beam, $\rho_a(\theta,\theta_0, \phi)$ is the path radiance, $F_d(\theta_0)$ is the normalized downward total flux for zero surface reflectance, T(θ) is the upward total transmission into the direction of the satellite's field of view, s is the atmospheric backscattering ratio, and ρ' is the surface reflectance averages on the view and illumination angles (Kaufman et al. 1997). The radiance at the top of the atmosphere (left hand side of the equation) is the quantity measured by MODIS. The second term on the right hand side of the equation can be approximated for a given field of view. The term for path radiance can be further expanded to

$$\rho_a(\theta,\theta_0,\phi) = \rho_m(\theta,\theta_0,\phi) + \omega_0\tau_a P_a(\theta,\theta_0,\phi)/(4\mu\mu_0) \qquad (3)$$

where $\rho_m(\theta,\theta_0,\phi)$ is the path radiance due to molecular scattering, ω_0 is the single scattering albedo for the aerosols, τ_a is the aerosol optical depth, P_a is the phase function, and μ and μ_0 are the cosines of the viewing and illumination angles, respectively. From equations 2 and 3, the aerosol optical depth can be related to the measured radiances from

MODIS, given a specific aerosol model, with which values of single scattering albedo and phase function can be determined (Kaufman et al. 1997). In the course of these calculations, aerosol size distribution, single scattering albedo, and refractive index are assumed, as well as that the aerosol is spherically shaped and homogenously distributed over the field of view (Kaufman et al. 1997, Levy et al. 2003).

Both the land and ocean algorithms follow the same basic path, beginning with radiances in the appropriate bands and assuming that the ambient aerosol over the field of view can be represented by one fine and one coarse lognormal aerosol distribution (Remer et al. 2006). The radiances used as input to the algorithm come from the MODIS L1B product and are corrected for atmospheric gaseous absorption prior to use in the aerosol algorithm (Appendix 1 of Remer et al. 2006). Various threshold tests and the MODIS MYD35/MOD35 cloud mask product (Ackerman et al. 1998) are used to determine which of these pixels are contaminated by cloud, sediment in water, or other odd reflective surfaces (Kaufman et al. 1997, Remer et al. 2006). The algorithm relies on comparisons of reflectivity over dark pixels: aerosol optical depth cannot be determined within clouds or in areas of high ocean glint, snow, and some regions of sediment in shallow water. For dark surfaces the aerosol radiative effect is stronger because backscattering of direct sunlight dominates over sunlight reflected from the surface (Kaufman et al. 1997).

MODIS Land Algorithm

If any individual pixel in the scene is identified as land, the land algorithm is used for the retrieval (Remer et al. 2006). For land scenes, the darkest 20% and brightest 50%

of pixels at 0.66 μm are discarded to eliminate cloud shadows and other odd surfaces. If there are at least 12 out of the original 400 pixels in a 10 by 10 km^2 box, the algorithm proceeds with the retrieval by using a continental aerosol model look up table (LUT) to determine the aerosol optical depth, τ, at 0.47 and 0.66 μm. The path radiance at these two wavelengths can be calculated from these optical depths, and the ratio of these radiances allows the algorithm to further refine the aerosol LUT by selecting a dust model, a non-dust model, or a mixed retrieval using both models. Different non-dust models are used based on seasonality and location (Remer et al. 2005). Each LUT contains optical properties of aerosols for seven possible values of optical depth, nine solar zenith angles, 16 sensor zenith angles, and 16 relative azimuth angles. The solution is the one that minimizes the error between the measured radiance at 0.66 μm and the value derived from the LUT at that wavelength. For a more detailed description of the algorithm, see the Algorithm Theoretical Basis Document (Remer et al. 2006).

MODIS Ocean Algorithm

The ocean algorithm is similar to the land algorithm and also uses a LUT to find the aerosol parameters. All 400 pixels in the 10 by 10 km^2 box must be classified as ocean, which helps reduce problems caused by shallow water near the coast (Tanré et al. 1997, Levy et al. 2003). The MODIS cloud mask product, spatial and temporal variability tests, and sediment tests, ocean glint tests, and other internal cloud tests are used to find dark pixels (Tanré et al. 1997, Remer et al. 2005). For the ocean retrieval, only the brightest and darkest 25% of pixels are discarded, as the ocean cloud mask is expected to be more accurate than the land cloud mask due to difficulties in estimating land surface

emissivity (Remer et al. 2006). At least 10 out of the original 400 pixels must remain in the 0.86 μm channel for the algorithm to proceed. The LUTs for the ocean algorithm have been primarily derived from data from photometers such as the global network of sun and sky photometers called the AErosol RObotic NETwork (AERONET) and from errors in previous versions of the MODIS algorithms (Remer et al. 2006). In the current algorithm version 5, there are four fine modes and five coarse modes of aerosol. The total radiance in the satellite's field of view can be written as $L_\lambda^t = \eta L_\lambda^f + (1-\eta)L_\lambda^c$, where L^t is the total radiance, L^f and L^c are the contributions from fine and coarse aerosols, respectively, and η is the fine weighting parameter, or reflectance weighting parameter over the ocean (Tanré et al. 1997, Remer et al. 2006). This fine weighting parameter represents the fraction of the aerosol optical depth that is contributed by fine mode aerosols (Remer et al. 2005). The reflectance at each wavelength is calculated for each combination of fine and coarse aerosol modes. The solution is the one that minimizes the fitting error between the measured reflectance and that calculated from the LUT for a given fine and coarse mode with a given reflectance weighting parameter (Remer et al. 2006). The mean of the top three best-fit solutions is also provided and is the product used in this study.

Before the results of the aerosol algorithm are output additional consistency checks make sure that the values of aerosol optical depth are within appropriate ranges, generally from -0.1 to 5.0 at 0.55 μm. The biggest uncertainties in the retrievals come from surface reflectances and the aerosol models, which in some cases are derived from point measurements and may not reflect the characteristics of aerosols in other locations around the globe (Kaufman et al. 1997). If 1% of a pixel is covered by snow, it could

cause an error in AOD of 0.1 (Kaufman et al. 1997). The assumption that all aerosols are spherical could also have an effect on scattering properties, causing MODIS AOD values to be too large in the 0.47 μm and 0.55 μm wavelengths and too small at 0.87 μm (Levy et al. 2003). In general the values of aerosol optical depth produced by MODIS and AERONET have similar annual cycles and magnitudes of optical thickness. Koren et al. (2010) found that on a day-by-day basis the MODIS AOD product is more accurate than the Goddard Chemistry Aerosol Radiation and Transport (GOCART) model and that it is the preferred source of AOD to derive quantitative relationships between cloud parameters and aerosols.

Limitations to MODIS Aerosol Data

AOD and AI are proxies for CCN, and the reliability of assuming that the two are related depends on the uniformity of the aerosol size, composition and vertical distribution (Koren et al. 2010, Tao et al. 2012). MODIS provides no information about aerosol composition, and yet different aerosol types are expected to produce different aerosol effects (van den Heever et al. 2006). Undetected clouds, aerosol humidification, and so called 3D cloud effects can yield a larger AOD when measured from space (Koren et al. 2010). Deliquescence of aerosol in regions of high relative humidity makes it difficult to determine how much of the scattering contribution to AOD comes from aerosol and how much comes from water (Gasso et al. 2000). Satellite derived AOD is also frequently overestimated in coastal regions due to ocean contributions (Li et al. 2009). Brennan et al. (2005) found that cloud contamination begins with AOD values of 0.6, so RPFs/CFs with AOD larger than 0.6 were excluded from this study. This value is

a standard cut off for other studies (Lin et al. 2006, Niu and Liu 2011). Koren et al. (2010) showed a positive correlation between MODIS AOD and cloud fraction or cloud top height, regardless of whether AOD measurements near clouds were filtered out or not. These difficulties in estimating AOD add to the uncertainty of this study.

One problem with the MODIS technique is that it cannot measure AOD in or near cloud, so we are forced to make the assumption that aerosol properties on a larger scale are similar enough to aerosol properties near the cloud to compute useful relationships between aerosols and cloud properties (Jones and Christopher 2010). Another assumption involves the timing of satellite overpasses. The values of AOD/AI come from Aqua MODIS, which has an overpass time of 1330 (AOD is only calculated for daytime overpasses). TRMM does not have a sun synchronous orbit, so RPFs are observed at any hour, leading to a time gap between the TRMM observation of an RPF and the MODIS overpass. Again, using a large area to average values of AOD should help find a reasonable value, but if a large mesoscale convective system (MCS) passed through between the time of the MODIS overpass and the TRMM overpass, the value of AOD/AI could be high when the RPF developed in a clean environment.

Because the values of mean AOD are averaged over a region and exclude values above 0.6, the effects of cloud contamination are minimized. The vertical distribution of aerosols is problematic. As previously mentioned, aerosols in the boundary layer are more important in changing microphysical properties of the cloud than aerosols in the mid-troposphere (Chen et al. 2011). It is possible that a high value of AOD could result from elevated aerosols, and that the convective cloud could be forming in a relatively clean boundary layer. Currently there are no satellite products that offer determinations of

aerosol height. Global transport models could be one solution to this problem. In these models aerosol height and concentrations can be determined regardless of the presence of clouds, however these models also require assumptions.

MODIS Data

For this study, MODIS AOD parameters are matched to each RPF or CF. AOD values are located in the MOD04_L2 product. The corrected aerosol optical depth for land, mean effective optical depth for ocean, Angstrom exponents for land and ocean, and number of pixels used in the calculation of each 1° bin were obtained from the Level 1 and Atmosphere Archive and Distribution System (LAADS). The "mean AOD" is the mean value of MODIS AOD (land or ocean, whichever is appropriate) at 0.55 μm averaged over a 4° box centered on the RPF/CF. The mean optical AI value was calculated for each 1° bin by multiplying the AOD by the Angstrom exponent. A "mean AI" value was calculated for each RPF/CF in the same manner as mean AOD. Ideally the mean value of AOD or AI within this region is representative of the large-scale environment, particularly if we are examining regions of biomass burning where aerosol concentration can be affected on a large scale.

It is important to note that within the 4° box used to calculate mean AOD/AI, some data values will be missing due to clouds. Each 1° bin in the MODIS data is calculated using either 110 (land) or 202 (ocean) pixels of level 2 data, with a pixel resolution of 5-10 km, depending on which wavelengths are used. This is shown in Figure 1. In order to consider an RPF to have a good match with MODIS, at least 8 out of 16 possible data points must exist within the 4° box surrounding the RPF. Additionally,

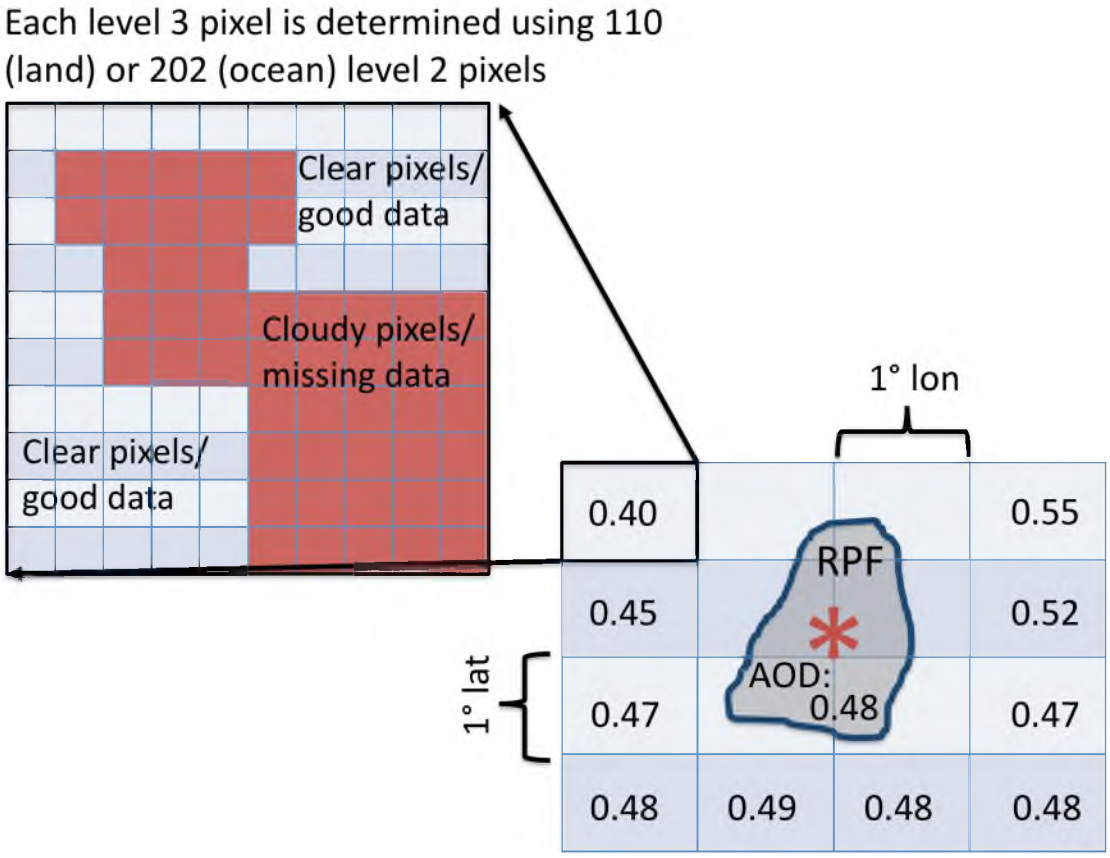

Figure 1: Selection of a mean AOD or AI value for each RPF or CF, which is represented by the red asterisk. The mean value of AOD comes from the surrounding 4° of latitude and longitude, and each of these 1° pixels are made up of a number of level-2 pixels, shown in the upper box. Some pixels will have missing data due to cloud.

for AI, at least 5 data points must be used in the creation of each 1° bin. This ensures that one single data value is not selected to represent an entire 1° area.

The seasonal distribution of MODIS AOD can be seen in Figure 2. This figure shows good agreement with the locations of high and low values AOD seen in Figure 8 of Remer et al. (2008) and also with the seasonal distributions seen in Yu et al. (2003). The northern hemisphere generally has higher values of AOD. Notable maxima caused

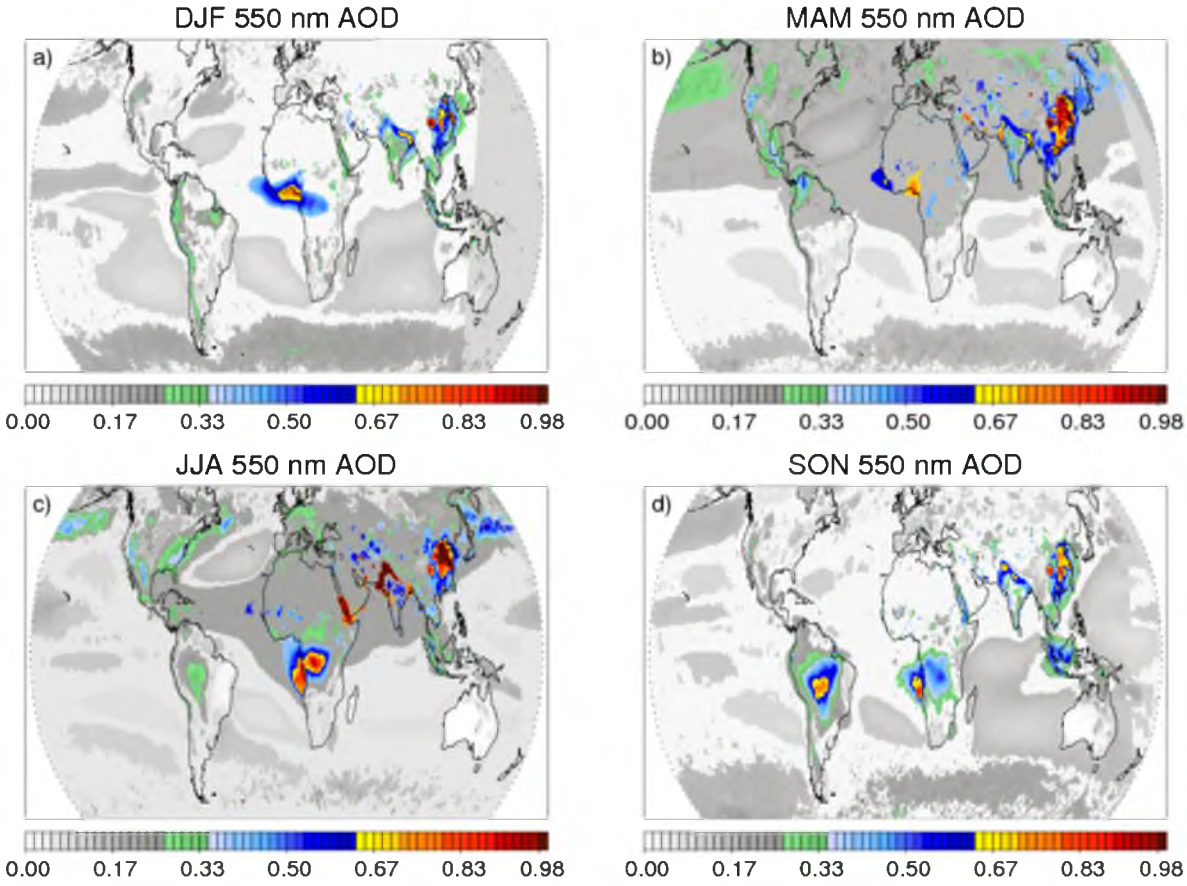

Figure 2: Global distribution of 10-year (2002-2011) mean MODIS AOD at 0.55 μm for a) December-February, b) March-May, c) June-August, and d) September-November. biomass burning to the southeast (Yu et al. 2003). Elevated AOD values occur over the equatorial Atlantic Ocean due to dust from the Sahara, but ocean regions tend to have lower values of AOD than land regions.

by biomass burning can be seen in the central Amazon and southern Africa during the boreal fall. East Asia also has very high aerosol loading from dust outbreaks and biomass burning to the southeast (Yu et al. 2003). Elevated AOD values occur over the equatorial Atlantic Ocean due to dust from the Sahara, but ocean regions tend to have lower values of AOD than land regions.

The seasonal distribution of MODIS AI is shown in Figure 3. AI has similar maxima, particularly during the boreal fall season in the Amazon and Africa. Because AI takes into account the sizes of the aerosols, some areas stand out more in Figure 3 than in Figure 2. The eastern United States during spring and summer is a good example of this. The size of aerosols can vary widely (hence using small and coarse modes for the MODIS algorithms), but a large number of smaller particles will be "dirtier" than a small number of large particles. A dirtier atmosphere, in many cases, will have more possible CCN, and therefore is more likely to produce aerosol effects. AI is a better indicator of this dirty air than AOD alone.

RPFs are termed, "clean" or "dirty" based on the values of MODIS AI collocated with the RPF. AI quartiles are used to define these categories. The bottom quartile is "clean", while the top quartile is "dirty". Using these values will help ensure that the values of AI are representative of the area in which the feature occurs- all of the values of AI surrounding the target cloud must be either very high or very low for the mean AI of the RPF to be in the clean or dirty categories. If a gradient of AI existed within the 4° box, it would average out to a moderate value.

The use of this criterion to select dirty and clean environments is helpful when looking for differences in convective features forming in clean and dirty regions. Because

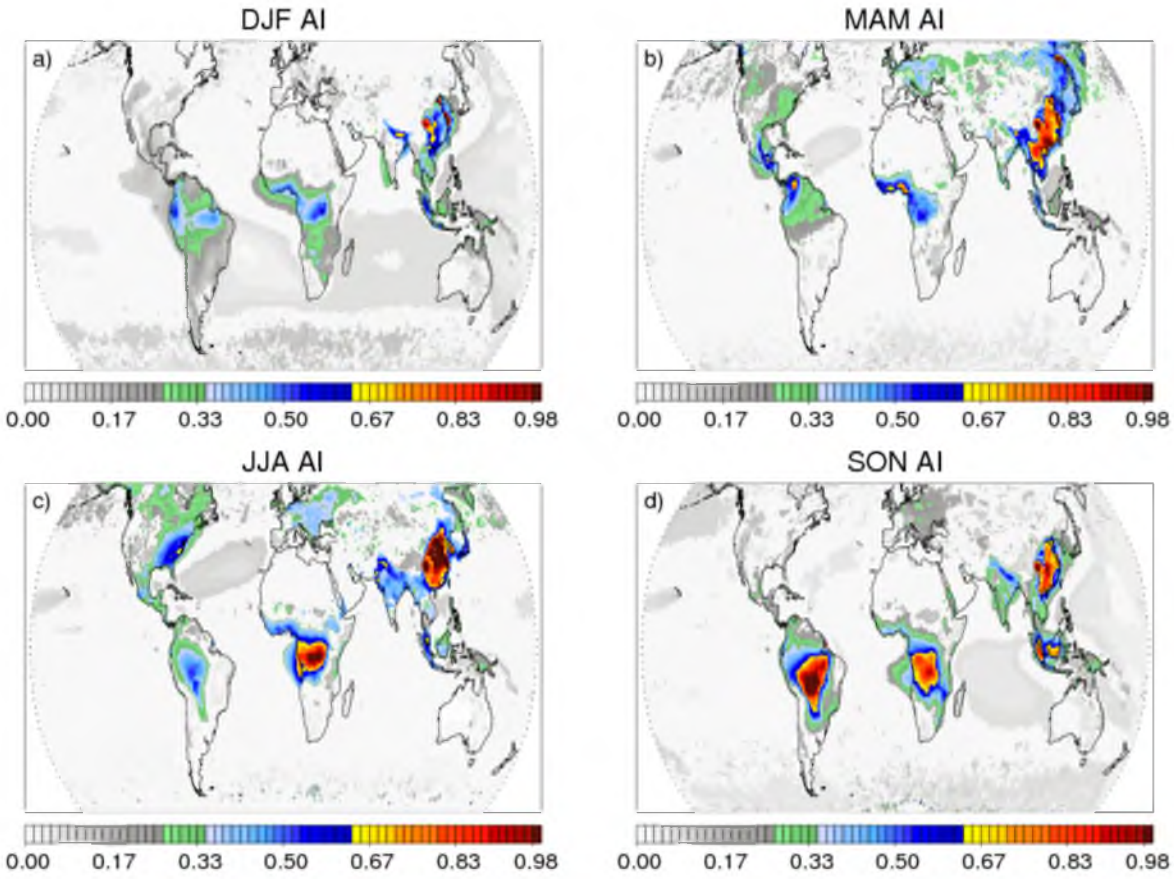

Figure 3: Global, seasonal distribution of 10-year (2002-2011) mean MODIS AI for a) December-February, b) March-May, c) June-August, and d) September-November.

each region has different sources of aerosols, values of AI vary from region to region. Ocean areas typically have much lower values than land. Using the upper and lower quartiles to separate clean and dirty environments allows the comparison of features in regions with varying ranges of AI values. The very cleanest and dirtiest in each region will be compared. This analysis is further described in the following chapter.

CHAPTER 3

AEROSOLS AND DEEP CONVECTION

While it is known that environment plays an important role in determining the magnitude of aerosol effects, it is useful to begin an analysis of the aerosol indirect effect by looking globally at features from the TRMM satellite that are classified as clean or dirty. While differences between clean and dirty features are not necessarily caused by aerosol alone, it is important to determine whether differences exist.

Analysis with TRMM

In some figures in this study, the upper and lower quartile values of AI for the entire population of RPFs will be used to define clean and dirty RPFs. The lower quartile for all global RPFs is $0.0 < AI < 0.038$, while the upper quartile is $0.128 < AI < 0.8$. The very wide spread in the upper quartile occurs because most values of AI over the ocean are very clean. In some figures the population of RPFs has been divided into land and ocean. This allows a better separation of clean and dirty cases using the upper and lower quartiles because ocean air tends to be cleaner than air over land. Ocean RPFs have a median AI of 0.056, while land RPFs have a median AI of 0.273. The upper and lower quartiles for land and ocean are labeled in Figure 4.

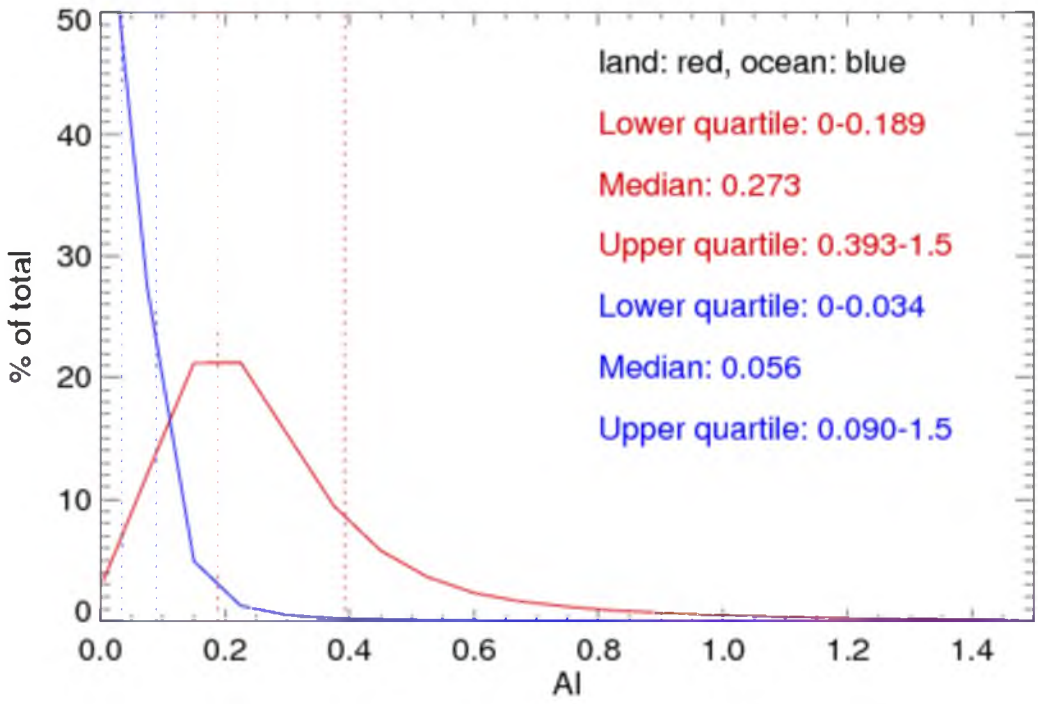

Figure 4: Histogram of aerosol index (AI) for the global population of RPFs. Land RPFs are shown with red, and ocean RPFs are blue.

Using definitions of clean and dirty based on the quartiles for the entire globe, Figures 5 and 6 show the seasonal distribution of clean and dirty RPFs. As expected, the vast majority of dirty RPFs occur over land, while clean RPFs are more populous over the oceans. Some areas that are known to be aerosol-laden (the Sahara desert, for example) do not show up in this figure because AI has been paired with RPFs-precipitation features are necessary.

The Southern Hemisphere has fewer dirty RPFs, matching the results of Yu et al. (2003). The northern half of South America has a large population of dirty features year round. Africa has a distinct peak in fall during biomass burning season. The US has many more dirty RPFs during the summer, as does western China. Oceans on the east side of continents in the northern hemisphere have larger populations of dirty RPFs as aerosol is transported off the coast.

Clean RPFs occur mostly over the ocean. The southeastern United States has some clean RPFs during the winter season. The clean RPFs in Figure 5 demonstrate the importance of defining clean and dirty populations for individual regions. Because land AI values are so much higher than ocean AIs, if the total upper and lower quartiles were used for comparing regions, many land regions would have virtually no clean RPFs and ocean regions would have no dirty RPFs. For this reason clean and dirty features will be defined using the upper and lower quartiles of the regional population when examining specific locations. One issue with this definition is that values of AI over the ocean are so much cleaner that the upper quartile may not be representative of what are typically considered dirty or polluted environments. This will be discussed on a regional basis.

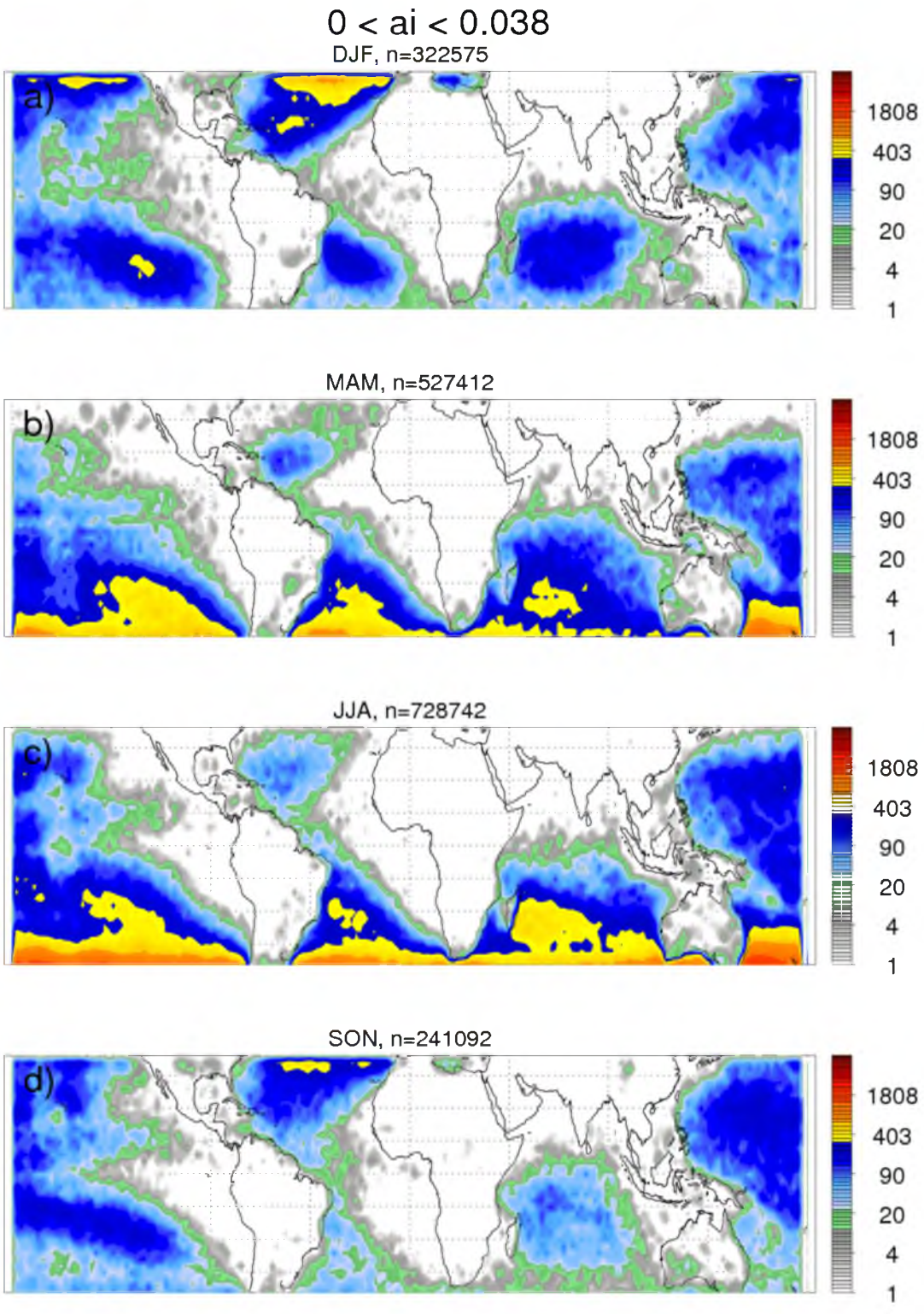

Figure 5: Population of clean (0.0<AI<0.038) RPFs for a) December-February, b) March-May, c) June-August, and d) September-November.

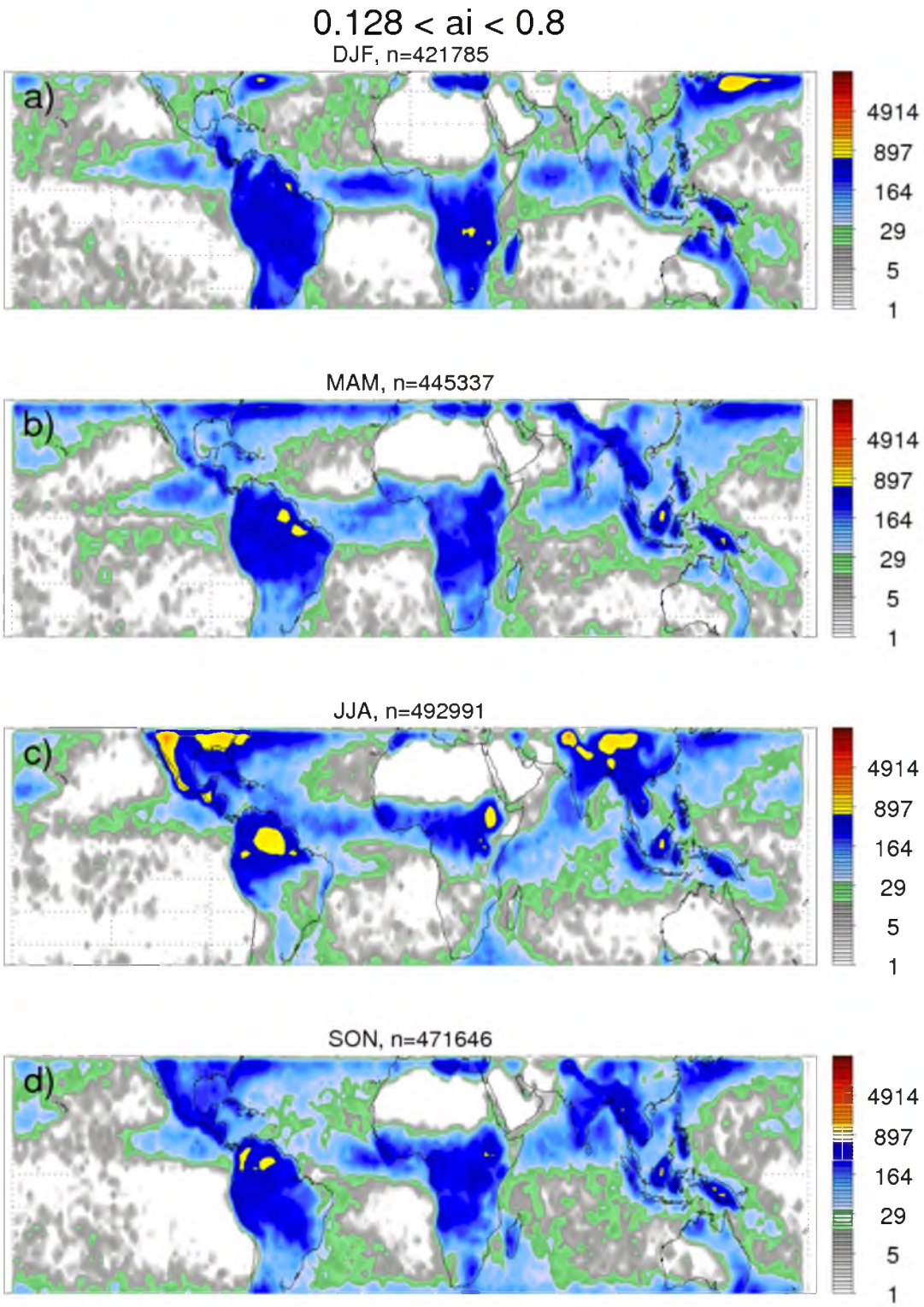

Figure 6: Population of dirty (0.128<AI<0.8) RPFs for a) December-February, b) March-May, c) June-August, and d) September-November.

Breaking down these global RPFs into clean and dirty categories allows an initial comparison between clean and dirty RPFs. Figure 7 shows histograms of volumetric rainfall (the product of area and rain rate) from the TRMM PR and flashcount from LIS, as well as cumulative distribution functions (CDFs) of the maximum height of the 40 dBZ echo and 20 dBZ echo. Differences in intensity over land and ocean are immediately apparent. Differences in volumetric rainfall are very small and difficult to distinguish. Above 600 $mmkm^{-2}hr^{-1}$ dirty features over land have slightly larger values of volumetric rainfall, however the differences in these distributions are not found to be statistically significant using a t-means test. Differences in flashcount are visible over only a small range as well, with a larger population of dirty features having between 1-5 flashes when compared to clean features. Again the differences in flashcount between clean and dirty features are not statistically significant and do not demonstrate aerosol indirect effects on a global scale. Yuan et al. (2011) found an increase in lightning activity with increased aerosol loading. Williams et al. (1999) found that larger CCN concentrations lead to higher maximum flash rates. Additionally, the CDFs of the maximum height of 40 and 20 dBZ show very clearly that dirty RPFs have higher echo tops over both land and ocean. This is also consistent with previous studies that have found higher cloud tops and enhanced reflectivities in dirty clouds (Andreae et al. 2004, Koren et al. 2005, Koren et al. 2010, Koren et al. 2012, Storer et al. 2013, Storer and van den Heever 2013). Because these populations are separated only by AI, these differences could be a result of other environmental factors. Additionally, "dirty" values of AI over the ocean are much lower than "dirty" values of AI over land. While using quartiles to separate clean and dirty RPFs allows comparison of RPFs occurring in the cleanest and dirtiest of environments

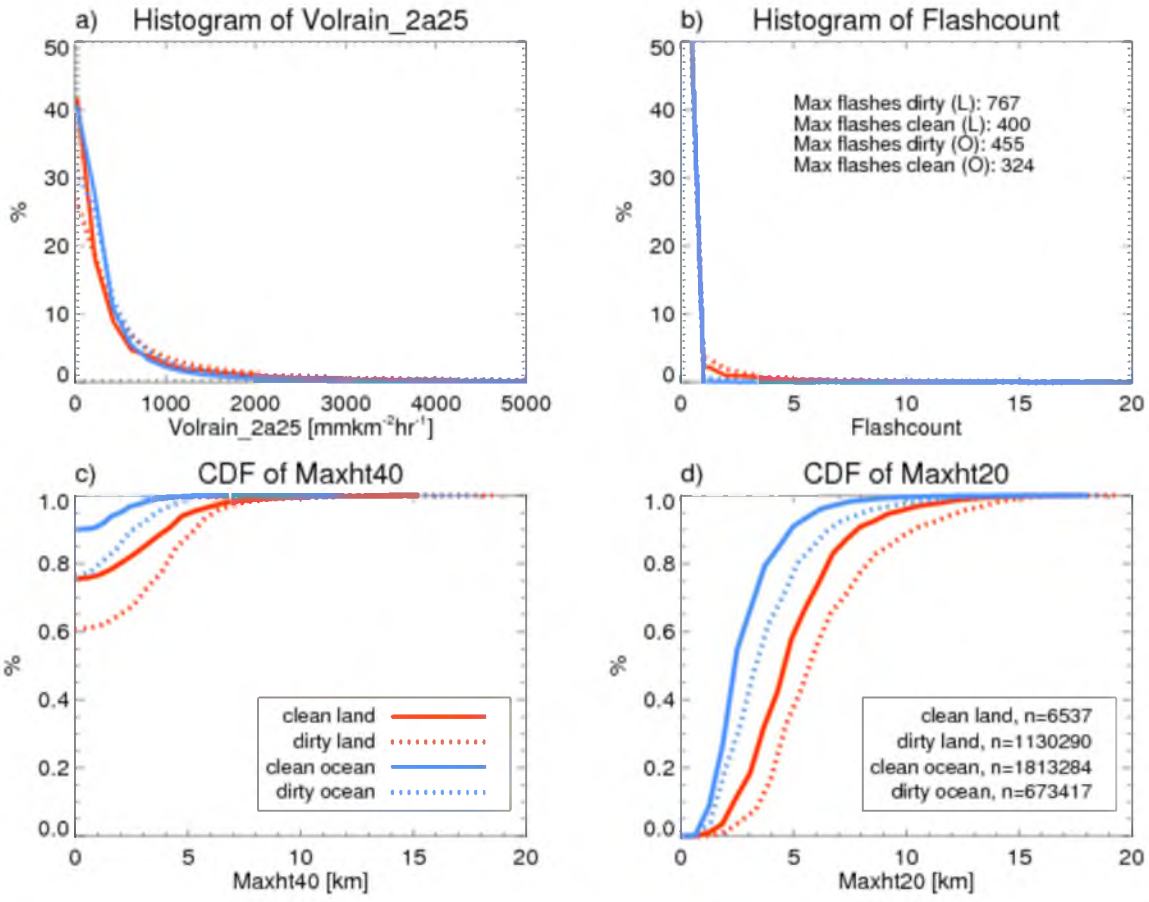

Figure 7: Properties and differences between dirty/clean RPFs over both land and ocean are visible in a) the histogram of volumetric rainfall from the PR (2A25 algorithm), b) the histogram of flashcount from LIS, c) the cumulative distribution frequency (CDF) diagram of maximum height of the 40 dBZ echo, and d) the CDF of the maximum height of the 20 dBZ echo. Red indicates land RPFs, blue indicates ocean RPFs, solid lines indicate clean RPFs, and dotted lines indicate dirty RPFs.

within each region, low values of AI for "dirty" RPFs over the ocean indicate a smaller number of potential CCN. This issue will be discussed in greater detail in Chapter 6.

Because CAPE, relative humidity, and shear are three of the big factors influencing convection, selecting a few of these variables and comparing them to AI on a global scale may prove useful in looking for aerosol effects. Figure 8 shows histograms of RPF area from the PR binned by AI and mid-level relative humidity from the ERA-interim. No clear trend can be seen with increasing AI, although area increases as

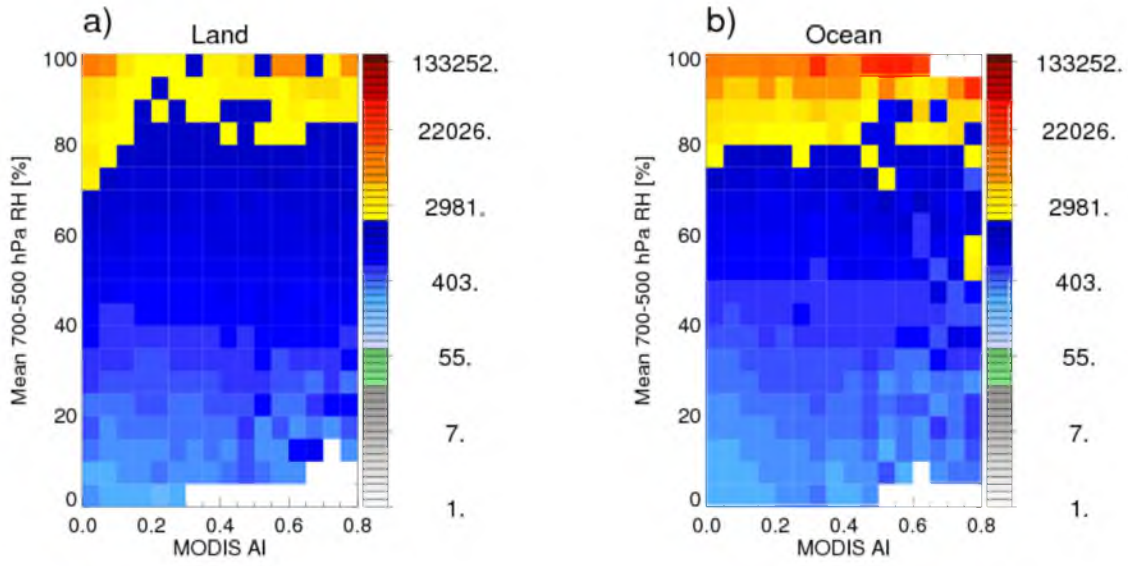

Figure 8: Two-dimensional histograms of the mean area [km^2] of RPFs for a) land and b) ocean by MODIS aerosol index and the mean relative humidity from the ERA-Interim between 700-500 hPa.

midlevel relative humidity increases. This same pattern occurs if maximum area is plotted (not shown). Multiple regression shows that mean mid-level relative humidity is a better predictor of area than AI.

Figure 9 shows a similar histogram of mean precipitation rate (an instantaneous rate calculated by dividing the volumetric rainfall from the 2A25 algorithm by the area of rain detected by the PR) with increasing AI and CAPE. Note that the RPFs in this global population are in all phases of life cycle. In this figure precipitation rates over land and to a lesser extent, ocean, do increase with higher values of AI, although there are no

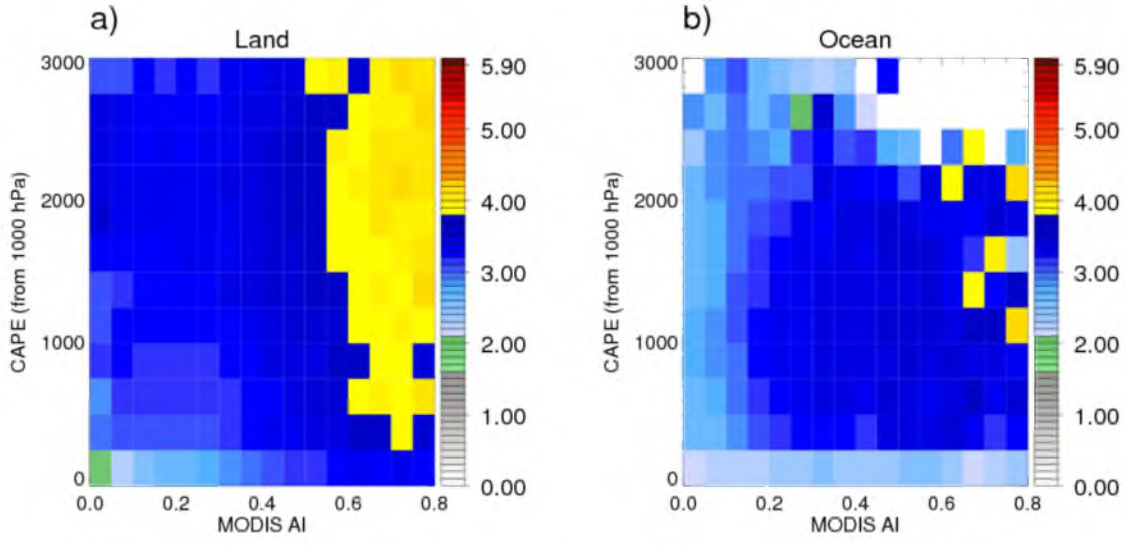

Figure 9: Two-dimensional histogram of mean precipitation rate [mm/hr] for a) land and b) ocean from the PR with increasing MODIS aerosol index and CAPE. Colored boxes indicate precipitation rate.

differences in precipitation rates with AI for low and high values of CAPE, as seen in the model of Lee et al (2008) and Storer et al. (2010). Multiple linear regression showed that AI is a better predictor of rain rate than CAPE. Adding CAPE in a stepwise regression did not explain additional variance for either land or ocean. No pattern is seen for maximum precipitation rate (not shown).

Environment plays a very important role in determining the strength of convection, so in order to make a reasonable comparison between clean and dirty RPFs, location must be taken into account. Figures 10 and 11 show the percentage of RPFs within each bin that have a 30 dBZ echo top above 6 km. Clouds with a 30 dBZ echo top above 6 km have a greater probability of having lightning (Liu et al. 2012). For this figure, land and ocean have separate upper and lower quartiles, as described in Chapter 2. This allows the separation of the very cleanest and the very dirtiest RPFs over both land and ocean. Note that bins with few samples are excluded. In the southern part of South America, as well as parts of Africa during SON and a small area of the southeastern United States during JJA, RPFs in the upper quartile with respect to AI have a greater percentage of the population of RPFs with 30 dBZ echo tops above 6 km. Changes are visible over the western Pacific in JJA and central Pacific during DJF and MAM. From these figures, paired with Figure 7, it seems that dirty RPFs do have higher values of reflectivity at higher altitudes than clean features. This result agrees with the results of Storer et al. (2013) and Storer and van den Heever (2013). Regional results will be discussed further in the next section.

In order to further investigate the differences in echo top height, profiles of the bottom 10%, median, and top 10% values of reflectivity were created for clean and dirty

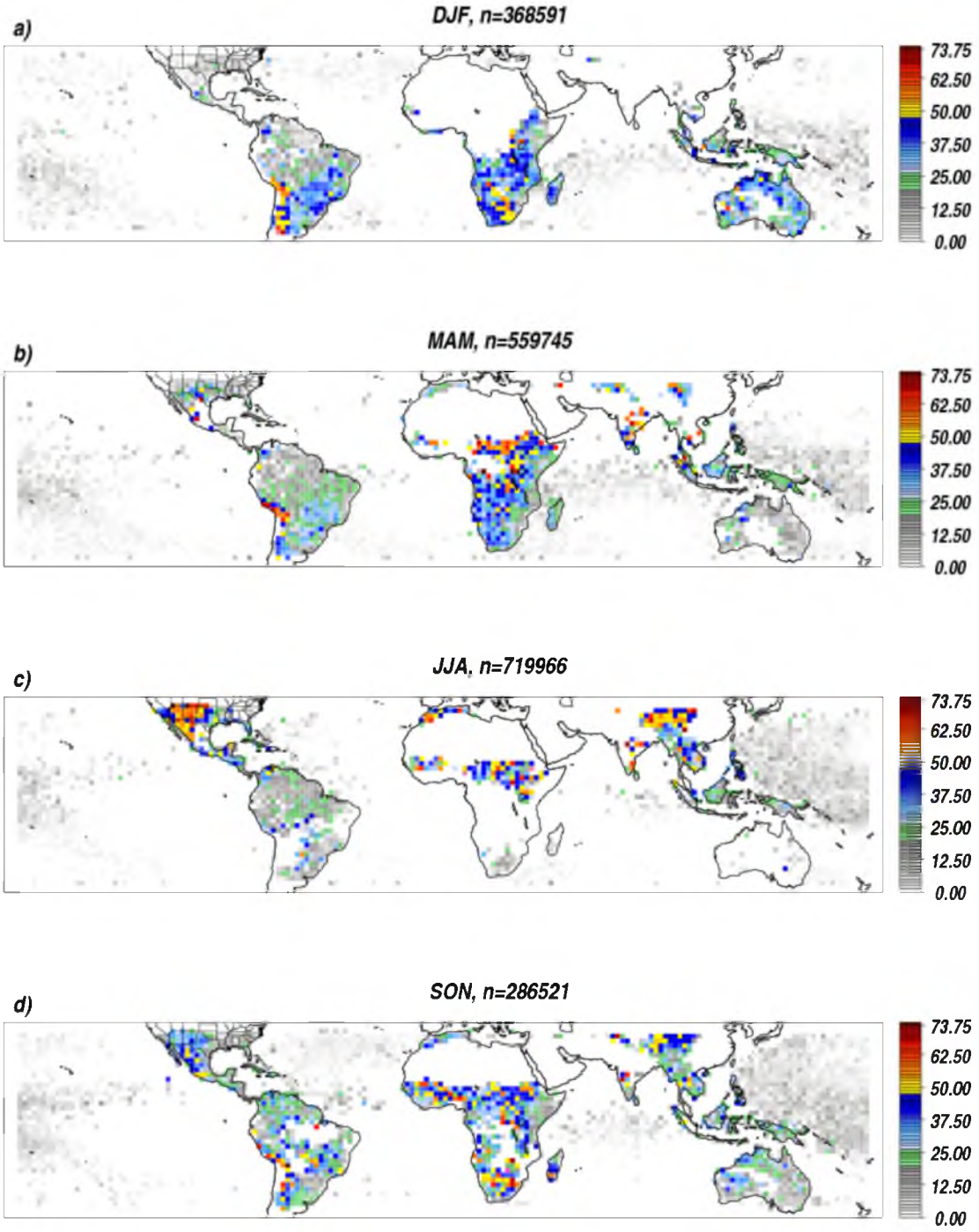

Figure 10: The seasonal distribution of clean RPFs with 30 dBZ echo top greater than 6 km. Percentage of the population within each 2° bin is indicated in color. Bins must have at least 10 samples to be included.

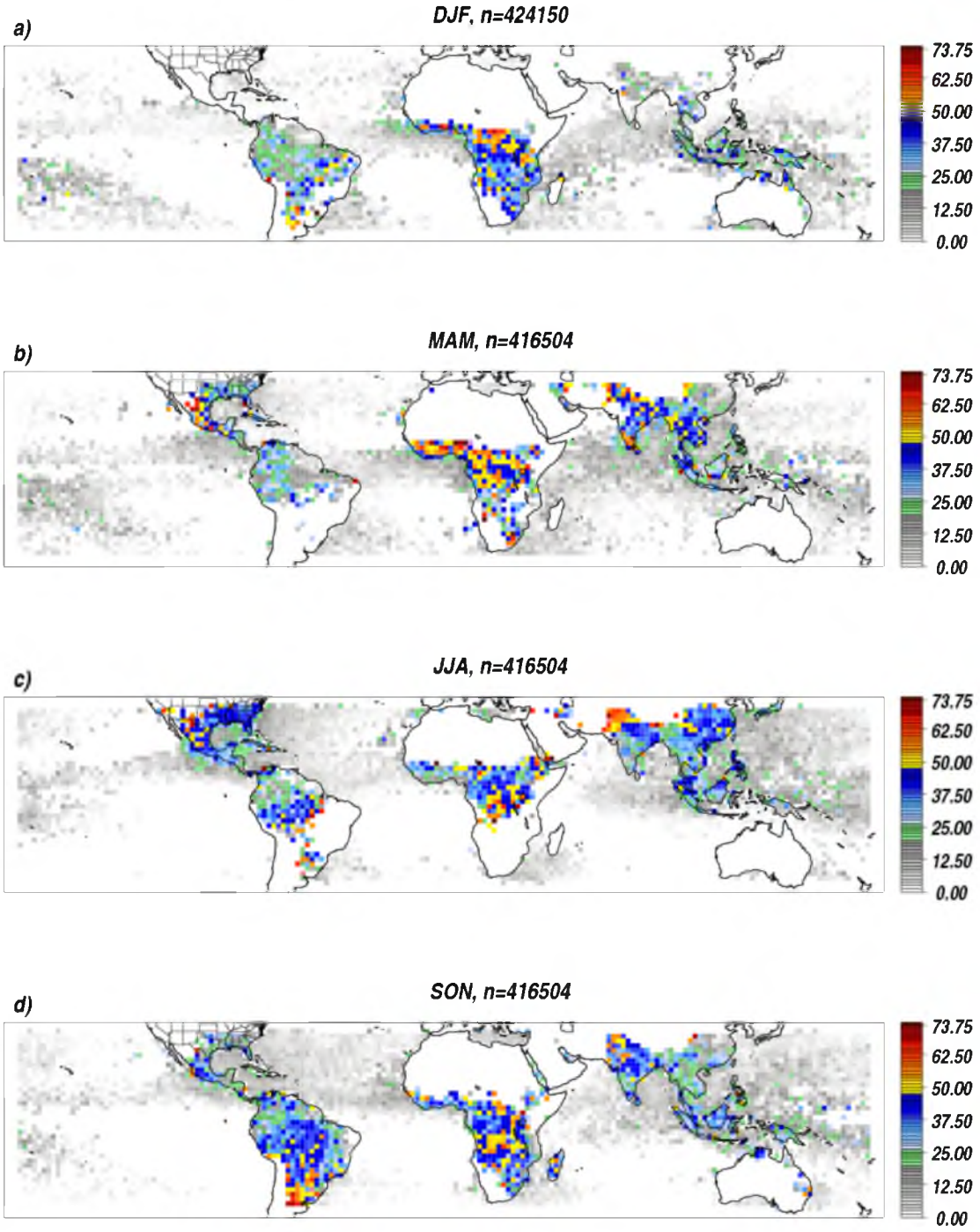

Figure 11: The seasonal distribution of dirty RPFs with 30 dBZ echo top greater than 6 km. Percentage of the population within each 2° bin is indicated in color. Bins must have at least 10 samples to be included.

RPFs globally, using the global upper and lower quartiles of AI. Figure 12 shows these profiles. A very clear difference is observed, with dirty features having much taller reflectivity profiles for median and top 10%. These distributions are statistically significantly at the 99% level using a Komolgorov-Smirnov test at each level.

Differences between these two profiles should be expected. Specifically, because dirty RPFs occur primarily over land, they should be taller with higher maximum reflectivities. Clean RPFs should have characteristics of oceanic features. In order to truly determine differences between clean and dirty features, individual regions and seasons must be compared.

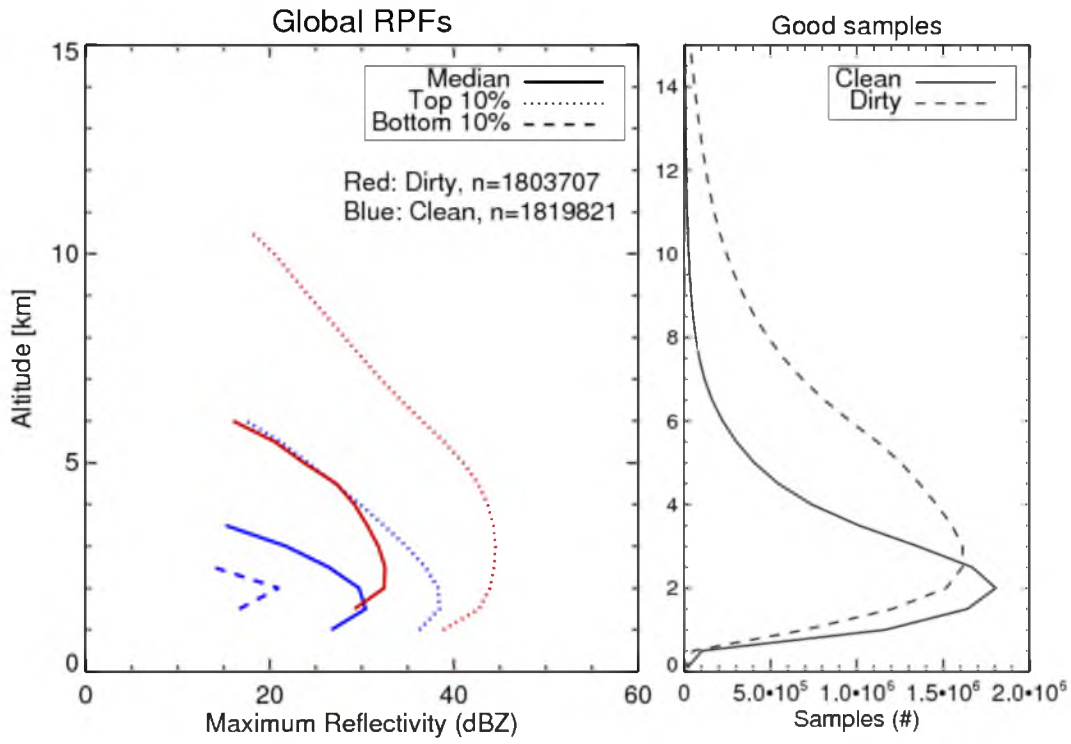

Figure 12: Profiles of bottom 10%, median, and top 10% of reflectivity for clean and dirty features. Dirty features are red, and clean features are blue. Population of each sample is indicated at right.

Regional Analysis

Different parts of the world have different thermodynamic environments as well as different typical aerosol compositions. In order to isolate the effects of aerosols, these regional disparities must be taken into account. To accomplish this, several regions have been selected for specific seasons during which they have a certain characteristic aerosol type. These regions are labeled in Figure 13. The Amazon and Africa regions will be observed during the Southern Hemisphere fall, during periods of biomass burning. Biomass burning in the Amazon releases fine mode sulfur particles, black carbon, mercury, iron and other particulate matter, and during biomass burning season, values of aerosol optical thickness increase drastically (Artaxo et al. 2009). A significant fraction (40-60%) of these aerosol particles can act as CCN (Gunthe et al. 2009). In Africa, anthropogenic biomass burning particulate matter and natural mineral dust can become mixed to varying degrees. Studies have shown that during the fire season, an elevated layer of smoke is present above a dust-rich surface layer (Liousse et al. 2010). The central Atlantic will be selected for the summer period, during which time mineral dust and anthropogenic pollution from Europe are advected over the ocean from the Sahara (Garrett et al. 2003). Northern Mexico, during the summer months of the North American Monsoon, will also be examined.

Within these regions, "clean" and "dirty" RPFs will again be defined based on the upper and lower quartiles of MODIS AI. While these values are different for each region, it allows for a comparison between features in the cleanest and dirtiest environments within each region, which is the goal of this study, particularly since regions are known

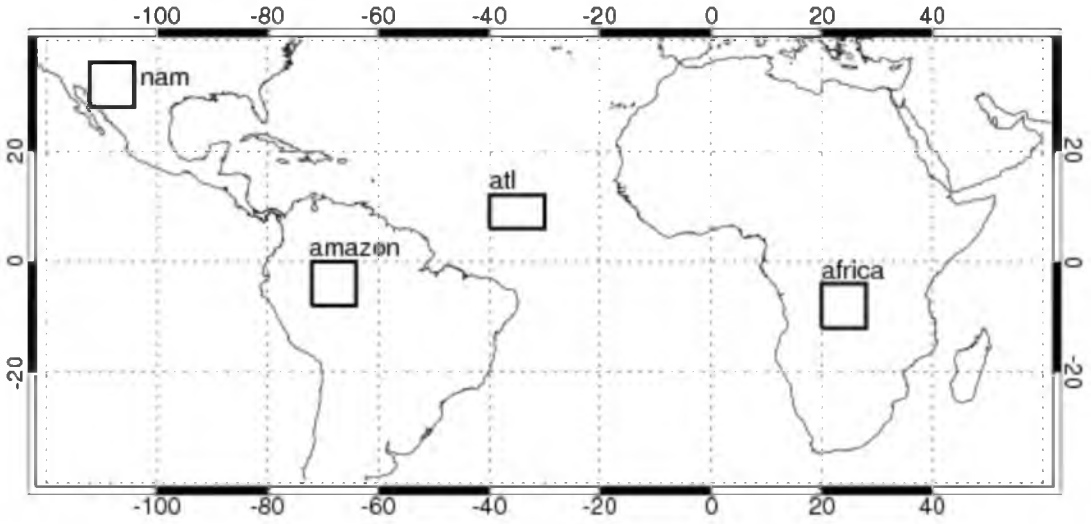

Figure 13: The four regions in the study: North American Monsoon, Amazon, Atlantic, and Africa.

to have differences in aerosols amount and type. The histograms of aerosol index for these regions are shown in Figure 14.

Each region has a very different distribution of aerosol index. The lower limit for the upper quartile in the Atlantic region would be in the lower quartile in the other three land regions. The dirty RPFs in the Atlantic have larger values of AI than clean RPFs, so they may have more available CCN than RPFs in the clean oceanic environment, but the differences between clean and dirty environments over the ocean are far less than the differences between clean and dirty environments over land.

Africa has the greatest overall variability in AI and the greatest number of high AI values, which range up to 1.5. The Amazon and Desert Southwest regions have peaks at lower values than Africa but experience higher values as well. The Desert Southwest is the cleanest of the three land regions. Each of these regions was selected from figures such as Figures 5 and 6, ensuring that there are both clean and dirty features based on the global population.

How do properties of RPFs vary with increasing AI in these regions? Table 1 shows the properties of flashcount from all four regions for clean and dirty RPFs. Because the Atlantic region is oceanic, flashes are not expected, although slightly more dirty features have flashes (based on the mean number of flashes). In the Amazon and Africa regions, the dirty population has a larger number of mean flashes per RPF, a greater number of maximum flashes (matching the results of Williams et al. 1999), and higher percentages of features with at least 1 flash and more than 5 flashes. The NAM region is very different, with the population of clean RPFs having more flashes in each category.

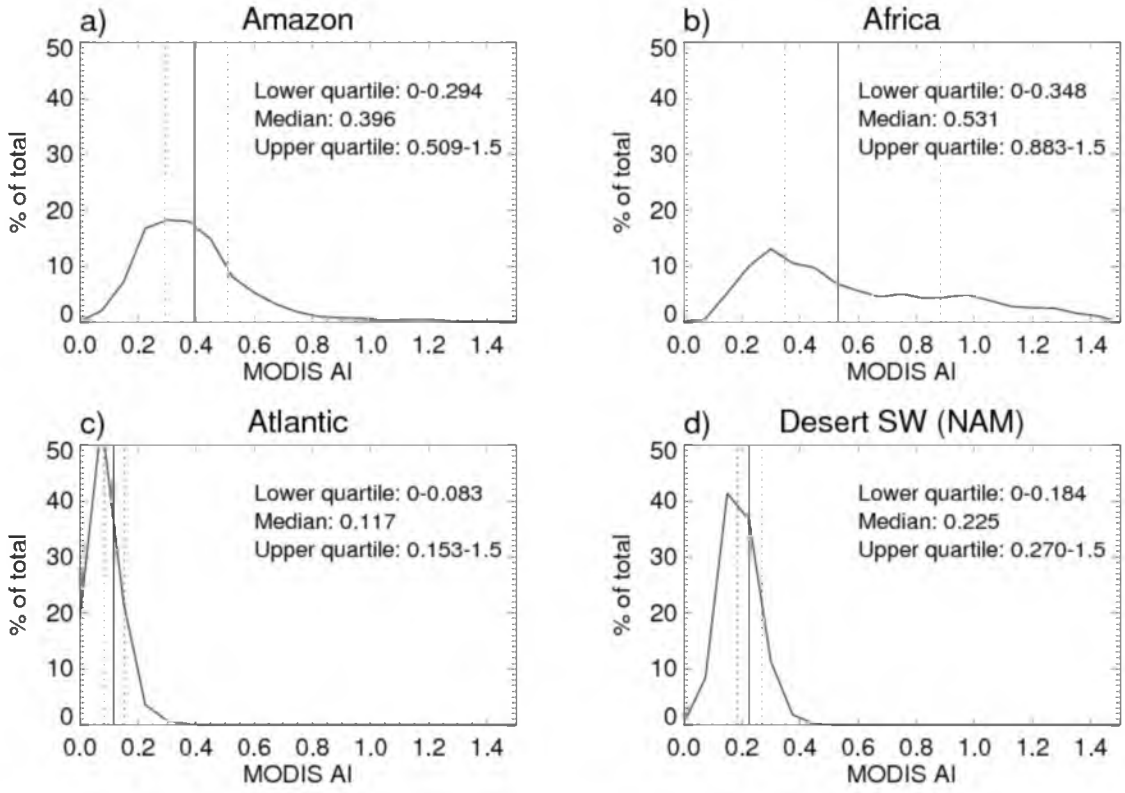

Figure 14: Histograms of MODIS aerosol index (AI) for the regions used in this study. The panels show a) the Amazon, b) Africa, c) the Atlantic, and d) the North American Monsoon region in southwestern North America.

Table 1: Properties of Flashcount for each region

	Mean Flashes	Min Flashes	Max Flashes	RPFs with 1+ flash (%)	RPFs with 5+ flashes (%)
Amazon (Clean)	0.557	0	47	9.13	3.24
Amazon (Dirty)	1.78	0	184	17.5	6.96
Africa (Clean)	1.85	0	94	18.1	8.52
Africa (Dirty)	3.27	0	168	26.3	13.1
Atlantic (Clean)	0.00378	0	4	0.151	0
Atlantic (Dirty)	0.00529	0	2	0.454	0
NAM (Clean)	2.07	0	230	24.0	8.79
NAM (Dirty)	1.61	0	168	21.0	7.74

Figures 16-19 show the percentage of features with 30 dBZ echo tops above 6 km for both clean (a) and dirty (b) features. This parameter showed a relatively clear signal in global plots (Figures 10-11). Some areas tend to have a larger percentage of RPFs with 30 dBZ reaching 6 km in dirty environments. In the Amazon and Africa regions (Figures 16-17), dirty features do have a larger percentage of 30 dBZ echo tops above 6 km. In the Atlantic region, no pattern can be discerned, and in the NAM, a higher percentage of clean features have 30 dBZ extending above 6 km.

The Amazon and Africa regions are, as mentioned previously, regions of large-scale biomass burning during the months of September-November. These types of fires produce large amounts of smoke particles, which can serve as CCN that invigorate the cloud (Rosenfeld 1999). Williams et al. (1999) found greater lightning flash rates in clouds in dirty environments. The Atlantic region is an area that is affected by the Saharan Air Layer (SAL) during the summer months. The SAL brings with it dust from Africa as well as anthropogenic pollution from Europe (Garrett et al. 2003). The dust can act as a CCN, but it can also decrease the in-cloud supersaturation and reduce the concentration of CCN (Karydis et al. 2011). Garrett et al. (2003) uses a one-dimensional column model and finds that carbonaceous, sulfate, and nitrate aerosols contribute up to 1/3 of the aerosol optical depth over the tropical North Atlantic Ocean during dust events. The drier air of the SAL can also inhibit convective growth. Aerosols in the southwestern parts of North America could be dust as well. If increased dust is acting to inhibit convective growth, lower percentages of RPFs with 30 dBZ echo tops above 6 km would be expected in the Atlantic and NAM regions, while invigoration of the cloud by smoke particles would lead to higher percentages in the Amazon and Africa regions.

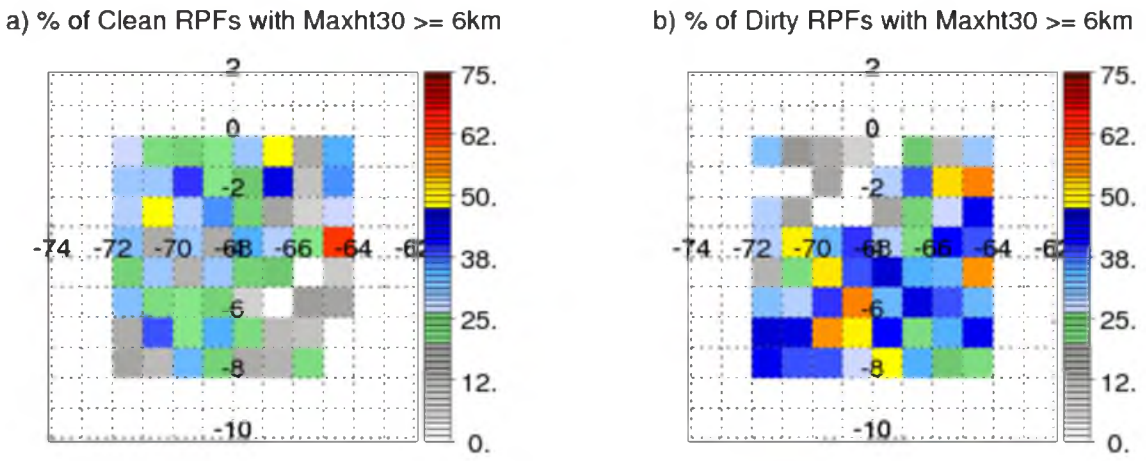

Figure 16: The percentage of features (in color) in the Amazon Region in a) clean and b) dirty environments with maxht30 > 6 km. in 1-degree bins.

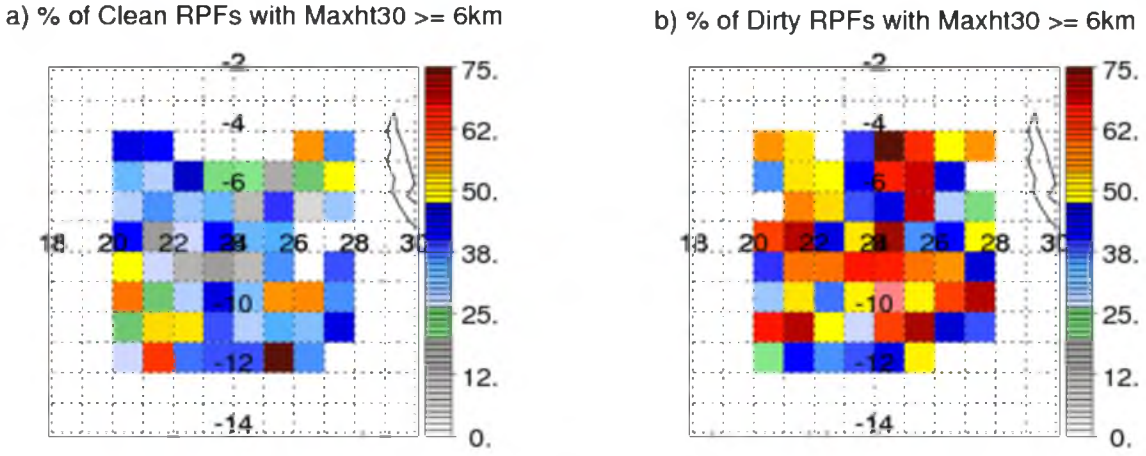

Figure 17: The percentage of features (in color) in the Africa Region in a) clean and b) dirty environments with maxht30 > 6 km. in 1-degree bins.

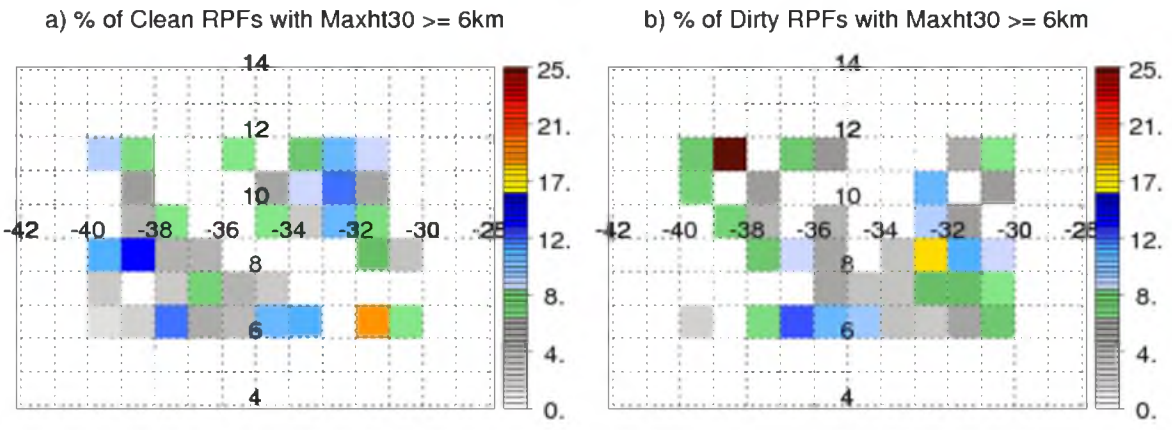

Figure 18: The percentage of features (in color) in the Atlantic Region in a) clean and b) dirty environments with maxht30 > 6 km. in 1-degree bins.

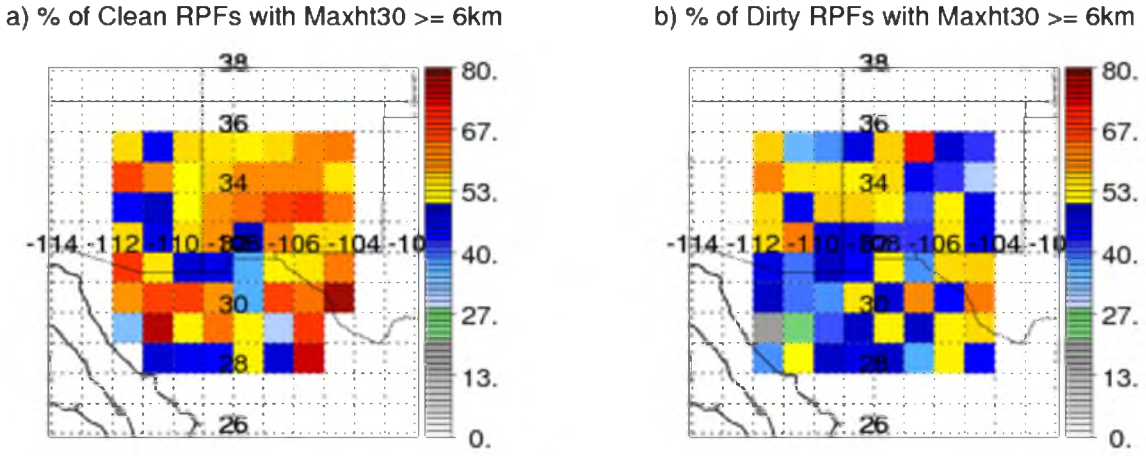

Figure 19: The percentage of features (in color) in the NAM Region in a) clean and b) dirty environments with maxht30 > 6 km. in 1-degree bins.

This idea can be examined further by looking at reflectivity profiles, shown in Figures 20-23. Dots on the lines indicate where the differences between clean and dirty are statistically significant. The Amazon and Africa regions are shown in Figures 20-21, and in both of these regions, dirty features have higher values of reflectivity and taller tops for the top 10%, median, and bottom 10% of profiles. The Africa region has larger differences than the Amazon region. Figures 22-23 show the Atlantic and NAM regions, which show that clean features have the same or higher reflectivities. For these regions, the largest differences appear for median reflectivities, with the top and bottom 10% nearly the same. The differences in reflectivity profiles for the Amazon and Africa regions match the modeling results of Storer et al. (2013) very closely.

Another way of determining influence of aerosols on convection is precipitation rate. Koren et al. (2012) found more intense rain rates in convection in dirty environments. A histogram of mean precipitation rate (determined using number of pixels from the TRMM PR and the volumetric rainfall) with CAPE and MODIS AI is shown in Figure 24. Again, the regions have different responses to increasing aerosols. The Amazon and Africa regions (panels a and b) show higher mean rain rates for higher values of AI. The Atlantic, again being an oceanic region with convection with ocean properties, has very low mean precipitation rates. No pattern is discernable in the NAM region. Two-dimensional Kolmogorov-Smirnov tests of the aerosol index and rain rate for populations of clean and dirty RPFs show that the populations almost certainly come from different distributions; however, plotting AI and CAPE shows that the two variables are not entirely independent, with Amazon, Africa, the Atlantic, and the NAM regions having linear correlation coefficients of 0.563, 0.643, 0.648, and 0.310, respectively. If

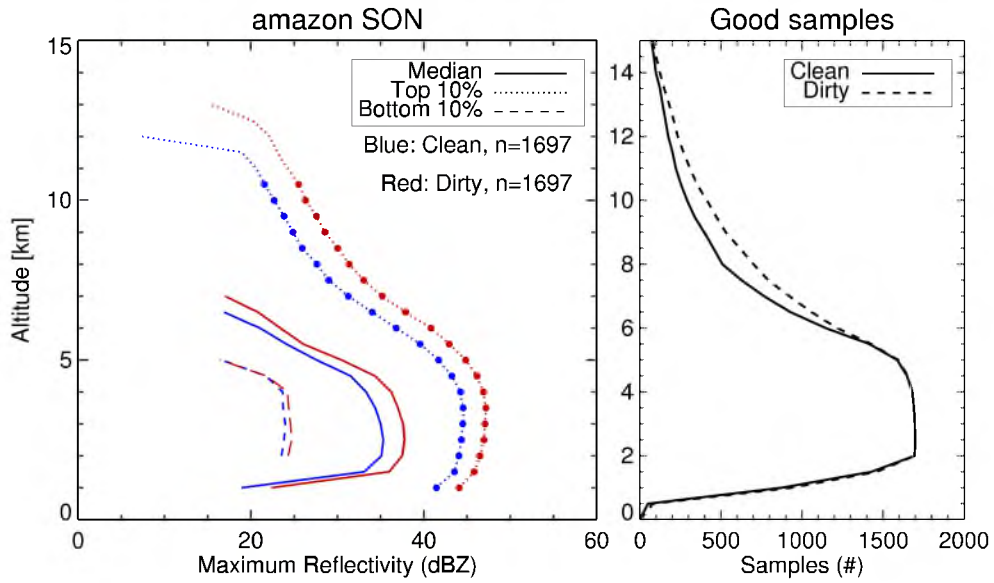

Figure 20: Profiles of bottom 10 % (dashed), median (solid), and top 20% (dotted) reflectivity profiles for clean (blue) and dirty (red) features in the Amazon region during September, October, and November. Number of samples is indicated to the right. Solid circles indicate levels at which the reflectivity distributions are statistically different at a 99% confidence interval using a Kolmogorov-Smirnov test.

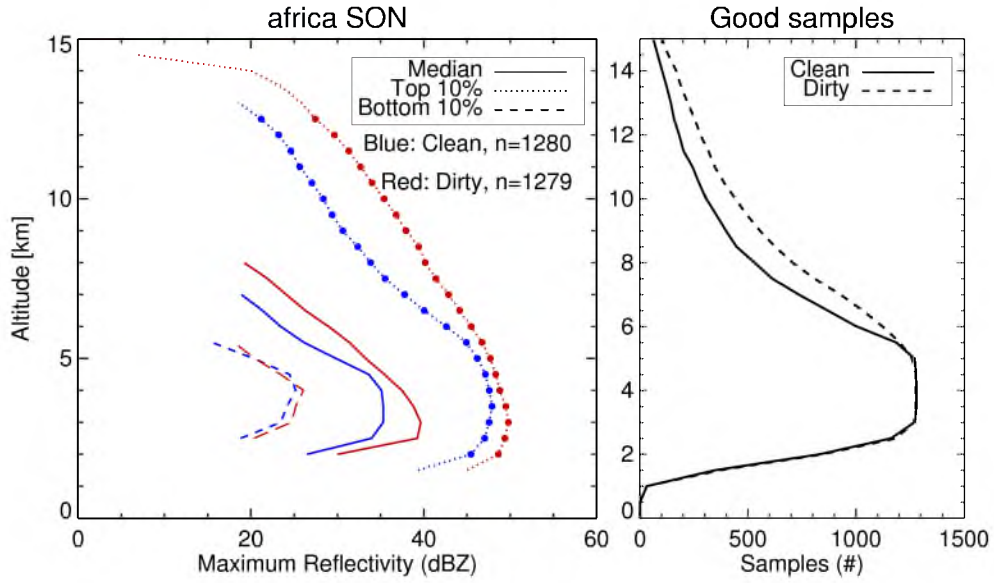

Figure 21: Profiles of bottom 10 % (dashed), median (solid), and top 20% (dotted) reflectivity profiles for clean (blue) and dirty (red) features in the Africa region during September, October, and November. Number of samples is indicated to the right. Solid circles indicate levels at which the reflectivity distributions are statistically different at a 99% confidence interval using a Kolmogorov-Smirnov test.

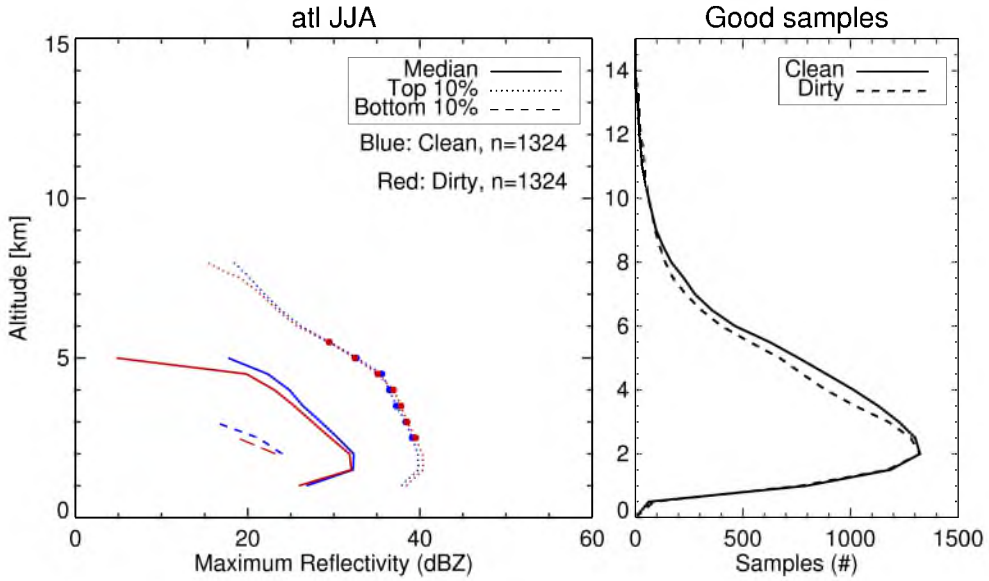

Figure 22: Profiles of bottom 10 % (dashed), median (solid), and top 20% (dotted) reflectivity profiles for clean (blue) and dirty (red) features in the Atlantic region during June, July, and August. Number of samples is indicated to the right. Solid circles indicate levels at which the reflectivity distributions are statistically different at a 99% confidence interval using a Kolmogorov-Smirnov test.

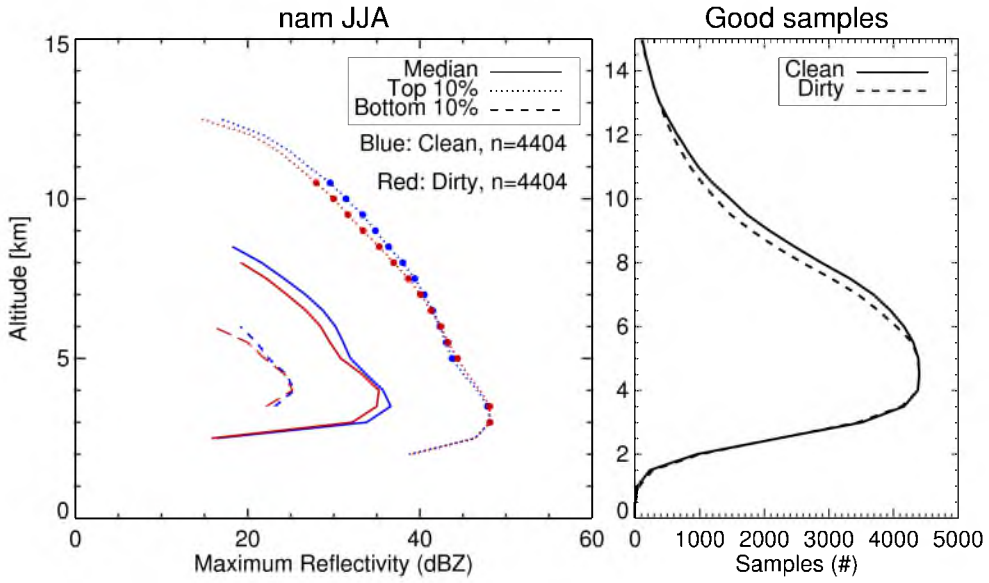

Figure 23: Profiles of bottom 10 % (dashed), median (solid), and top 20% (dotted) reflectivity profiles for clean (blue) and dirty (red) features in the NAM region during June, July, and August. Number of samples is indicated to the right. Solid circles indicate levels at which the reflectivity distributions are statistically different at a 99% confidence interval using a Kolmogorov-Smirnov test.

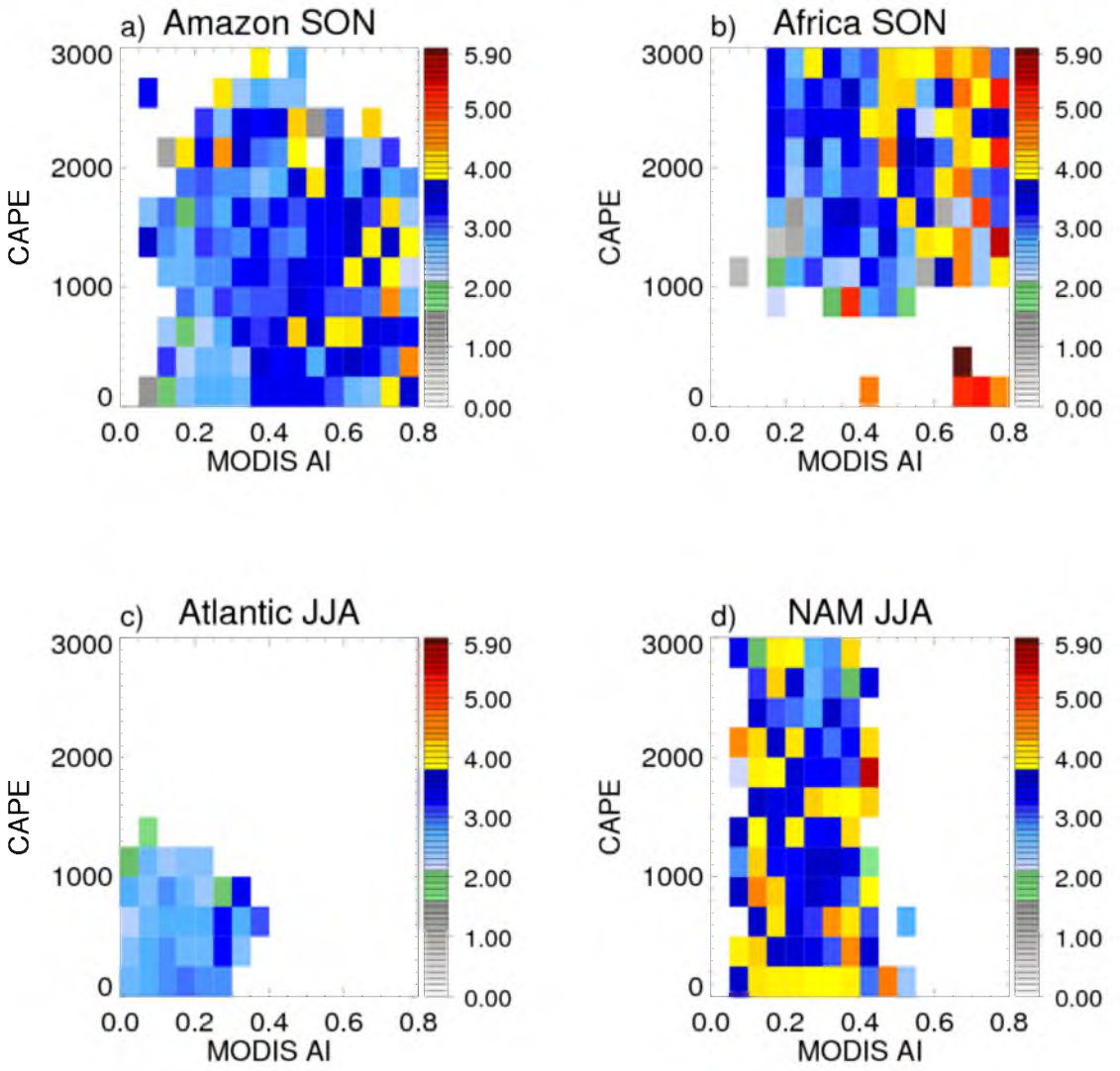

Figure 24: Two-dimensional histograms of mean precipitation rate (in color) for a) the Amazon region, b) the Africa region, c) the Atlantic region, and d) the NAM region. At least 5 samples must be present within the bin.

the environment is correlated with AI, it is impossible to separate AI from the environment.

Effect of the Environment

The preceding results clearly show differences between RPFs occurring in clean and dirty environments. The biggest question regarding the differences in reflectivity and precipitation rate is whether or not these changes are a result of the effects of aerosols or of the thermodynamic environment surrounding the RPF. If the environmental conditions that result in higher aerosol concentration also happen to be more favorable for convection, there is no way to determine whether or not aerosols are causing convective invigoration. Any attempt to answer questions about the aerosol effects must include other aspects of the environment.

The first step in this analysis is looking at wind direction. Wind roses from the ERA-Interim 850 hPa wind associated with each feature are shown in Figure 25. These figures show the number of RPFs in clean and dirty environments from each wind direction for each region. No region has completely separate wind directions for clean and dirty RPFs. The Amazon region has the most notable differences, with cleaner RPFs likely to have more northerly components than dirty RPFs. Africa has only very small differences between clean and dirty. Not surprisingly, given that aerosols in the Atlantic are produced by the SAL, dirty RPFs have more easterly and northerly components than clean RPFs. In the NAM region, both clean and dirty RPFs have a wide range of wind directions. Clean RPFS have a peak in to the southwest, while dirty has a peak to the

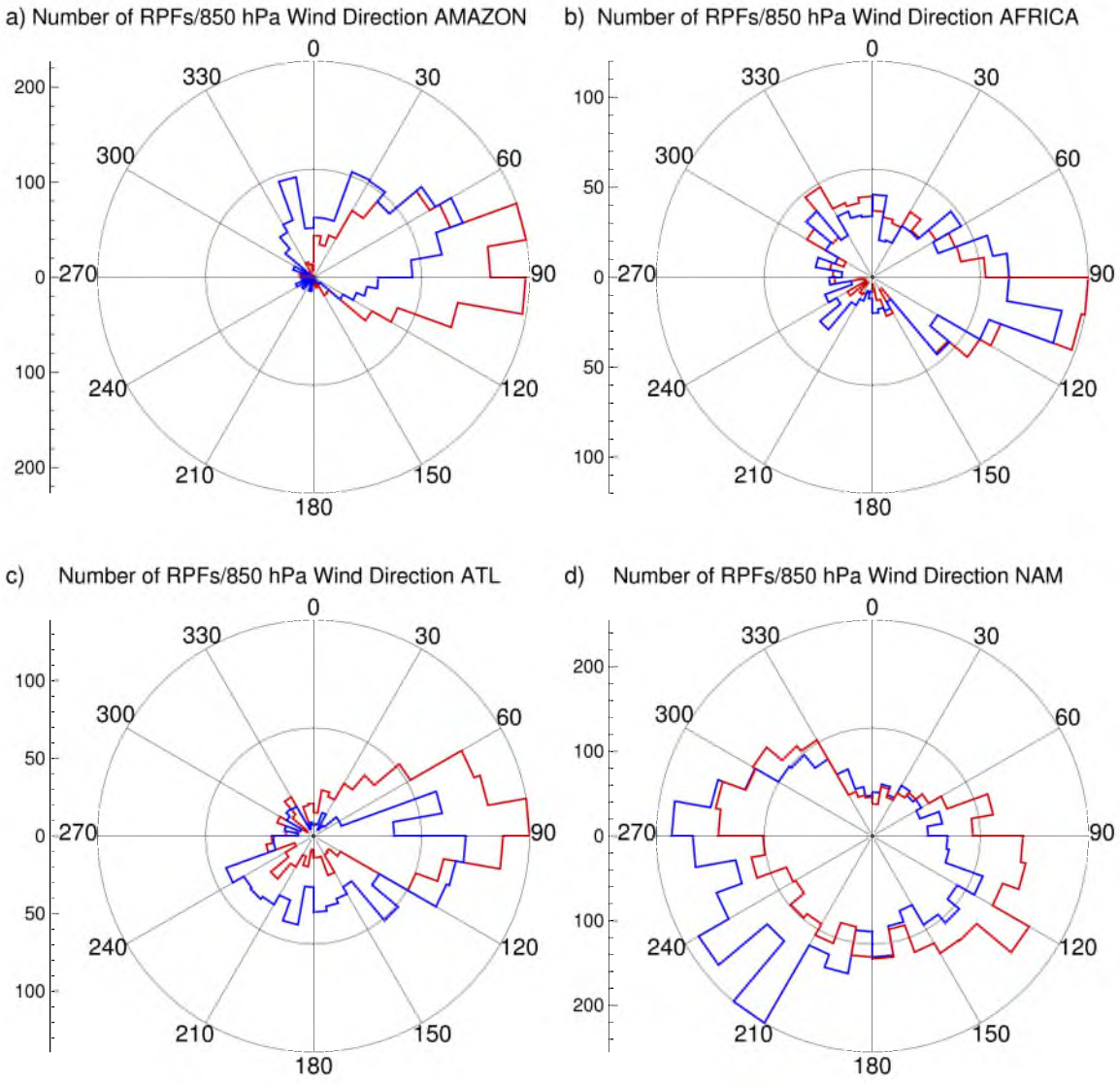

Figure 25: Wind roses showing the number of RPFs in clean (blue) and dirty (red) environments occurring at each wind direction (0-360°). Panel (a) shows the Amazon region, b) is the Africa region, c) is the Atlantic region, and d) is the NAM region.

southeast. Wind from the southeast could transport dusty air from the arid regions of central Mexico

These wind roses do show some differences between the winds in clean and dirty regions, but none of the differences are enough to state that aerosols are consistently transported into any region from one particular direction. In regions of biomass burning, this makes sense because the location of fires changes from year to year. In the Atlantic and Southwest US, where dust is likely to be a primary aerosol, the direction of the dust source may be showing up to a small extent in the dirty cases. The next step of the analysis is to look at mean soundings for clean and dirty RPFs. These figures will show if there are any systematic differences in the thermodynamic environment between clean and dirty RPFs.

Figure 26a shows the soundings for clean and dirty RPFs in the Amazon. The dots on the profiles indicate levels at which mean temperature and relative humidity values are statistically different at the 99% level using a T-test (only mandatory levels are tested). At lower levels, winds in the clean sounding have a more northeasterly component. Easterly winds prevail aloft in both soundings. Temperature profiles stay very similar for both environments, with slightly warmer surface temperatures for clean RPFs. The biggest difference occurs in mid-level moisture, with the dirty environment being drier at mid-levels.

Soundings for the Africa region can be seen in Figure 26b. These two categories show more extensive differences than for the Amazon region, and the differences in means are statistically significant at the 99% level throughout the sounding. Mid-level

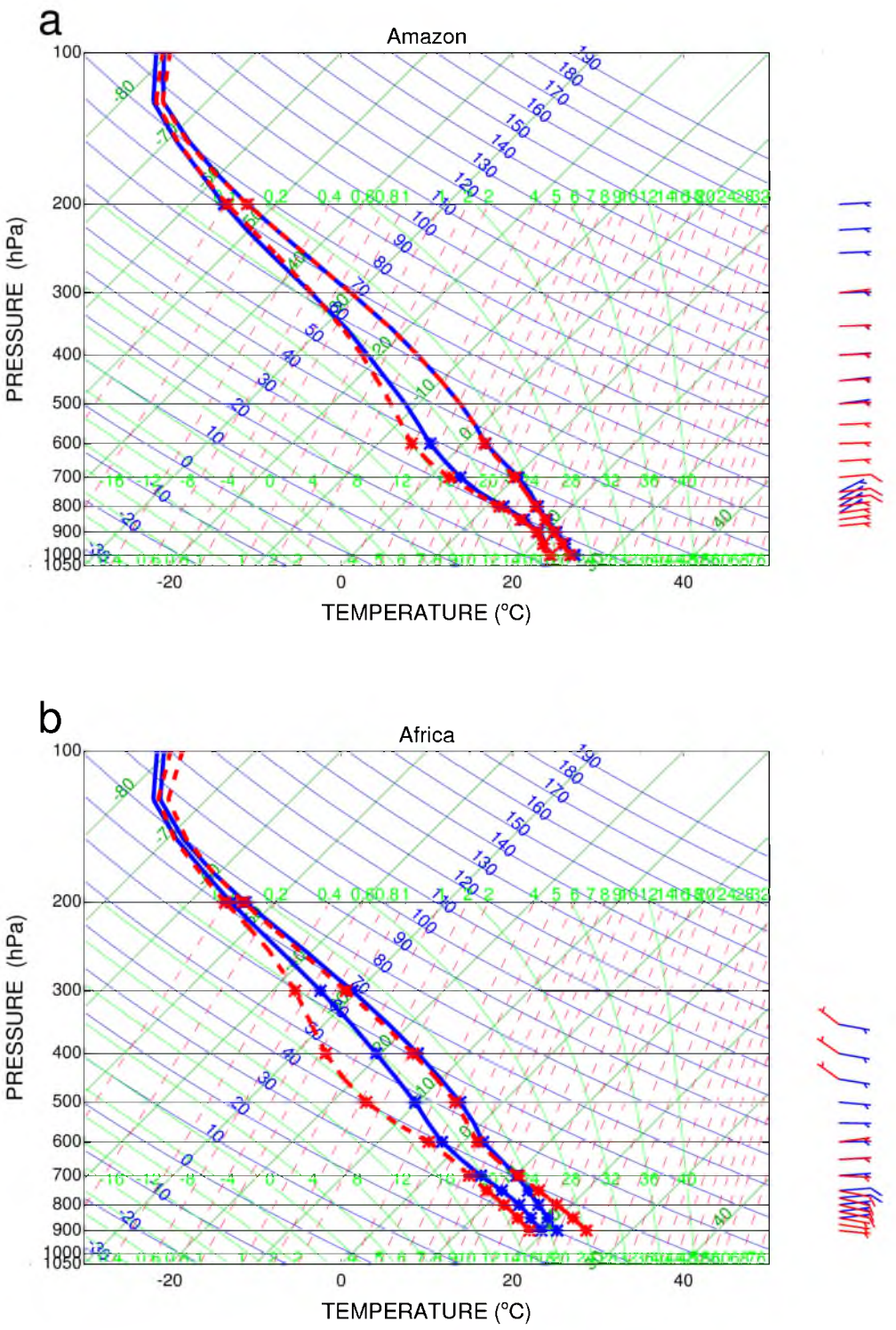

Figure 26: Mean environment soundings from the (a) Amazon region, and (b) Africa region for clean (blue) and dirty (red) features. Solid dots on the plot indicate levels where the means of temperature and relative humidity are significantly different at the 99% level using a T-test

winds for the clean profile display a more easterly component, while the dirty profile has slightly more southerly winds. The surface is warmer in the dirty environment, and the entire profile is drier, particularly between 400-600 hPa. The drier, warmer air in dirty environments could indicate that convection must be more vigorous to survive in this environment and therefore will grow taller. If the environment is more favorable for convection in clean cases, RPFs may be weaker and more widespread (which in turn could rain out aerosol and further clean the environment).

Differences between the mean clean and dirty environments in the Atlantic region, shown in Figure 27a, are not as extreme as those in the Africa region and are only significantly different at the 99% level at a few levels. A slight drying between 700-250 hPa can be seen in the dirty sounding. Low-level winds are also slightly stronger in the dirty environment than those in the clean environment. This region shows the smallest differences between clean and dirty environments. The "dirty" environments in the Atlantic are not as aerosol-rich as "dirty" environments over the continental regions. Aerosols can affect temperature profiles through absorption of radiation, so it is possible that a lesser number of aerosols results in smaller changes in the environment, leading to smaller differences between the profiles.

In the NAM region, Figure 27b, the dirty environmental profile is more moist throughout, with slightly cooler surface temperatures. The profiles are statistically different at the 99% level from the surface to 700 hPa and above 500 hPa. One possible explanation for these differences is the North American Monsoon. During periods of higher moisture, frequent afternoon convection causes gusty outflow winds, which could cause blowing dust. This lofted dust increases the AI and makes the environment dirtier.

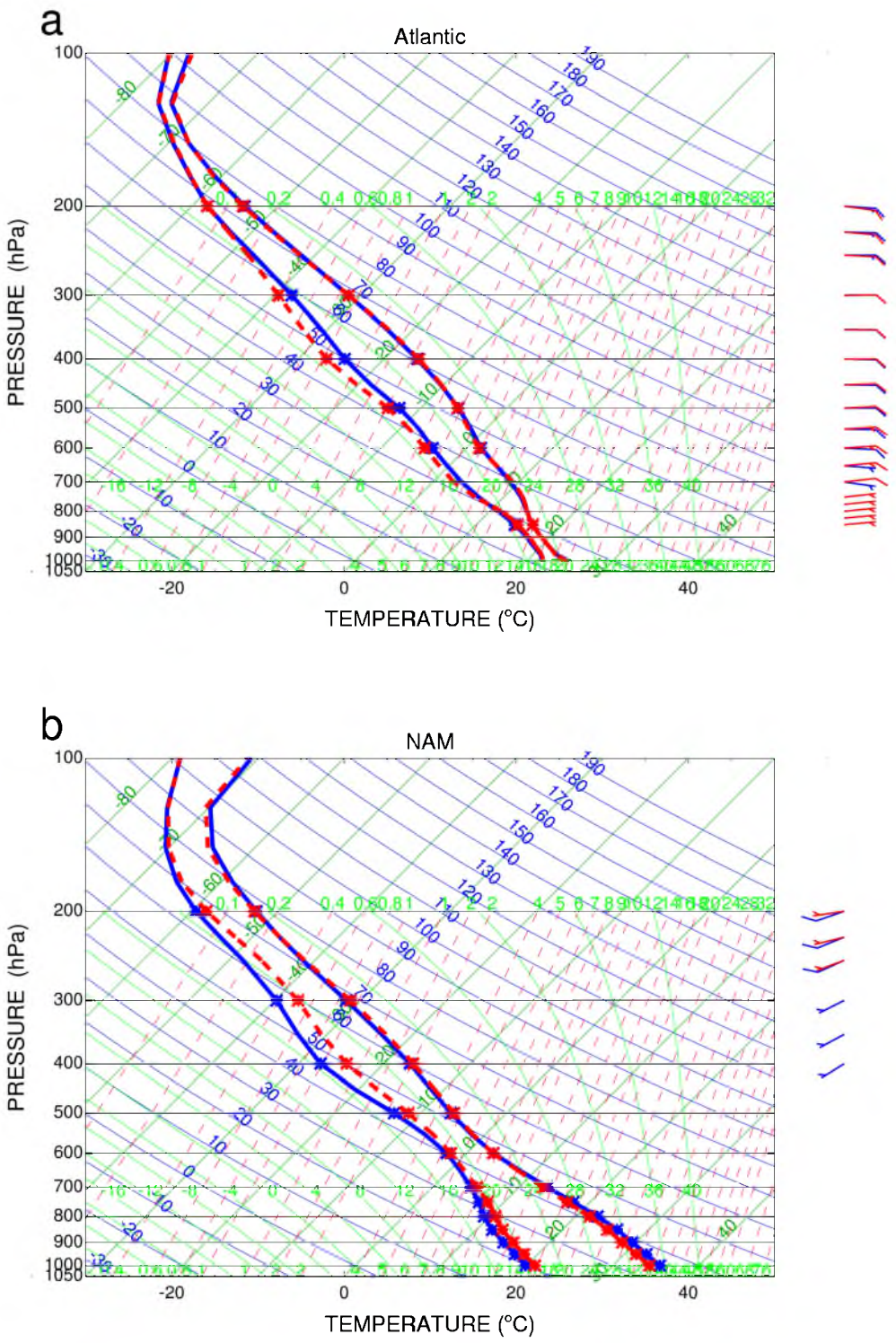

Figure 27: Mean environment soundings from the (a) Atlantic region and (b) NAM region for clean (blue) and dirty (red) features. Solid dots on the plot indicate levels where the means of temperature and relative humidity are significantly different at the 99% level using a T-test.

Interactions with dust and convection are complicated, and the amount of dust ingested by a convective cloud depends on a number of factors (Seigel and van den Heever 2012).

The analysis thus far shows that there are variations in convective intensity between RPFs forming in clean and dirty environments in different parts of the world. Some regions show larger differences in reflectivity profiles from clean and dirty features than others. Some regions seem to show convective invigoration (Amazon, Africa). Other regions seem to show convective inhibition (Atlantic, NAM). Further evaluation of the environments of clean and dirty days shows differences in wind direction in some regions. The African region shows large, statistically significant differences in the thermodynamic environment that could possibly explain differences in convection on clean and dirty days, while the Atlantic and Amazon regions have smaller differences that are not always statistically significant and could point to true aerosol effects. These results highlight the complexity of the aerosol problem and the difficulties in separating the effects of aerosols from those of the environment purely from observations. It is not easy to find significant differences between clean and dirty features that are attributable to aerosol indirect effect when these groups are defined by MODIS AI. In each region examined here, significant differences occur at some levels in the mean thermodynamic profiles and prohibit attributing differences in RPFs to aerosol indirect effect alone.

Clean and Dirty Features in Similar Environments

Another approach to attempt to identify the aerosol indirect effect is to find similar environmental profiles and look at the range of AI values within these similar profiles to look for trends in convective proxies with increasing AI. Attempts to cluster

environments using k-means cluster analysis produced unsatisfactory results. Many different variables (CAPE, mid-level relative humidity, wind shear vector, and temperature, dewpoint, wind speed, and wind direction at multiple levels) were used to cluster environments, but regardless of the variables used, the groups defined by the algorithm did not represent distinct environments. Manual binning of environmental parameters provides one way to look at RPFs occurring in similar environments, but limits the number of variables to two at a time.

Figures 28 and 29 show the results of binning the environments in the Amazon (Figure 28) and Africa (Figure 29) by mid-level relative humidity and either surface to 700 hPa shear vector (panel a) or CAPE (panel b). The original Amazon and Africa regions did not have a large enough sample size to subdivide the environments this many times, so the areas of both regions were expanded. In order to determine the differences in mean values of parameters for convective intensity (maxht20, maxht30, maxht40, and min85pct), a modification factor was calculated by subtracting the mean value of each parameter for clean RPFs from the mean value of the same parameter for dirty RPFs. These differences were normalized by the standard deviation of the parameter and added together. The difference for min85pct was multiplied by -1, since lower values indicate a more convectively intense storm. Larger values of the modification factor (more blue in the figure) indicate that clean values are larger, and therefore clean RPFs are more intense. Values less than 0 indicate that dirty RPFs are more intense and appear red. Individual plots (not shown) were constructed for each variable, to ensure that no one parameter is overpowering the others.

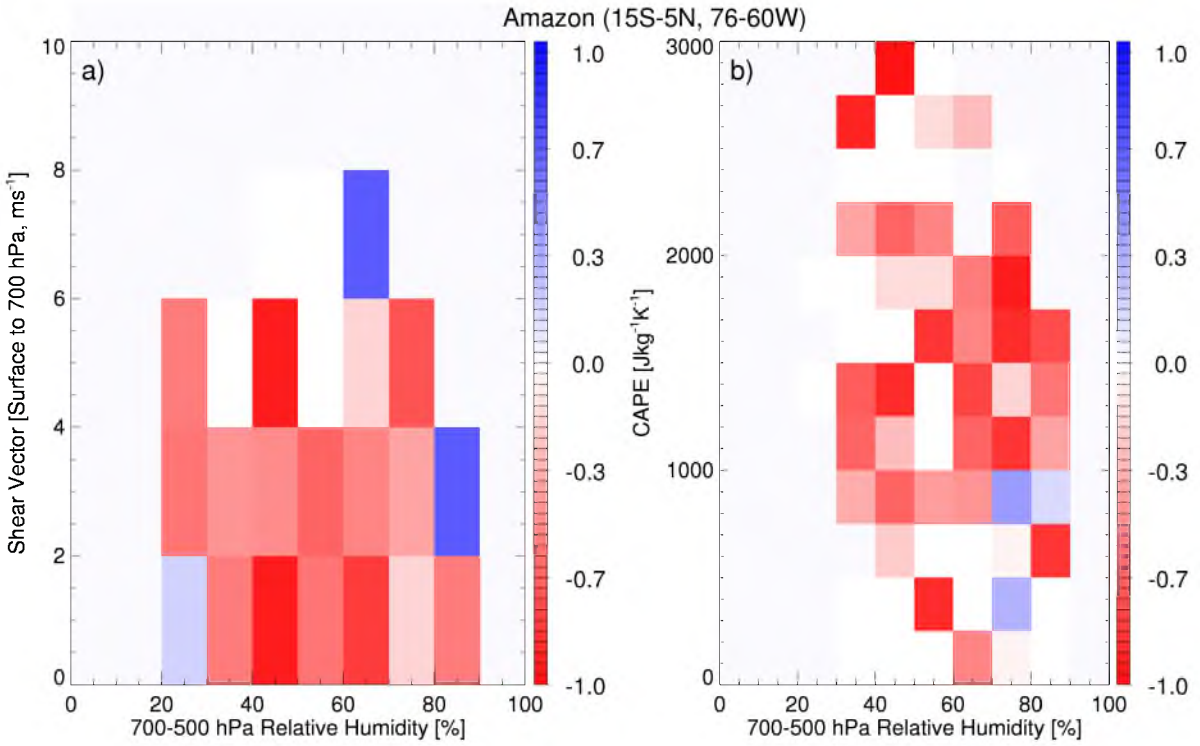

Figure 28: The modification parameter binned by 700-500 hPa mean relative humidity and a) surface-700 hPa shear vector or b) CAPE for the Amazon region, which in this figure is extended to 15°S-5°N and 76-60°W. Increasingly dark shades of red (blue) indicate increasing intensity of dirty (clean) RPFs.

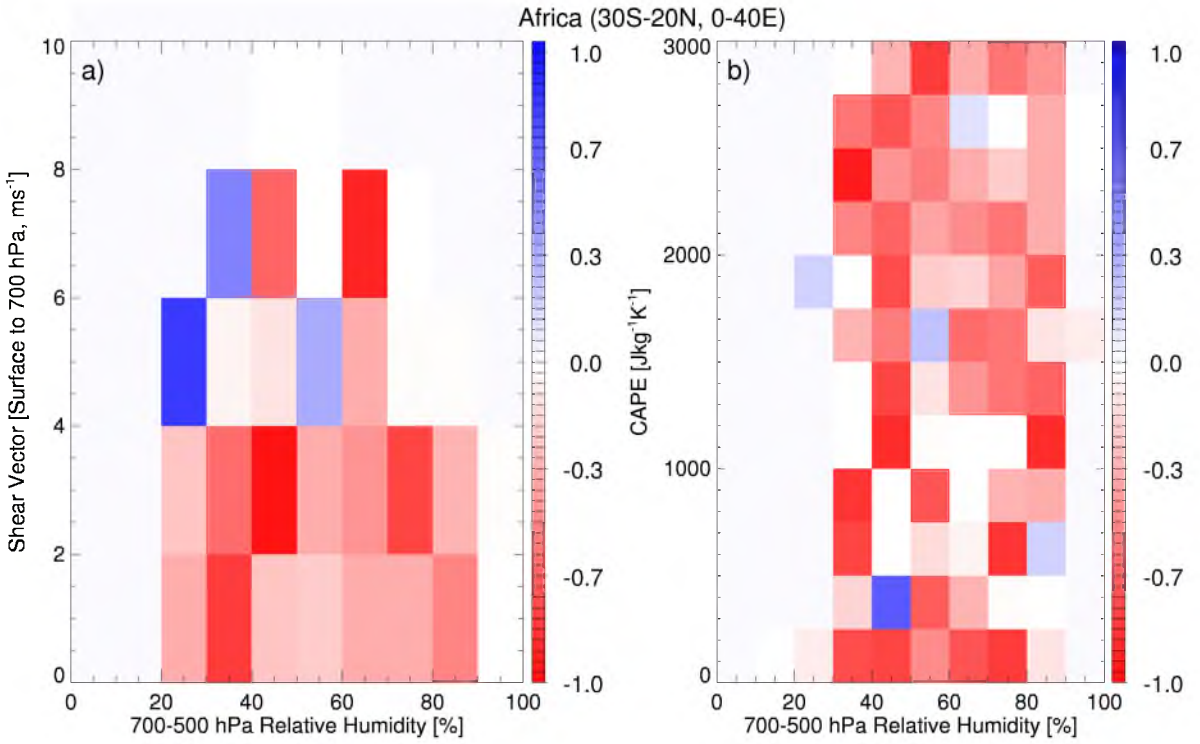

Figure 29: The modification parameter binned by 700-500 hPa mean relative humidity and a) surface-700 hPa shear vector or b) CAPE for the Africa region, which in this figure is extended to 30°S-20°N and 0-40°E. Increasingly dark shades of red (blue) indicate increasing intensity of dirty (clean) RPFs.

These figures show that overall, regardless of environment, dirty RPFs tend to be more intense. This result is not surprising, given prior results showing that dirty RPFs have higher echo top heights. Most of these proxies for intensity used here are directly related to reflectivity. These figures show no preferred environment for invigoration. There are no systematic patterns to suggest that the TRMM RPFs will be modified more in regions of low CAPE or low shear, as has been seen in modeling studies (Lee et al. 2009, Fan et al. 2009).

A further examination of the distributions of these parameters by plotting CDFs, which have the additional advantage of showing the entire distribution, in different environments (not shown) also displays no systematic differences in the distributions of maxht20, maxht30, maxht40, min85pct, and area. Thus, this analysis finds no evidence to verify the idea that certain environments allow greater modification by aerosols.

CHAPTER 4

DEFINING CONGESTUS

Deep convection alone is a complicated problem, with many storm-scale feedbacks. Larger convective systems have multiple updrafts and downdrafts, which can buffer the signal of aerosol invigoration and make it difficult to observe an aerosol effect. Cumulus congestus, on the other hand, would seem to be a slightly more manageable problem. Congestus occur on a smaller horizontal spatial scale and generally have fewer interacting variables. These types of clouds could have a greater "modifiability" than large convective systems, which are driven more by their environment and localized storm dynamics than by the aerosol effect.

What Are Congestus?

Many previous studies have examined the distribution of clouds in the Tropics. The most studied cloud types have been shallow cumulus and cumulonimbus, or deep convection. Johnson et al. (1999) remind us that there are three prominent cloud types in the Tropics: shallow cumulus, cumulonimbus, and *congestus*. Congestus have not seen as much attention, perhaps due to the varied definitions of this cloud type. Congestus is considered to range from tall, skinny building cumulus to large clouds that extend above

the freezing level but do not meet cumulonimbus criteria. The American Meteorological Society glossary defines congestus as "A strongly sprouting cumulus species with generally sharp outlines and, sometimes, with a great vertical development; it is characterized by its cauliflower or tower aspect, of large size" (Glick 2000). This definition leaves considerable room for interpretation.

Studies from past field campaigns show the impact of congestus on climate in the Tropics. Congestus with tops between 4.5 and 9.5 km produced 57% of the precipitation occurring from convective clouds in the Tropical Ocean Global Atmosphere Coupled Ocean Atmosphere Response (TOGA COARE) Experiment, and these same clouds contribute 28% of the total convective rainfall over the west Pacific warm pool (Johnson et al. 1999). Stephens and Wood (2007) found that the typical mode of convection producing precipitation at the Manus Atmospheric Radiation Measurement (ARM) site is congestus-like convection underlying higher layers of cirrus clouds. Their study analyses over 825,000 radar profiles in the tropics to find that the biggest change between different regimes of synoptically-forced convection was the occurrence of different storm types rather than cloud and precipitation structure. Storm class E from their study, with precipitation echo top heights between 4-6 km, is similar to the definition of congestus we will use in this study.

Congestus are also thought to play an important role in preconditioning the environment for deeper convection (Johnson et al. 1999), and this moistening may be very important in advancing the Madden Julian Oscillation (MJO) from developing to mature stage (Kikuchi and Takayabu 2004). Waite and Khouider (2010) use a cloud resolving model to show that detrainment of water vapor from congestus can moisten the

lower troposphere. Riley et al. (2011) use Cloudsat to classify congestus, and do not see dramatic differences in congestus population during different stages of the MJO. Hohenegger and Stevens [2013] find that cumulus congestus transition to deep convection too quickly for congestus clouds to sufficiently moisten the atmosphere, and Takayabu et al. [2010] find parts of the world, particularly the east Pacific ITCZ, that have significant quantities of rainfall from congestus, but little rain from deeper convective features. The relationship between population of congestus and preconditioning for deeper convection remains unclear.

Jensen and Del Genio (2006) examine the relationship between the environment and congestus at the ARM Nauru site and find that drying in the mid-troposphere is more likely to be responsible for limiting congestus cloud-top heights than stability of the freezing layer. Takemi et al. (2004) found that in the West Pacific mid-level moisture is the biggest difference in environmental soundings when comparing instances where congestus were able to develop to days on which only shallow cumulus occur. Environment has an important impact on where congestus form, and differences in cloud properties could result from regional variations in humidity and temperature fields.

These studies of congestus are necessarily limited in scope because they rely on data from field experiments or stationary ground-based instrumentation with data from limited locations or time periods. Other studies (Luo et al. 2009, Casey et al. 2011) use CloudSat. Luo et al. (2009) use reflectivity profiles from the CPR to determine whether or not congestus observed by a CloudSat overpass will continue to grow vertically ("transient convection") or will cease growth ("terminal convection"). An analysis of data between 15°S and 15°N from 2007 shows that a significant fraction of tropical congestus

will continue to grow. Another congestus study by Casey et al. (2011) uses the CloudSat cloud classification product to group convective clouds into cloud features. They describe the characteristics of cloud- and echo-top height in oceanic congestus in the tropics from 2008. Around 31% of the convective features they identified meet the criteria for congestus clouds used by Luo et al. (2009).

CloudSat allows the investigation of congestus globally. However, the increase in spatial coverage is offset by a lack of temporal resolution. Its sun-synchronous orbit results in two overpasses per day at 0130 and 1330 local time. Because of this orbit, obvious difficulties arise when using CloudSat to examine any convective phenomenon. It is well known that there is a distinct diurnal cycle of convective clouds, which differs over land and ocean (Hall and Vonder Haar 1999, Yang and Slingo 2001, Liu and Zipser 2008). This diurnal cycle paired with the timing of the afternoon CloudSat overpass questions the representativeness of climatology of clouds generated by CloudSat (Liu et al. 2008).

TRMM is not sun-synchronous and can observe the diurnal cycle of convection.. TRMM carries the Visible and Infrared Scanner (VIRS) in addition to the PR. VIRS provides the traditional infrared image that can be used to identify different types of clouds (Rossow et al. 1991). In addition to the horizontal cloud area indicated by the VIRS, the PR actively detects the vertical structure of precipitation with a minimum detectable signal of 18 dBZ, corresponding to light rain under these clouds. A combination of observations from these two satellites will be used to provide details about the global distribution and properties of congestus from different perspectives.

With TRMM and CloudSat, the typical locations of congestus as well as cloud properties and how they vary over the globe can be observed.

Using more than 4 years of CloudSat and 14 years of TRMM observations, this chapter addresses the following questions:

- Where do congestus occur globally? What contribution do these congestus make to global cloud cover and precipitation?
- How does the global occurrence of congestus change seasonally and during day and night?
- What are the typical properties (size, height, thickness, reflectivity profile) of congestus? Do these properties change over different regions, especially over land and ocean?

Congestus Using CloudSat

Many definitions of congestus have appeared in previous publications. Congestus are easy to identify visually. Figure 7 (particularly panels (a) and (b)) of Johnson et al. (1999) show some examples of congestus clouds. When using radar data to identify congestus clouds, definitions vary by study. Jensen and Del Genio (2006) state that congestus should have a cloud base near the lifting condensation level (LCL), heights near the freezing level, a lack of significant ice hydrometeors, and precipitation reaching the ground. A cloud top height restriction selects clouds with tops above the typical freezing level in the Tropics (4.75 km), but not high enough to be dominated by ice processes. Figure 1 of Jensen and Del Genio (2006) shows a pronounced peak in occurrence of clouds with CTH between 5 and 7 km. In our study we expand this upper

limit to 8 km in order to capture the peak in cloud top occurrence between 7-8 km observed by Riley and Mapes [2009]. Luo et al. (2009) identify congestus in CloudSat data by requiring a CloudSat cloud top height (CTH) between 3-9 km, a continuous radar echo from CTH to the ground, 10 dBZ echo top height (ETH) within 2 km of the CloudSat CTH, 0 dBZ ETH within 1 km of the CloudSat CTH, and the Calipso CTH within 1 km of the CloudSat CTH. Casey et al. (2012) utilize a similar definition, requiring CTH between 3-9 km, cloud base within 1 km of the surface, and a definition of "cumulus" or "deep convection" in the CloudSat cloud classification product.

In this study the University of Utah CloudSat Database was used to identify congestus globally. This database spans 5 years from 2006-2011 and uses the 2B-GEOPROF product to identify clouds. Cloud features are identified by grouping contiguous pixels with reflectivity of at least -28 dBZ and a cloud mask greater than 20. Cloud mask is included in the 2B-GEOPROF product and represents the likelihood that a cloud is actually detected by the CPR. The properties of each cloud feature, including maximum cloud top height, vertical profile of width and maximum reflectivity in the cloud are summarized. Figure 30a and 30b show two examples of congestus clouds over land and ocean, respectively, with contoured CloudSat reflectivity. One difficulty in defining congestus in this way is to separate adjacent congestus clouds adjoined by an area of low reflectivities (e.g., Figure 30c), making it impossible to separate individual congestus. Congestus are often seen as smaller than the examples in Panels (a) and (b). The resolution of both CloudSat and TRMM smears individual clouds together, creating seemingly larger congestus than one may expect. The profiles of these congestus clouds, as seen in Figure 30, can be thought of as "cloud envelopes" in which a number of

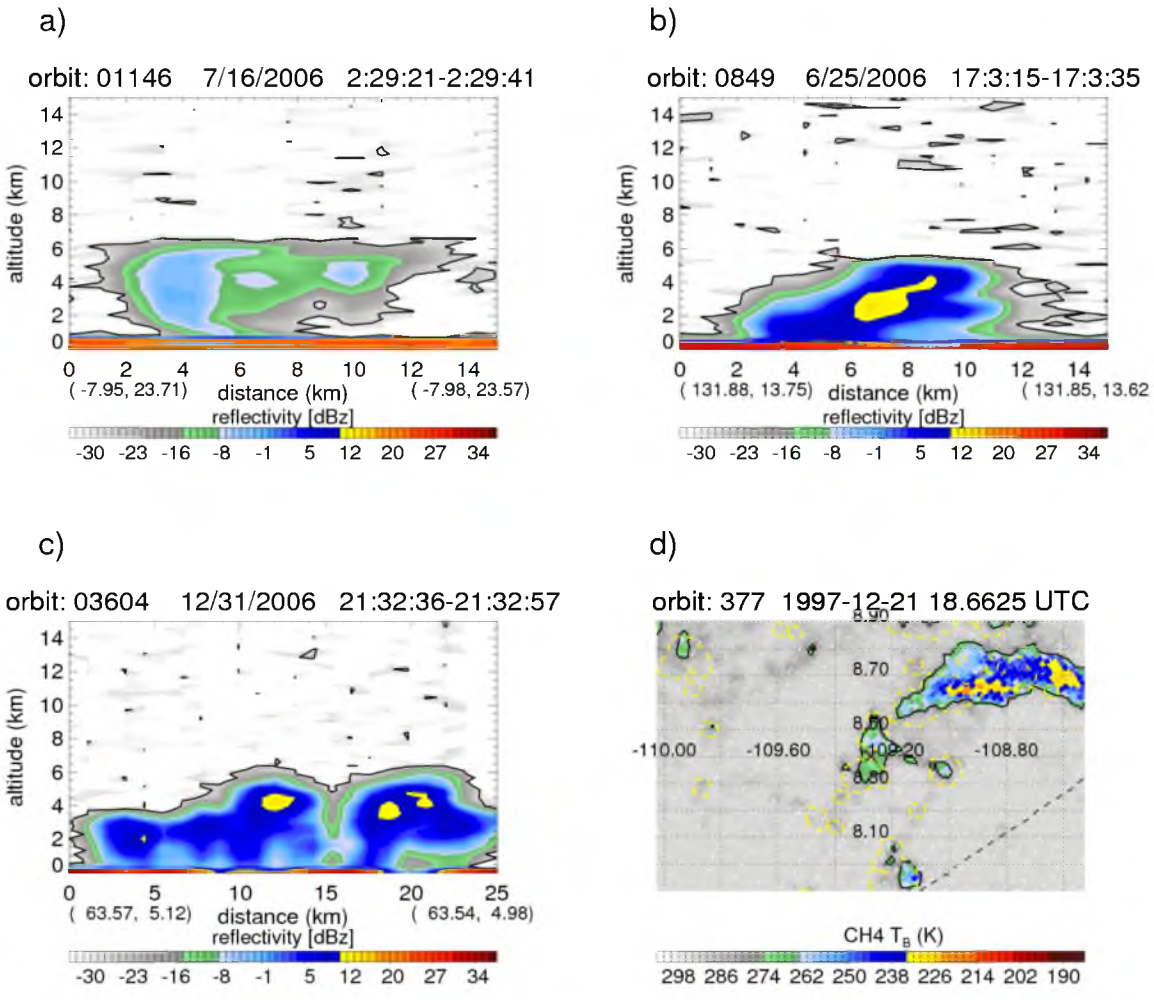

Figure 30: Panels (a)-(c) show examples of congestus identified by CloudSat over Africa, the west Pacific and Arabian Sea. Reflectivity is contoured in color, with the dark black lines outlining -28 dBZ, which is the CloudSat minimum detectable signal. Titles above the figure show the date and time of the overpass. Panel (d) shows an example of a TRMM VIRS cloud feature over Africa (denoted by 'X'), with T_{B11} contoured in color. The black contour is 273 K. Dashed lines indicate the edges of the TRMM precipitation radar overpass. Yellow dashed lines indicate areas with near surface rainfall above 0.

smaller congestus clouds are grouped close together, with individual turrets in the 2-4 km range in width.

The first step of this study is to subset the congestus clouds from the whole cloud database. The method used to identify congestus is subjective and was derived through multiple iterations of selecting criteria and examining features. Congestus are restricted to clouds with maximum cloud tops between 5-7 km, following the range of congestus cloud top shown by Jensen and Del Genio (2006). Van den Heever et al. (2011) also found a congestus mode in their radiative convective equilibrium model between 4-7 km. Cloud bottom is required to be less than 1.5 km above the terrain height to somewhat ensure surface precipitation. It should be noted that the cloud base is ambiguous in the event that rain is falling from the cloud. The Cloudsat CPR sees both cloud and rain. At some reflectivities inferences can be made as to whether a cloud is precipitating, but for the remainder of this study, cloud echo base is used to bypass the problem of separating rain from cloud. If a congestus is raining, the cloud echo base would be the lowest level at which rain is detected. This problem will be discussed further later in this chapter.

Congestus must have a maximum reflectivity reaching -5 dBZ, thickness of at least 4 km, and a horizontal (along track) width of less than 30 CloudSat pixels (33 km). Additionally, in order to compare CloudSat to TRMM observations, only congestus between 36°S and 36°N are examined. Some of the congestus selected using this method have overlying cirrus layers. Investigation of a subset of congestus showed that these overlying layers typically had low reflectivities and therefore these cases were not excluded from our congestus population.

Congestus Using TRMM

As previously mentioned, CloudSat's sun-synchronous orbit may skew the climatology if there is a strong diurnal variation of clouds. In order to determine the impact of diurnal sampling, we use cloud features from the TRMM cloud and precipitation feature database (Liu et al. 2008). In this database, cloud features are identified by grouping contiguous pixels of VIRS 11 μm brightness temperature (T_{B11}) colder than 273 K. Then the size of the cloud, minimum T_{B11} and rainfall indicated by TRMM PR inside cloud feature are summarized. To subset congestus, the cloud features with minimum infrared T_{B11} between 260-273 K and area less than 200 km^2 are identified as candidates cloud features. These temperatures correspond to approximately 6.8-4.75 km based on climatological tropical soundings. Non zero surface rainfall is required for a candidate cloud feature to be counted as a congestus. This removes many samples with low reflectivity due to TRMM's minimum detectable signal of 18 dBZ. At the same time, this reinforces the definition as congestus of above average convective intensity, with relatively higher radar echoes. Many congestus do not produce rain, and these would be omitted from our sample. Thus our population represents only the strongest congestus. Features occurring in the winter hemispheres from 20°-36° are omitted from the population in order to exclude the large number of cold winter clouds and cold surfaces over mountains that fit the T_{B11} criteria. Fourteen years (1998-2011) of TRMM data provide a large enough sample size to have a statistically robust dataset for the entire diurnal cycle, so the VIRS congestus features will be used in the following sections to compare to CloudSat congestus to determine the effect of the CloudSat orbit on sampling.

Panel (d) of Figure 30 shows a plan view of one large area of cloud with infrared T_{B11} between 260-273 K and some isolated TRMM VIRS "congestus" clouds. The dark black lines show the boundaries of the features. By looking at the visual band from VIRS (not shown), it can be seen that the center cloud is a field of congestus, similar to what we see in Panel (c) but with larger horizontal extent adjoined by many small congestus clouds. The resolution of the TRMM satellite (5 km footprint) is larger than that of the CPR, meaning that VIRS is only able to resolve fields of congestus such as this. As with CloudSat, individual congestus are not resolvable.

Global Distribution of Congestus

In total, 105,471 congestus clouds and 4,708,864 cloud features with infrared T_{B11} ranging 260-273 K are separately identified from 5 years (June 2006 - April 2011) of CloudSat and 14 years (1998-2011) of TRMM observations. Figure 31 shows the global distribution of CloudSat congestus and TRMM VIRS congestus features. Panels (a) and (b) compare CloudSat congestus and TRMM congestus that occur within 30 minutes of the CloudSat overpass. These two figures are similar, lending confidence to our TRMM VIRS definition of congestus. Panel (c) also shows the relative frequency of TRMM VIRS congestus, but all times are included.

Including the entire diurnal cycle (panel c) lessens the maxima seen over the Amazon and the West Pacific but enhances the East Pacific Intertropical Convergence Zone (ITCZ) and the northern Atlantic. TRMM VIRS does not capture the maxima in congestus over Africa well. This likely occurs because congestus must have surface rainfall when defining VIRS congestus. There is lower fraction of congestus candidates

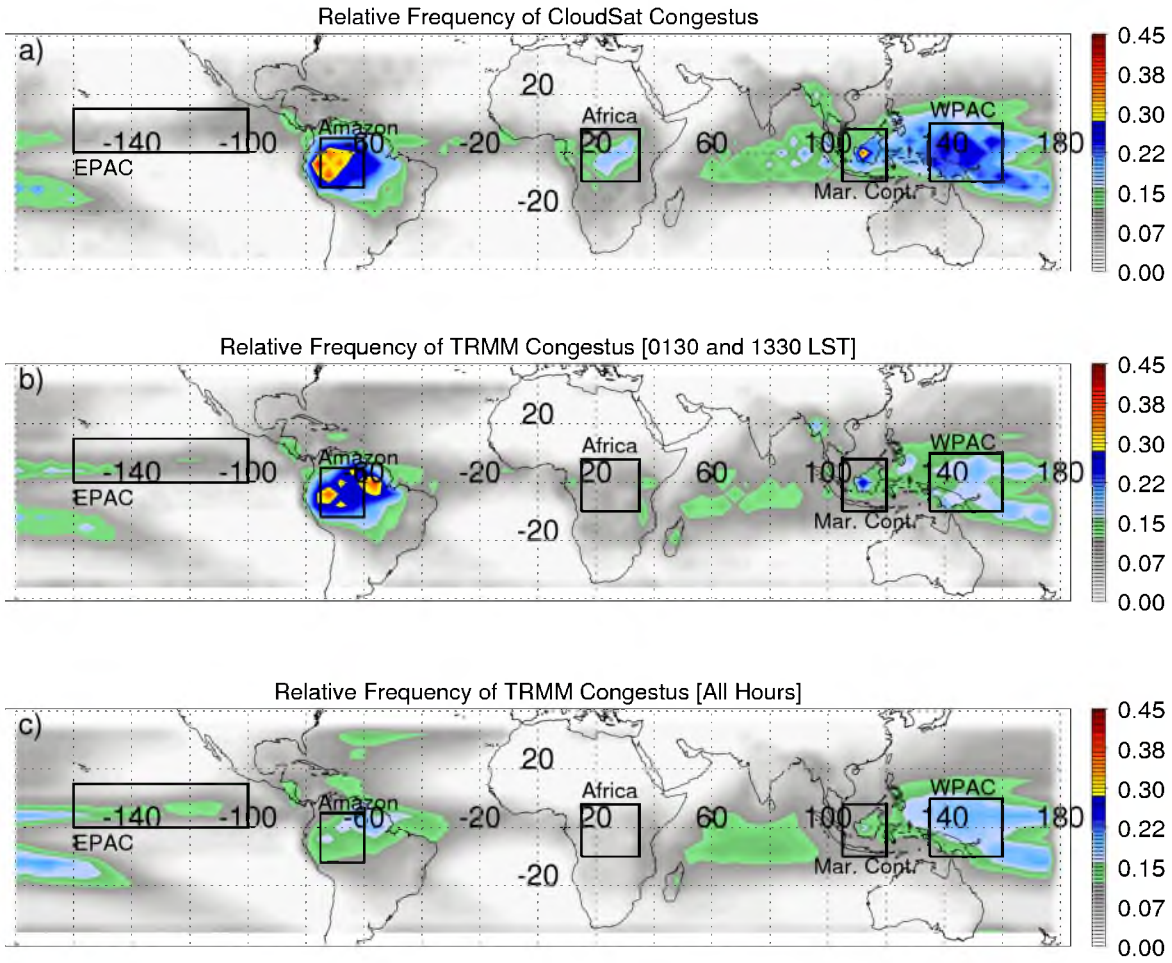

Figure 31: The relative frequency (contoured in color) of (a) CloudSat congestus, (b) TRMM VIRS congestus occurring within 30 minutes of the local CloudSat overpass time, and (c) all TRMM VIRS congestus. Black boxes denote regions of interest.

(clouds with infrared T_{B11} at 260-273 K) having surface rainfall over Africa (5.1%) than other regions, e.g., over the Amazon (13.5%). The features with no surface rainfall over Africa get excluded. The distribution of congestus over the Pacific and Indian Oceans corroborates the distribution found in Casey et al. (2012). The difference between Figure 31b and 31c suggest a significant diurnal variation of congestus over the Amazon. The high fraction of congestus clouds over the Amazon in Figure 31a is partially due to the sampling of CloudSat and would not be so significant if CloudSat could observe the full diurnal cycle of convection in the region.

Five different regions are displayed with black boxes in Figure 31. These regions, the East Pacific, West Pacific (ocean only), Amazon, Africa, and Maritime Continent (land only) will be utilized to look at differences in congestus over different regions. A variety of land and ocean regions were chosen, as important differences in convection have been shown to occur over land and ocean (Zipser and LeMone 1980, Zipser and Lutz 1994, Robinson et al. 2011).

Contribution of Congestus

One of the most important questions regarding congestus clouds is how much they contribute to the cloud population. Johnson et al. (1999) found that while congestus did not produce as much rain as cumulonimbus, the rain from congestus still accounts for a large amount of the precipitation falling in the west Pacific warm pool. The contribution of congestus to the total CloudSat cloud population is summarized for individual regions in Table 2 and shown globally in Figure 32. Figure 32a shows the percent of all clouds that are congestus, while Figure 32b shows the percent of clouds

Table 2: Regional Contributions of Congestus to Area and Rain Volume. Tall clouds are clouds with maximum cloud top above 12 km. The rain fraction is calculated using the precipitation rate retrieved from TRMM radar reflectivity.

	Percent of All CloudSat Clouds That Are Congestus [%]	Percent of Low CloudSat Clouds That Are Congestus [%]	Mean Ratio of Area of CloudSat Congestus to Area of Tall CloudSat Clouds	Mean % of Volumetric Rainfall Produced by TRMM VIRS Congestus [%]
All Land	3.04	6.44	0.196	0.770
All Ocean	1.61	2.39	0.211	1.08
EPAC	1.63	2.43	0.145	1.19
WPAC	5.08	10.9	0.177	1.02
Amazon	7.12	14.5	0.261	1.11
Africa	4.71	12.8	0.179	0.423
Maritime Continent	5.22	12.0	0.164	0.997

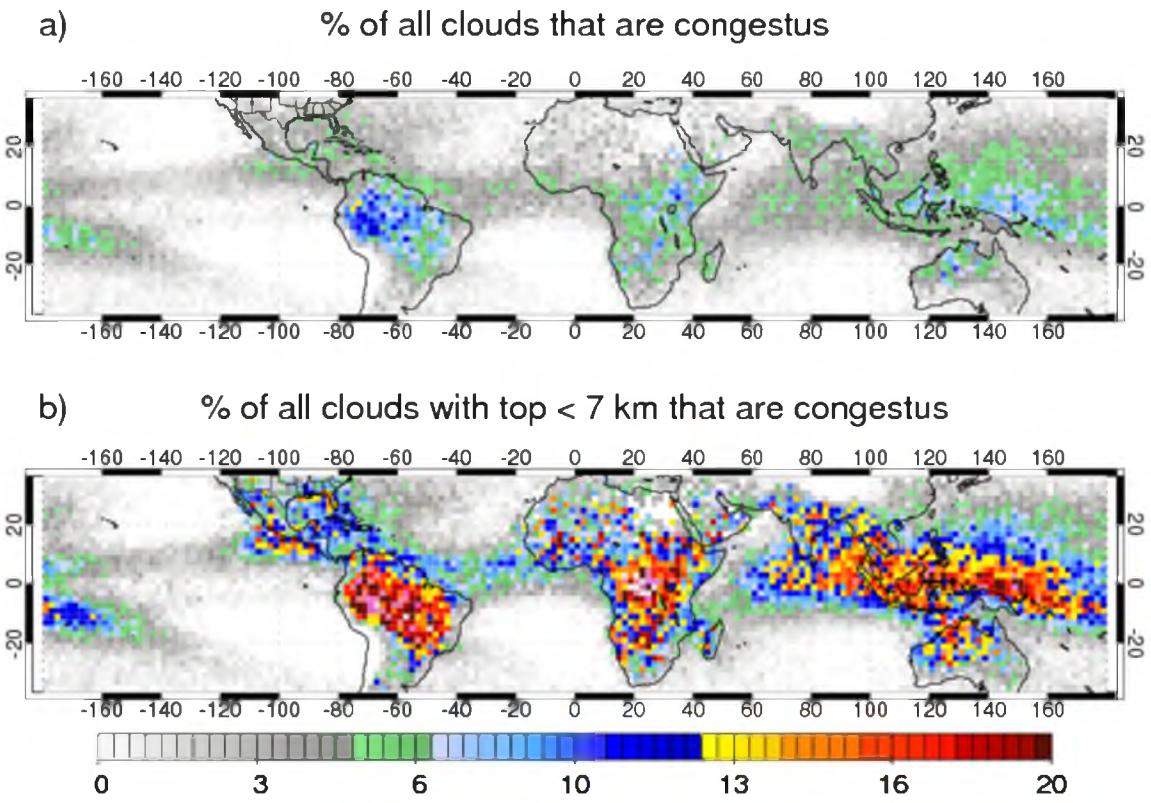

Figure 32: Figures showing the percent (indicated by color) of (a) all clouds observed by CloudSat that are congestus and (b) all clouds with tops less than 7 km observed by CloudSat that are congestus.

with tops less than 7 km that are congestus. The maximum over the Amazon is immediately apparent. In this region, a greater percent of the cloud population is made up of congestus, and these congestus make up 14.5% of low clouds. Central Africa and the Maritime Continent also have a higher proportion of congestus. Over the ocean ITCZ areas, generally 1-5% of all clouds are congestus.

Figure 33 shows the contribution of congestus clouds to global cloud area and amount of rain. Panel (a) shows the ratio of the total coverage (along-track width) of congestus to the total coverage (width) of clouds with maximum tops above 12 km. Areas with a small sample size of congestus are not shown. It is important to note that CloudSat only sees a swath through the cloud, so if the cloud was elliptically shaped and the satellite passed across the minor axis, the width may not reflect the true size of the cloud. In most cases, tall clouds should have a larger horizontal extent than the shorter congestus, which are restricted to smaller sizes by definition. Generally areas dominated by warm rainfall (Schumacher and Houze 2003, Liu and Zipser, 2009) and regions with large-scale subsidence, such as over the southeast Pacific and south Atlantic oceans have a larger ratio of congestus to deeper convection. Of areas with sizable populations of congestus, the Amazon region has a greater ratio of congestus to taller convection. Table 2 lists the values for each region specifically.

To evaluate the rainfall contribution from congestus, rainfall in each TRMM VIRS cloud features is determined from TRMM precipitation radar reflectivity (Iguchi et al. 2000). The fraction of near-surface rainfall from TRMM VIRS congestus is calculated and shown in Figure 33b. In general congestus produce a larger percentage of the total rainfall over the oceans. These percentages of rainfall are far lower than those observed

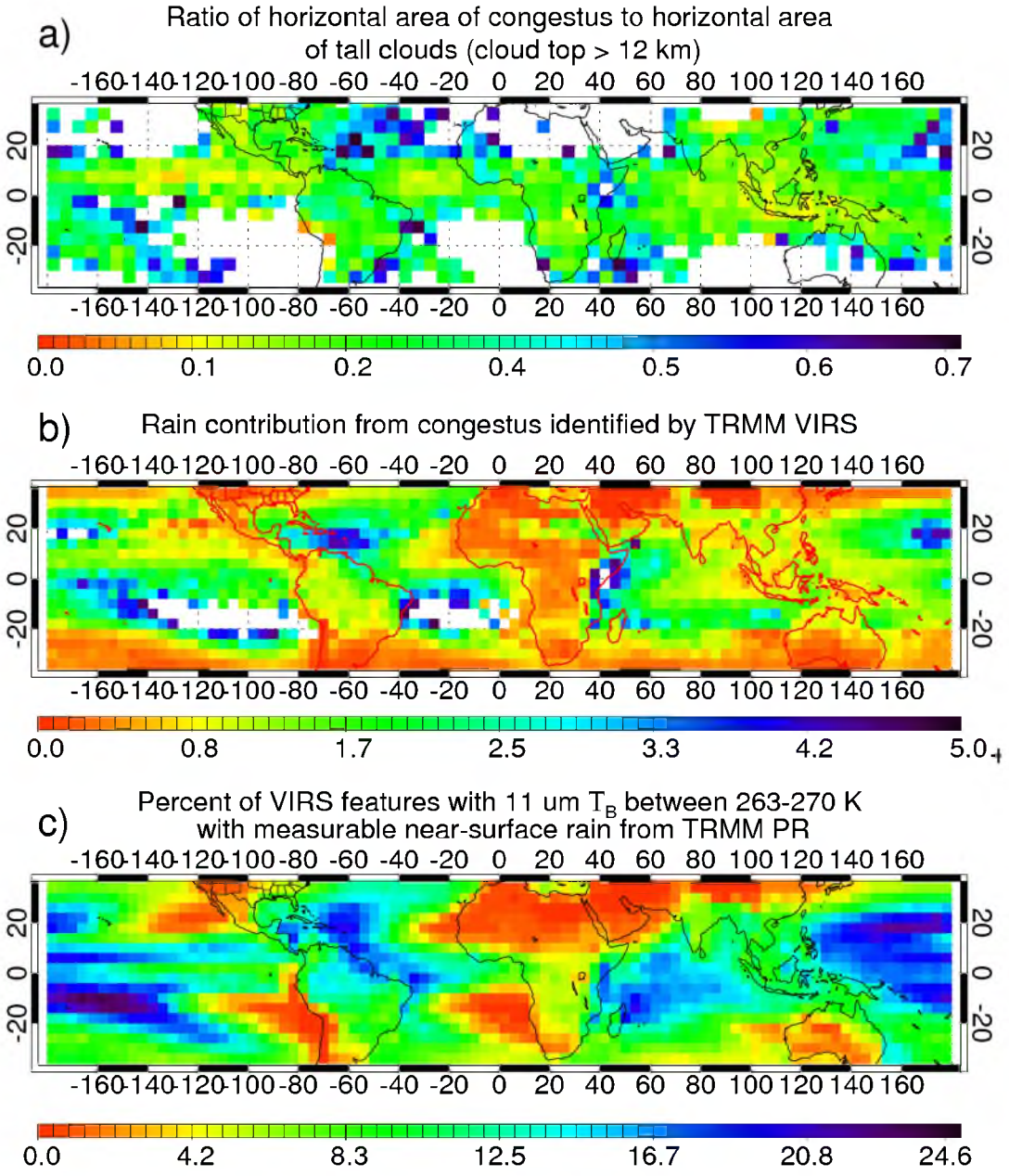

Figure 33: Contributions of congestus to (a) tall cloud (cloud top higher than 12 km) area from CloudSat, (b) rain contribution from congestus identified using TRMM VIRS, and (c) the percent of VIRS features with T_{B11} between 263-270 K with measurable near-surface rainfall from the TRMM PR.

by Johnson et al. [1999] in TOGA COARE, but our precipitation data comes from the TRMM PR, which is known to underestimate weak rainfall due to the radar's sensitivity and 5 km footprint [Berg et al. 2010, Lebsock and L'Ecuyer, 2011]. Therefore, Figure 33b excludes those congestus with very light rainfall rates or small areas. Over land congestus produce a much smaller percentage of total rain, with the exception again being the Amazon region, where values approach those over the ocean. Values for individual regions can be seen in Table 2.

Requiring surface rainfall in our definition of VIRS congestus leaves some congestus clouds out of our sample. Figure 33c shows the percentage of VIRS features with infrared T_{B11} between 263-270 K that have measurable surface rainfall. Ocean areas clearly have a higher fraction of congestus with rainfall while Africa has a much smaller percentage of these cloud features with rainfall. This result is consistent with Casey et al. [2007], which showed that midlevel clouds in Africa are less likely to be raining than midlevel clouds over the Amazon This is a reasonable explanation for the lack of VIRS congestus in Africa and likely results from a combination of higher cloud bases and more inefficient warm rain production. The Amazon region has a considerably higher percent of VIRS features with precipitation.

The Amazon region has the largest percentage of rain produced by congestus, as well as the greatest overall percentage of congestus compared to other types of clouds. Congestus clearly make up a more important part of the spectrum of convective clouds in this region. The West Pacific region and Africa are next in terms of the ratio of the area of congestus to tall clouds, as well as the percent of low clouds that are congestus. The contributions of congestus in these regions are greater than in other regions. Comparing

the East Pacific to West Pacific also yields interesting results. The West Pacific has a considerably greater percentage of all clouds that are congestus, but the mean percentage of rainfall produced by congestus is similar in both regions. This suggests that the East Pacific has a larger population of nonraining or weakly-raining clouds. Indeed, the East Pacific has a smaller percentage of VIRS features with T_{B11} between 263-270 K producing rain (13.3%) than the West Pacific (16.6%).

Seasonal and Diurnal Distributions of Congestus

Figure 34 shows the seasonal distribution of CloudSat congestus. Again, the maximum over the Amazon stands out. This region consistently has many more congestus than anywhere else in the world. The explanation for this is beyond the scope of the current study and will be explored in a subsequent paper. Globally, seasonal changes in the congestus population are more visible over the Amazon region and the West Pacific region. These regions along with Africa tend to have more congestus in the dry season (SON).

Panel (a) of Figure 35 shows the diurnal cycle of VIRS congestus features over the selected regions. The black dashed lines denote the times of the CloudSat overpass. Significant differences are seen in the diurnal cycle of ocean and land congestus. Ocean congestus have a slight peak in occurrence at 0300 local time with very small diurnal change. The diurnal cycle of land congestus has a greater amplitude and peaks near 1330 local time, which coincides with the CloudSat overpass. Notice that the Amazon and Maritime Continent regions peak slightly earlier, near 1245 local time, while Africa peaks later, between 1330 and 1500 local time.

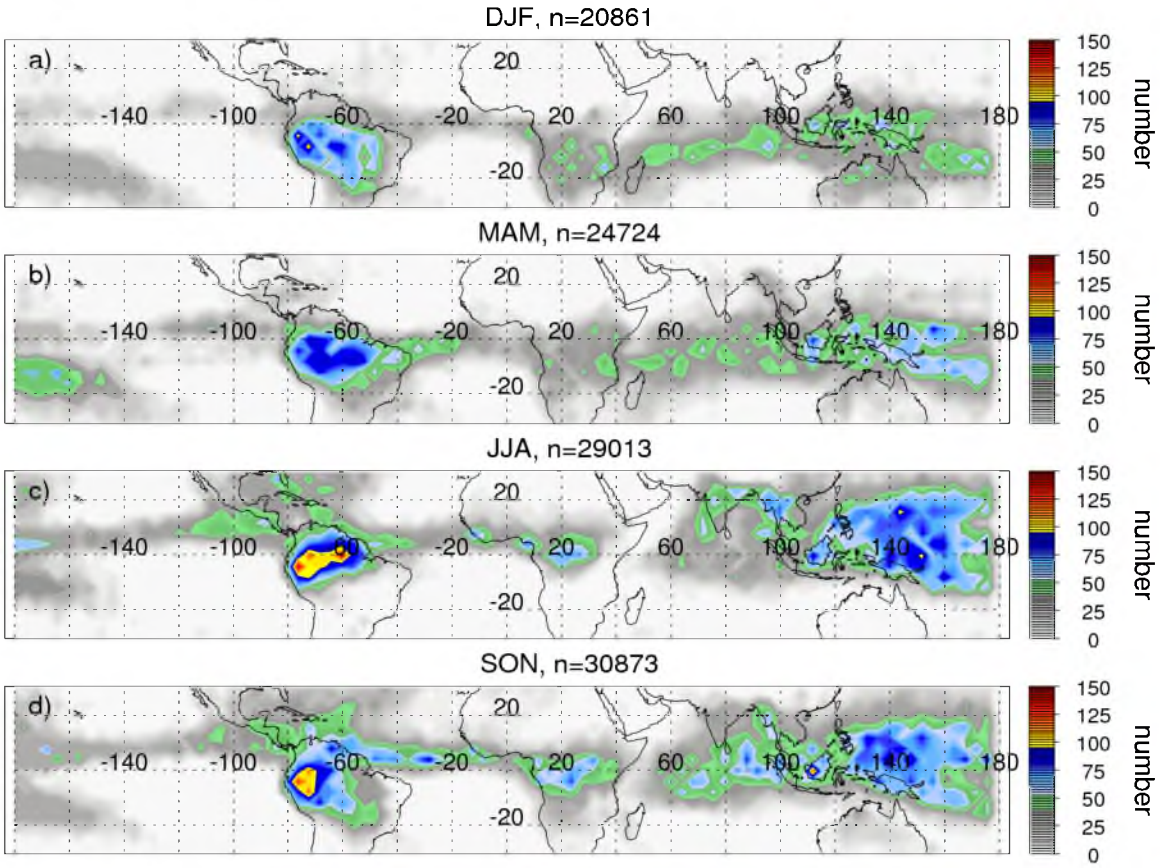

Figure 34: Seasonal cycle of global distribution of population of CloudSat congestus. Colored contours show number of features in (a) December-February, (b) March-May, (c) June-August, and (d) September-November.

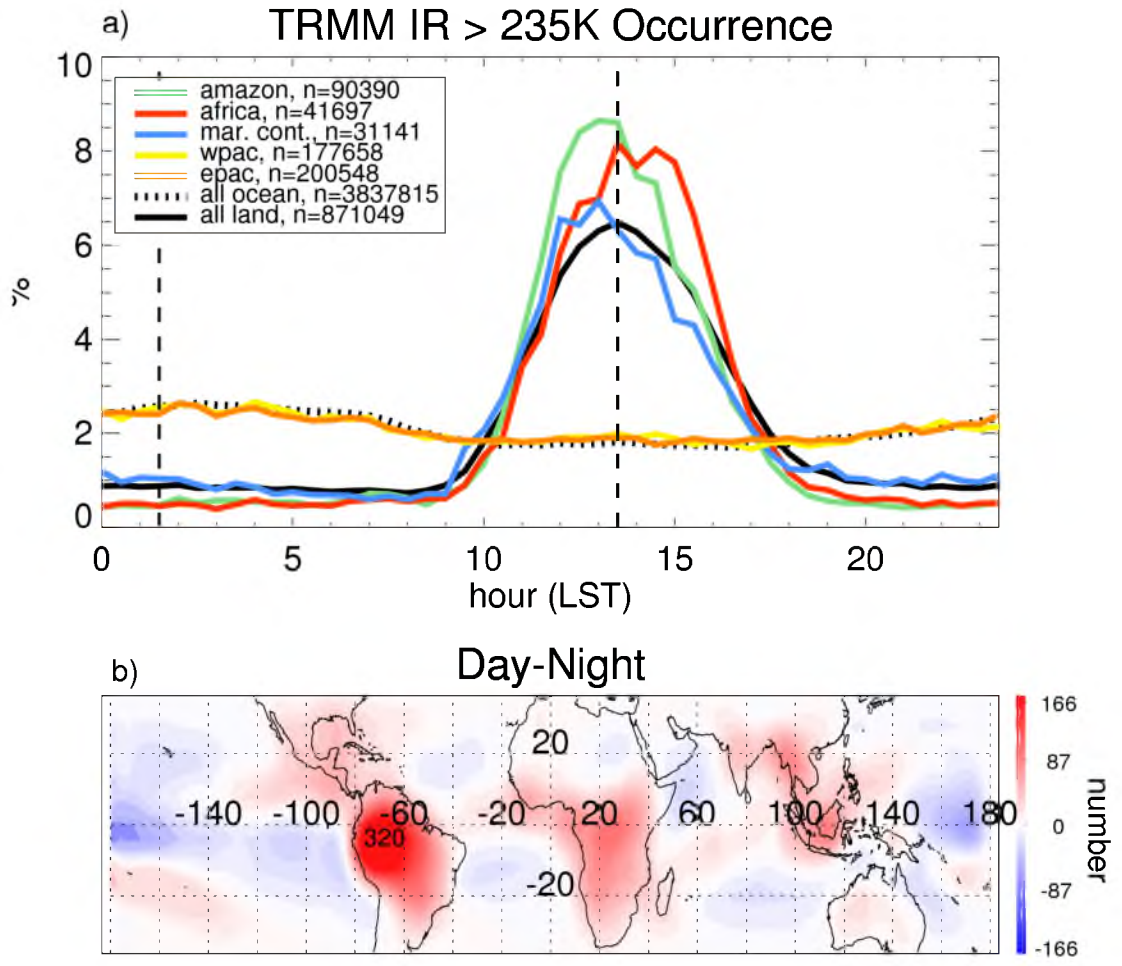

Figure 35: (a) Diurnal variation of population of TRMM VIRS congestus for different regions. The black dashed lines indicate the times of CloudSat overpass. (b) The difference in number of CloudSat congestus from day (1330 LT) to night (0130 LT), contoured in color. Red indicates more daytime congestus, while blue indicates more nighttime congestus. The peak over the Amazon is labeled with the peak occurrence.

The different peaks in diurnal cycle of occurrence match the results seen by Liu and Zipser (2008). In their study, ocean precipitation features from the TRMM precipitation radar (PR) peak between 0200-0300. Likewise, all land features peak between 1400-1500, but the Congo region features a peak in occurrence between 1500-1600. The times of congestus occurrence also match results seen in Liu and Zipser (2009), where rainfall from warm TRMM features peaks shortly after 1200 local time for land and between 0200-0300 local time over ocean.

While CloudSat cannot see the entire diurnal cycle, it captures the afternoon maximum in congestus occurrence. The difference between number of CloudSat congestus occurring during the day (1330 LT) and the number occurring at night (0130 LT) is shown in Figure 35b. Over land more congestus occur during the day. Again, the peak over the Amazon is strong- over twice the number of congestus occur here compared to any other region. Areas to the west of the continents around the ITCZ (west of central America and central Africa) also have more congestus during the afternoon overpass. Many ocean areas have more congestus during the night, but the magnitude of the difference is not as great as that in regions that have more daytime congestus.

Properties of Congestus

Different regions have different seasonal and diurnal cycles of congestus, but are properties of congestus similar for each region? Using CloudSat reflectivity to group features allows the examination of these clouds on an individual basis, rather than sorting each column of pixels individually. Figure 36 compares four different CloudSat congestus properties over selected regions. Panel (a) shows the histogram of maximum

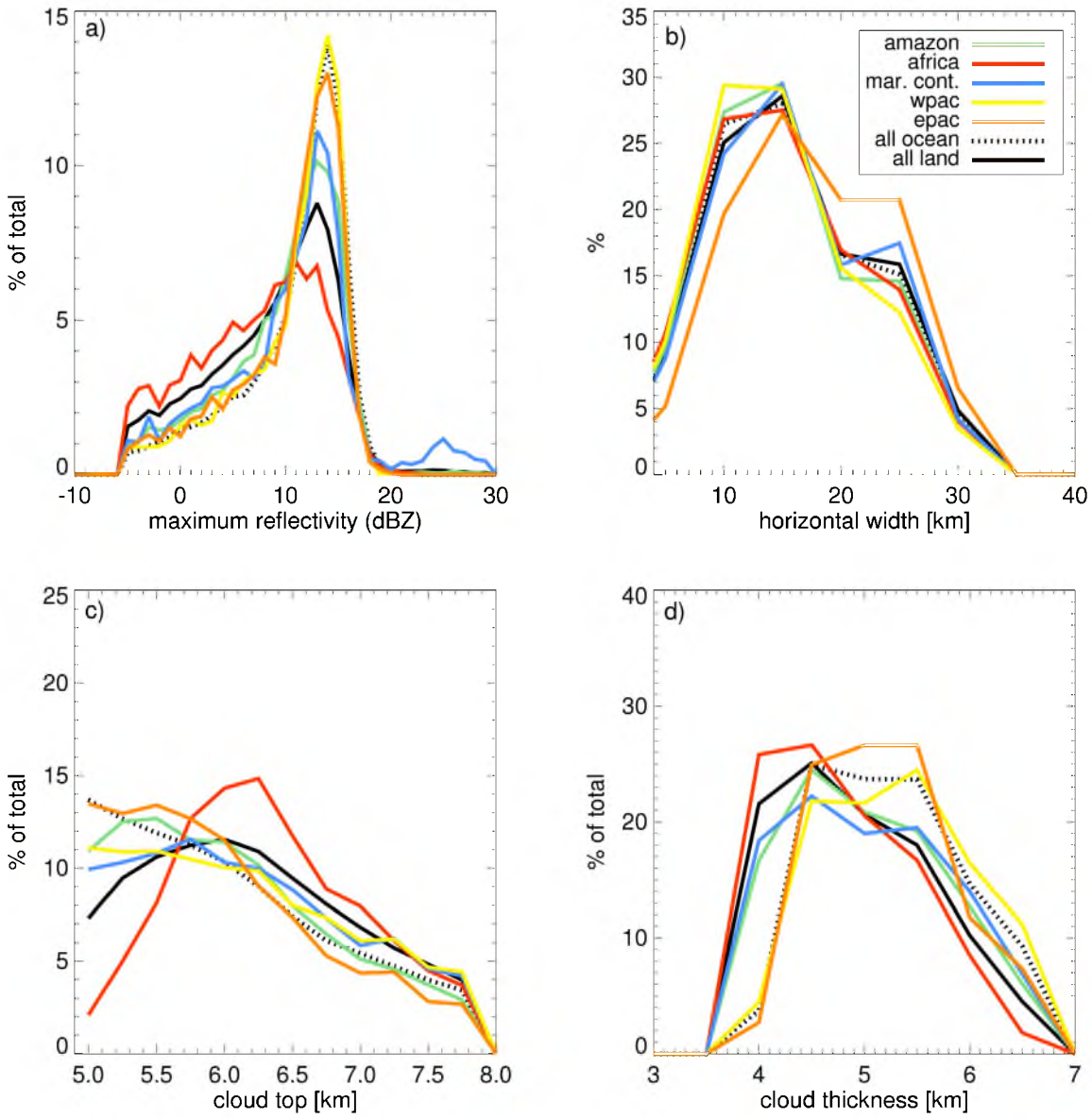

Figure 36: Histograms of (a) maximum reflectivity within a CloudSat congestus, (b) maximum horizontal (along-track) width of CloudSat congestus, (c) CloudSat congestus maximum cloud top, and (d) CloudSat cloud thickness (depth between maximum cloud top and lowest cloud bottom).

Panel (b) shows the histogram of maximum horizontal width of the cloud echo along the CloudSat track (the greatest horizontal extent of the echo at any level). Most regions have a peak in the 10-15 km range and have similar distributions. Slightly more separation is visible between the regions when considering widths of greater than 20 km. The East Pacific has a completely different distribution from any other region. Congestus groups in the East Pacific are larger overall than those occurring in the other regions. The difference in distributions is remarkable. Cifelli et al. (2007) examined two regions in the east Pacific and found that precipitation features in the eastern-most regime had slightly larger mean and median sizes. They also found that features in this eastern Pacific regime were deeper than those in the regime farther to the west, but our CloudSat congestus data do not show significant difference in the distributions of cloud tops between the East Pacific and other oceanic regions (panel c).

The distribution of cloud top heights is similarly shaped for many of the regions. Africa and the all land category are differently shaped, with the peak in the distribution at higher cloud tops. Africa has a peak at 6.25 km. Other land regions have discernible peaks, with the Amazon peaking near 5.5 km, the Maritime Continent near 5.75 km, and all land peaking near 6.0 km. Ocean regions have a slightly different shape to the distribution, with the maximum in occurrence at or just above 5.0 km and decreasing from there. This maximum is not necessarily representative of the population of ocean congestus because tops are required to reach 5 km, but ocean congestus tops in general are lower than land congestus tops. The Amazon region is a land region, but has a peak around 0.5 km lower than mean land and nearly 1 km lower than Africa. This supports the results of Liu and Zipser (2009), who found that mean storm heights over the Amazon

were around 1 km lower than other regions, and is consistent with the idea of the Amazon as a "green ocean" (Silva Dias et al. 2002). It should be clarified that true cloud top is certainly higher than that observed by the CloudSat radar- in this study cloud top refers to the -28 dBZ echo top detected by the CPR.

Cloud thickness is shown in Panel (d) of Figure 36. Cloud thickness is a function of both cloud base and cloud top. Cloud base is the lowest level of hydrometeors detected by CloudSat. The CPR does not differentiate between cloud and precipitation, so separating cloud base from precipitation is somewhat problematic. If a cloud is raining, cloud base will be the lowest detectable signal. Land regions have higher mean echo bases (not shown), which when paired with the restrictions on cloud top height forces land congestus to be vertically thinner than ocean congestus. Africa has the lowest peak in occurrence of cloud thickness, with a peak between 4.0 and 4.25 km. These lower cloud thicknesses could be caused by rain evaporating in drier air in the sub cloud layer. Mean land, Amazon, and the Maritime Continent are close behind, with peaks in thickness of around 4.5 km. The ocean regions (all ocean, EPAC, WPAC) have thicker clouds, with their peaks occurring between 4.5 and 5.5 km. Ocean regions could be producing more congestus with rain.

Width of Congestus

While the population of CloudSat congestus shows only small variations in the maximum horizontal extent of the cloud, surprising differences show up in the width of the clouds at different levels. Figure 37a shows median profiles of the horizontal (along-

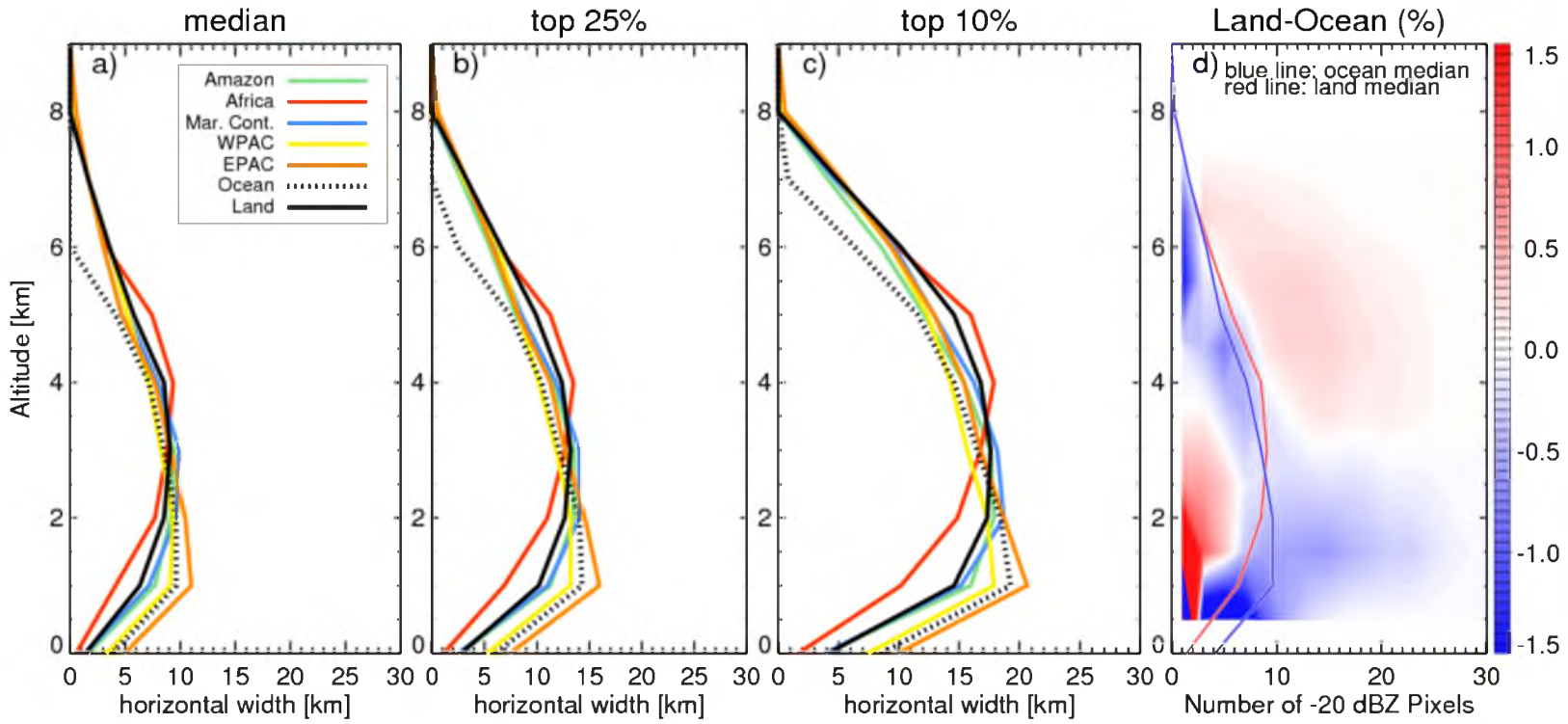

Figure 37: Profiles of (a) median, (b) top 25%, and (c) top 10% of horizontal (along-track) width of CloudSat congestus for different regions. Width is determined using -20 dBZ reflectivity level. Panel (d) shows the difference in occurrence of land and ocean congestus at different altitudes. The median lines for land and ocean are red and blue, respectively.

track) width of congestus at different levels, as defined using the -20 dBZ reflectivity level. The differences between the mean widths of land and ocean congestus are statistically significant at the 99% level at each vertical level. The East Pacific region again has wider congestus groups than any other region, but only below the freezing level (4.75 km in the Tropics). One explanation for this could be that the East Pacific region has more individual congestus towers that are grouped together and appear connected with CloudSat. At around 3 km, a reversal occurs in the width of land and ocean congestus groups. Below this level, the ocean regions have bigger features. Above this level, land congestus are larger. This reversal is featured most prominently in the top 25% and 10% (Figure 37b and 37c), where the largest land features have a much different shape than the largest ocean features. The difference in the percent occurrence of these profiles is shown in Figure 37d, in which it can be seen that groups of land congestus are generally smaller than groups of ocean congestus below 3-3.5 km, while ocean congestus groups are generally smaller than land congestus above this level.

Global differences in the mean widths of congestus are shown in Figure 38. The top panel shows mean cloud width at 5 km, and the bottom panel shows mean cloud width at 2 km. At 5 km features over land have larger mean widths, particularly in Africa. Ocean features at 5 km tend to have mean widths of 5-10 km, while some of the land widths reach nearly 20 km. At an altitude of 2 km, ocean features are clearly larger than land features in many areas, with ocean congestus reaching mean widths of 20 km, while the mean width over Africa is around 12 km. These results point to groups of congestus over land and ocean having very different shapes. This idea will be discussed further in the discussion and conclusions of this chapter.

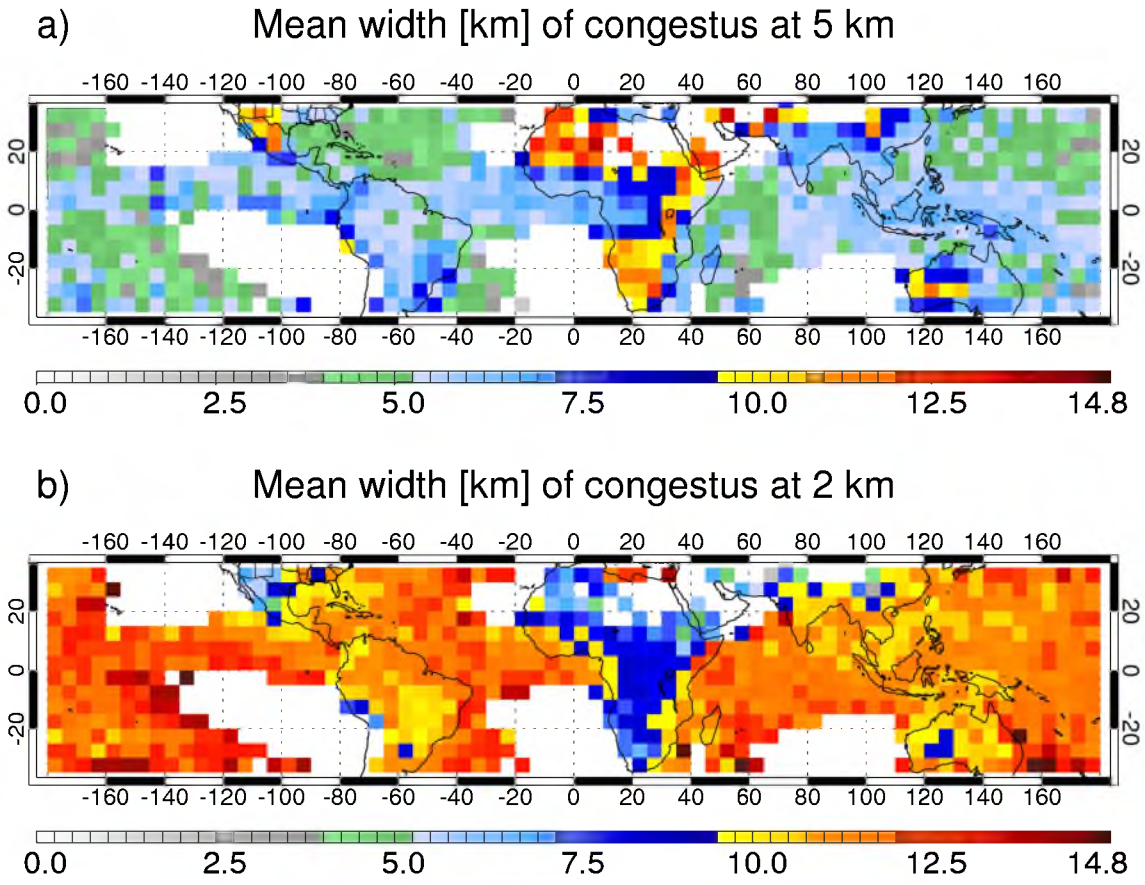

Figure 38: Mean width (defined using the -20 dBZ reflectivity level) at (a) 5 km and (b) 2 km in altitude for CloudSat congestus. Colors indicate mean width in km.

Profiles of Congestus Reflectivity

The differences in cloud width with height inspire questions as to whether trends can be seen in maximum reflectivity. Profiles of maximum reflectivity with height can be seen in Figure 39. The distributions of maximum reflectivity of land and ocean congestus have statistically different means at the 99% level for the entire vertical profile using a T-test. The ocean regions clearly have larger reflectivities below freezing level. Above this level, changes between land and ocean are difficult to discern. Differences between the regions are also greatest for the median maximum reflectivity- once only the top 10% are considered, differences between the regions are smaller. If a congestus cloud was growing vertically, we would expect higher reflectivities closer to cloud top. The top of the profile for the top 10% of maximum reflectivity may reflect the higher reflectivities seen in these growing congestus. Panel (d) shows the differences in contoured frequency by altitude figures for land and ocean. Ocean congestus clearly have a greater occurrence of higher maximum reflectivities. The shapes of these reflectivity profiles and their implications will be discussed further in the next chapter.

Discussion of Congestus

Congestus occur most frequently in the Tropics, with some regions experiencing a larger number of these clouds than others. Some differences in congestus properties, including area, reflectivity profile, and levels of cloud top and echo bottom are seen between these regions, but the greatest differences between these regions can be attributed to disparities between groups of land and ocean congestus.

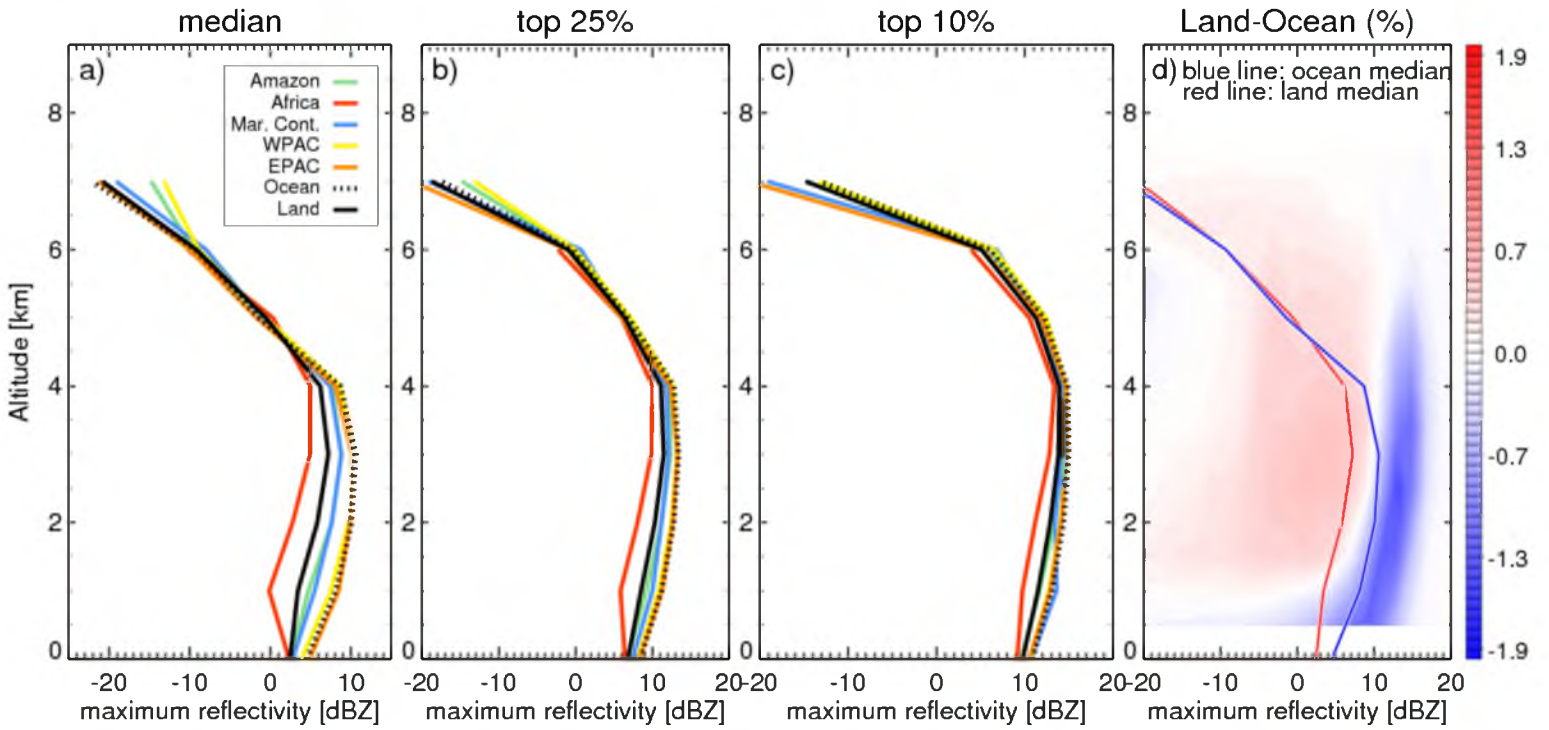

Figure 39: Profiles of (a) median, (b) top 25%, and (c) top 10% of maximum reflectivity for CloudSat congestus in different regions. Panel (d) shows the difference in contoured frequency between land and ocean profiles of maximum reflectivity. The land and ocean median lines are red and blue, respectively.

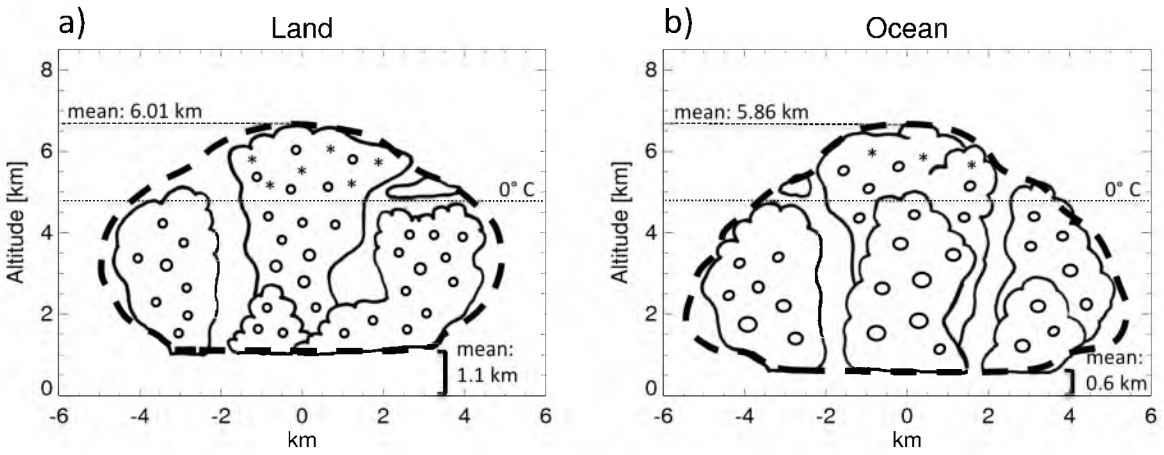

Figure 40: Theoretical schematic of (a) land and (b) ocean congestus, created from the mean width of CloudSat congestus over land and ocean at each altitude level. The mean cloud top height and cloud base height are indicated. The dashed line indicates the "cloud envelope" observed by CloudSat, while the congestus within this line are artistically sketched to show what the congestus might look like. The placements of hydrometeors are speculative.

Figure 40 summarizes the properties of land and ocean congestus. This cartoon can be compared with the land and ocean congestus examples shown in Figure 30, panels (a) and (b). The shapes of these cartoon clouds were derived from the mean width of land and ocean congestus at each level (similar to Figure 37a), not accounting for tilt of the cloud, and the mean tops and bottoms are indicated. These mean values of cloud base agree with the results of Hahn et al. (2001), who found mean values for land and ocean congestus and cumulonimbus using surface observations. Land and ocean congestus have nearly the same mean width. Again, the widths of the "congestus" observed by CloudSat are too wide to be individual cumulus congestus clouds. Rather, the shapes identified

using the mean widths can be thought of as "cloud envelopes", in which individual congestus towers are spaced too closely to be separated with the 1.1 km footprint of CloudSat. Figure 40 shows individual congestus clouds within this cloud envelope.

Differences occur in cloud shape, with land congestus being "muffin-shaped" while ocean congestus are more "bell-shaped". Land congestus also have higher bases and slightly higher tops overall than ocean congestus. Figure 7 in Liu and Zipser (2009) shows cumulative distribution frequencies of warm PFs defined using the TRMM over land and ocean in the tropics. In their figure, land features are smaller than ocean features. Area in this case is defined by raining area, so their results match the differences we have observed with congestus- land congestus are smaller than ocean congestus below the freezing level.

The locations and sizes of hydrometeors in this cartoon are purely speculative. Using only CloudSat we have no definitive proof of quantities or sizes of water and ice particles, although higher reflectivities in oceanic congestus point to larger hydrometeors in those clouds. The slightly higher cloud tops of land congestus and the larger area suggest that perhaps there could be more ice hydrometeors in the top of land congestus. Perhaps cloud probe data from flights in past field programs could shed more light on the distribution of hydrometeors within congestus clouds over land and ocean. The proper representation of the microphysics of these clouds, including differences between land and ocean congestus, is very important. Microphysics determine the amount of precipitation falling from the cloud and the amount of moisture that remains to moisten the environment (Emanuel 1997).

Entrainment and detrainment rates within these congestus are both functions of the vertical gradients of buoyancy within the cloud (Bretheron and Smolarkiewicz 1989). The release of latent heat above freezing level in convective clouds adds to the positive buoyancy of the cloud and increases the level at which outflow occurs at cloud top. Mixing occurs at all levels within the cloud, and buoyancy sorting within the cloud contributes to the vertical mass flux (Raymond and Blyth 1986). Maximum outflow from the cloud should occur at the height at which buoyancy is decreasing most rapidly with height (Bretherton and Smolarkiewicz 1989). Perhaps the differences in shapes of land and ocean congestus are caused by different buoyancy profiles. In land congestus, larger CCN concentrations lead to a larger number of smaller cloud drops and less collision and coalescence. These smaller droplets are then lofted above the freezing level where the release of latent heat adds to the positive buoyancy at that level, causing the outflow of the congestus to occur at a higher height and spreading condensate at a higher level than that of ocean congestus, leading to a different shape.

It is well known that important distinctions exist between deep convective clouds over land and over the ocean. Differences in heating profiles, updraft speeds, and number of cloud condensation nuclei (CCN) are all thought to play a role. The shape and magnitude of the profile of latent heating depends on the height of the clouds and the amount of cloud material detrained (Schumacher et al. 2007), so understanding the difference in shapes of congestus over land and ocean is important to properly represent these profiles.

Oceanic clouds generally occur in cleaner air (Squires 1956, Twomey and Wojciechowski 1969), and fewer CCN could result in more efficient warm rain process

and lead to larger raindrops. This is consistent with higher reflectivity in oceanic congestus at low levels. Less latent heat release and a weaker updraft above freezing level in ocean congestus would lead to fewer ice particles. The higher cloud base observed over land, especially over Africa, could be playing a role in weaker warm rain processes and higher cloud tops. Lower mean cloud bases for ocean congestus also indicate that they produce more rain than land congestus. This can be seen with the VIRS congestus (Figure 33).

Deep convective clouds over land have higher updraft speeds (Zipser and LeMone 1980), which could force more condensate above the freezing level. If enough condensate is lofted above 0°C, the release of latent heat could cause additional lift and higher cloud tops (Zipser et al. 2003). There is no way of knowing whether our congestus have reached their maximum height or will continue to grow in this manner.

This study does not investigate how many of these convective clouds over land and ocean continue to grow into larger, deeper cloud systems. Luo et al. (2009) found that 42% of their congestus over ocean and 36% of congestus over tropical land were transient, and likely to continue to grow. The presence of dry, warm air near the freezing level has been thought to control the amount of congestus that continue to grow into deeper convection (Malkus and Riehl 1964, Johnson et al. 1999, Redelsperger et al. 2002). Many of these ideas regarding land/ocean differences are purely speculative- we have not shown that these principles, most of which have been developed by studying deep convection, can be applied to congestus, but some of these processes could explain the differences between land and ocean congestus. A preliminary look at relative humidity profiles associated with our congestus showed that its effect on cloud

parameters such as top and area is more complicated than the presence of a dry layer and varies from region to region, so the explanation for congestus occurrence relative to environmental parameters is left for another study.

Interactions between congestus and the environment will be critical to the study of the MJO. Waite and Khouide (2010) find that detrainment from congestus clouds can moisten the lower troposphere, while Kemball-Cook and Weare (2001) show that the periodicity of the MJO may be controlled by the build up and discharge of moist static energy in the lower atmosphere. The MJO is typically preceded by low-level convergence and moistening at low levels, followed by the development of shallow convection, and a gradual lofting of moisture by congestus (Kiladis et al. 2005). The extent to which congestus precondition the environment for deeper clouds must be investigated.

The next steps in the study of CloudSat congestus are to determine which clouds occur on days when congestus grow into deeper convective clouds and examine the environments in which this does and does not occur, with the goal of exploring the mechanisms by which these congestus are restricted to lower levels or allowed to grow into deeper clouds.

Congestus Conclusions

Congestus cloud clusters are an important part of the tropical climate. Despite its sun-synchronous orbit, CloudSat is a viable tool for examining global congestus, as it is able to resolve both clouds and precipitation. Comparisons with TRMM show that it captures the afternoon maxima in congestus occurrence. CloudSat shows that congestus

are found most frequently in the Tropics, particularly along the ITCZ and make up anywhere from 0-12% of clouds. In places in South America, central Africa, and the Maritime Continent, congestus make up 18% of the population of low clouds. A significant maximum in the occurrence of congestus is observed in the Amazon.

Important differences are observed in properties of congestus cloud groups in different parts of the world. Most of the regional differences in congestus can, at first glance, be attributed to differences in congestus over land and ocean. Oceanic congestus tend to have higher maximum reflectivities, lower bases, and lower cloud tops than land congestus. Groups of congestus over the East Pacific region are larger than congestus clusters in other (land or ocean) parts of the world. Africa has the largest number of higher congestus tops.

Profiles of congestus width show that clusters of land and ocean congestus have different shapes. Ocean congestus groups are more bell-shaped, with wider bases and sides that slant towards a skinny top. Land congestus groups are more muffin-shaped, with sides that slope more slowly to a wider top. Many congestus over land are wider above the freezing level than near the ground. Panel (a) of Figure 30 shows an example of a land congestus with a very wide top. The differences in the shapes of these clouds are robust and are clearly seen within the means of land and ocean congestus. The difference in means is statistically significant. Differences in shapes of congestus would be well related to different latent heating profiles and possibly differences in precipitation and radiation balances between congestus over land and ocean. These previously un observed differences have large implications in the numerical modeling world, where the correct parameterization of tropical convection is critical in global climate models.

How do these congestus fit into the diurnal and seasonal cycles of convection? More work is needed to determine the full impact of these clouds on precipitation, cloud cover, and radiation balances in the Tropics. The mean environments of land and ocean congestus, including the presence of stable layers near the freezing level as well as mid-tropospheric moisture need to be examined to see if either of these parameters can explain the population of global congestus. Further work on these topics is warranted in the future.

CHAPTER 5

CONGESTUS AND AEROSOLS

Congestus clouds are smaller than their deep convective counterparts, which were discussed using TRMM in Chapter 3. Congestus probably do not influence their environment as much as deeper, larger convective features and their smaller size may allow detection of the very small signal of the aerosol indirect effect. Aerosols are known to affect warm clouds. The extent of aerosol influences on clouds with some ice is uncertain, at least from an observational perspective. The congestus defined and studied in Chapter 4 have tops reaching above 4.5 km, which is the typical freezing level in the Tropics, and therefore may have some ice. Sheffield et al. (2013) use a radiative convective equilibrium model to study the effects of aerosols on congestus and places a cloud top height restriction of 4-7 km on their congestus, matching the population of congestus used here. The results of Rosenfeld and Lensky (1998) show development of a mixed-phase region in their satellite-observed clouds between -5 and -10°C in most cases. Observations from West Pacific convective clouds show that by -10°C, congestus certainly contain ice, but that clouds that only briefly reach -5°C before falling back to lower altitudes continue to be composed of water (Rangno and Hobbs 2005). Thus this population of congestus, paired with MODIS AI, can be used to evaluate the influences

of aerosol on clouds with tops high enough to contain some ice, although the amount of ice is uncertain.

Regional Impacts of Aerosols on Congestus

From the results using TRMM, it is clear that the properties of convective clouds are influenced by location and seasonality. Seifert and Beheng (2006) and Stevens and Feingold (2009) postulate that the effects of aerosols are regime-dependent. Van den Heever et al. (2011) show that responses to aerosol forcing are cloud regime-dependent. For this reason, comparisons between clean and dirty congestus will only be made for three specific regions of the world, which can be seen in Figure 41. These regions were selected because they have a reasonably sized population of both clean and dirty congestus cases. Some comparisons for clean and dirty cases from all ocean congestus will be shown, but concerns about local environmental influences on congestus properties require that specific regions are selected. All congestus within these regions are considered, and then upper and lower quartiles of MODIS AI are used to define clean and dirty.

The Amazon and Africa regions are identical to the regions used in Chapter 4 and similar to the regions used in the TRMM analysis of deeper convective clouds. These regions showed the biggest differences between dirty and clean TRMM RPFs and are assumed to have the same type of aerosols, released from biomass burning in the September-November months. Additionally the West Pacific (WPAC) will be used to show the impacts of additional CCN on the shape of congestus. This region is influenced

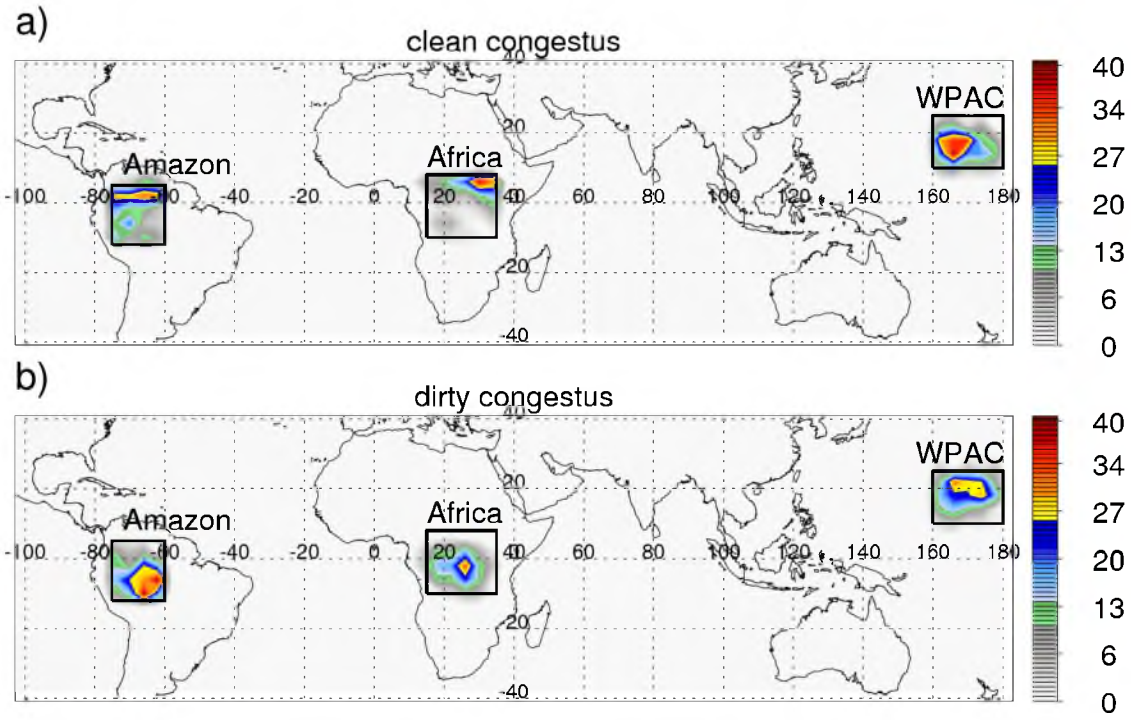

Figure 41: Plots showing the locations of (a) clean and (b) dirty congestus in the regions of interest for the study. Clean and dirty are defined by the upper and lower quartiles of AI.

by a variety of aerosols, including Asian dust and pollution in the form of sulfates (Chin et al. 2007). Note that this location is slightly to the east of the region used to study congestus properties in Chapter 4. This shift was made to select a region with a good sample size of clean and dirty congestus. Histograms of AI for each region are shown in Figure 42. The WPAC region has much lower values of AI because it is an ocean region. The difference in AI for "dirty" congestus in the three regions is highlighted by the median of the upper quartile shown on the figure. The median for the WPAC region is considerably less than that for the Amazon and Africa regions. Again, the lower limit on "dirty" RPFs in the WPAC is so low that some of these RPFs would be considered clean in land regions. These differences make it difficult to compare the effects of aerosols on land and ocean regions. Over the WPAC, truly dirty background aerosol concentrations are difficult to find.

One of the potential issues with using MODIS to define a background AI for TRMM features is that MODIS can only determine AI during the day, which is the 1330 local standard time (LST) overpass, and the differences in orbits between MODIS and TRMM could result in a lag between the occurrence of the RPF and the time of the MODIS AOD measurement. CloudSat does not have this problem for daytime congestus, because CloudSat and MODIS are on the same orbit. Table 3 shows the percent of CloudSat congestus in the three regions of interest that are observed during the 1330 LST overpass.

The land regions (Amazon and Africa) have a greater number of congestus occurring around 1330 LST than the WPAC. The WPAC region has more congestus around 0130 LST than the land regions. Amazon and Africa have better

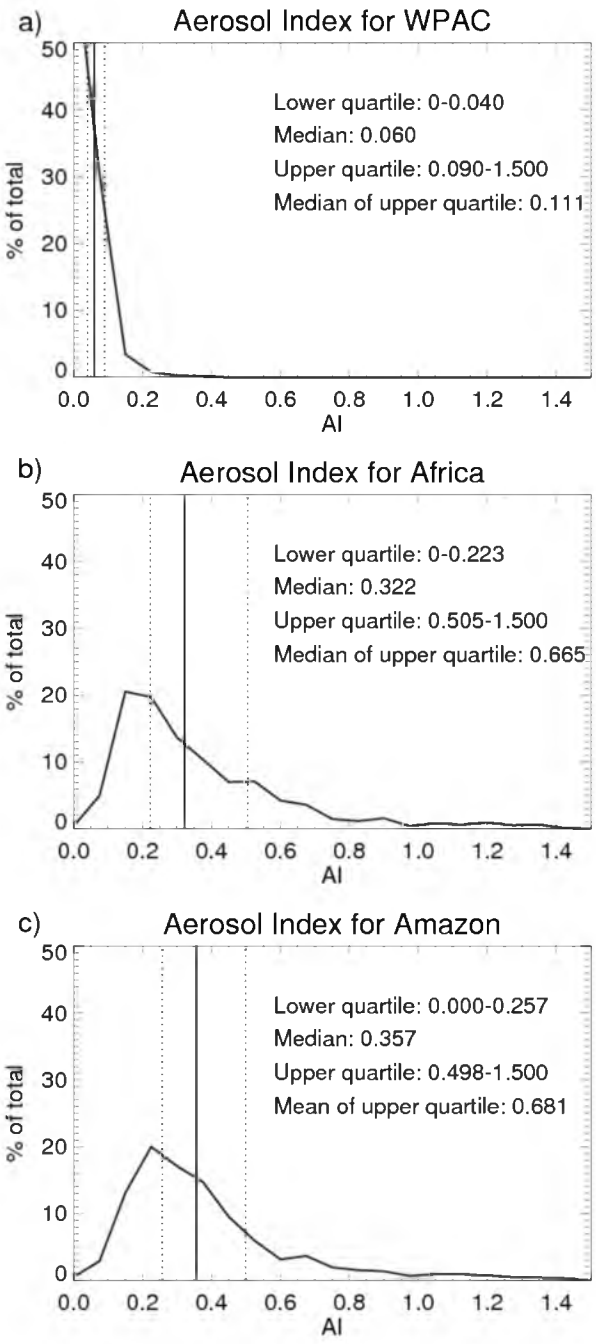

Figure 42: Histograms of AI for a) the West Pacific, b) Africa, and c) Amazon regions. The median value is indicated by the solid black line, and the dashed lines are the quartile limits. The upper and lower quartiles are used to define clean and dirty congestus.

Table 3: Population of congestus in each region observed during 1330 LST overpasses (day) and 0130 LST overpasses (night).

		% 1330 LST	% 0130 LST	Total Number
WPAC	Clean	32.7	67.3	429
	Dirty	22.8	77.2	
Amazon	Clean	85.0	15.0	590
	Dirty	94.6	5.4	
Africa	Clean	77.5	22.5	472
	Dirty	80.9	19.1	

temporal matches between congestus and the background aerosol content. The three regions have similar populations of congestus as well

Are there differences in the properties of congestus occurring in clean and dirty environments? Figure 43 shows histograms of a few properties of the clouds. Panel (a) shows maximum reflectivity. The Africa region has differences between clean and dirty congestus, but they are not systematic. The Amazon region shows a displacement of the peak occurrence- clean congestus have a peak at higher reflectivity. The WPAC region shows only slight differences between clean and dirty congestus but has a much more pronounced peak at around 12 dBZ- slightly higher than the peak reflectivity in Amazon or Africa.

Figure 43b shows histograms of cloud width. The Africa and Amazon regions have slightly different peaks in the histogram- Africa shows dirty congestus having a peak at a greater width. The Amazon region has clean and dirty congestus peaking at the same width, but slightly more dirty congestus have narrower widths. Again the WPAC shows only slight differences between the clean and dirty regimes.

The histograms of cloud top height (Figure 43c) are more interesting. In Africa, the peak in cloud top height for dirty congestus is 0.25 km higher than that for clean congestus, but the distribution of cloud tops for dirty congestus is more spread out, while the distribution of tops for clean congestus has a more pronounced peak. Again, the WPAC region shows only slightly differences between clean and dirty congestus, but this region has a very different shape from the land regions. Congestus tops tend to be lower, in the 5.0-5.5 km range. Fewer congestus reach 6.5 km, which is the altitude at which

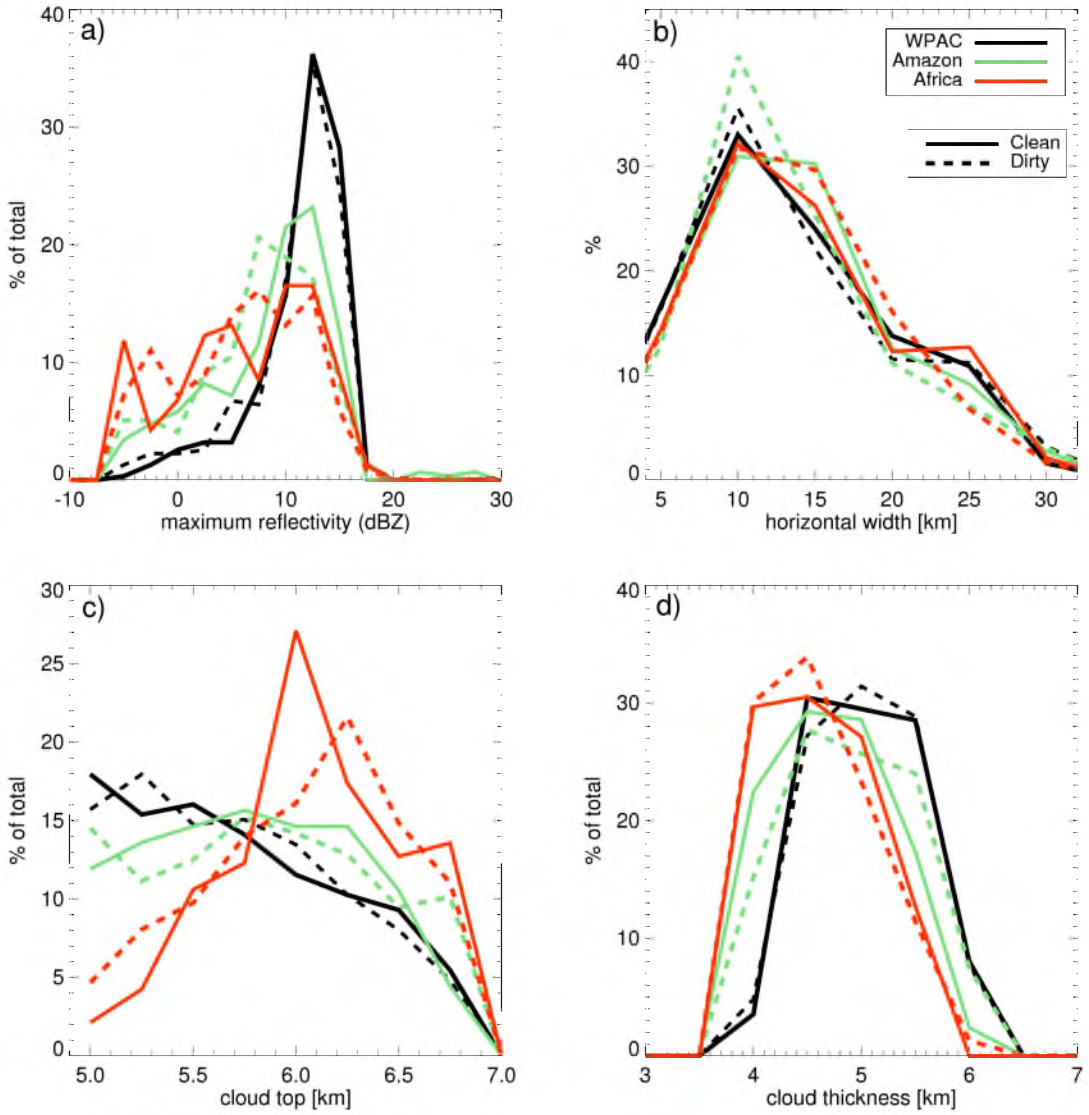

Figure 43: Histograms of a) maximum reflectivity, b) horizontal width, c) cloud top, and d) cloud thickness between clean (solid) and dirty (dashed) congestus in the Amazon (green), Africa (red), and WPAC (black) regions.

Blyth et al. (1997) first detected ice when flying through a cumulus congestus in New Mexico. The WPAC region therefore likely has more congestus without ice or with smaller quantities of ice, based on height of cloud top alone.

Sheffield et al. (2013) found that increasing aerosol concentration in their model more than doubled the number of congestus that reached above the freezing level. A larger number of CCN causes a greater number of small droplets, greater integrated droplet surface area, more effective supersaturation usage, and greater latent heating when compared to cleaner clouds. This allows congestus to grow above the freezing level. Because congestus tops are required to be above freezing in this study, we cannot observe this, but once congestus tops are above freezing, we see no invigoration for these cases.

Cloud thickness is shown in Figure 43d. Thickness is the value of cloud top minus echo base. Again, the CPR on CloudSat does not differentiate between cloud droplets and precipitation, so the term echo base is used to describe the lowest level of cloud/rain echo from the CPR. If a cloud is precipitating, rain is included as part of the cloud, and therefore the echo base will be lower. Unfortunately most methods for determining surface precipitation rely on using path integrated attenuation (as in Ellis et al. 2009), and the data in the CloudSat Database provides no method for determining the microphysical properties of congestus, although we can make some assumptions, which will be discussed shortly.

The Africa region shows only slight differences in thickness between clean and dirty congestus, while the distribution in the Amazon shows that dirty congestus tend to have greater vertical thickness in spite of only small changes in the cloud top height

distribution between clean and dirty congestus. The deepest congestus of all occur in the WPAC region. This result could be caused by a greater amount of rain falling from WPAC congestus. A higher percentage of congestus in this region are shown to produce rain in Figure 33c. Differences between clean and dirty are slight in all of these regions, but the land/ocean values of thickness between WPAC and the Africa/Amazon regions show a significant contrast.

These histograms do not show any striking differences between clean and dirty congestus, aside from some variations in cloud thickness. Two-dimensional histograms of congestus top and echo bottom with increasing AI also show only slight differences. These can be seen in Figures 44 and 45, respectively. As in Figure 43c, the WPAC and Amazon regions do not show any remarkable changes in CloudSat cloud top with increasing AI. The peak in cloud top between 6.0-6.5 km can be seen in the Africa region. Figure 45 shows that not much variation occurs in cloud echo base with increasing AI in Africa or the Amazon. In the WPAC, however, increasing AI leads to higher echo bases. Since a greater percentage of congestus in the WPAC are already producing rain (Figure 33c), perhaps increasing AI acts to suppress the warm rain, leading to higher echo base, if there is insufficient rain for CloudSat to detect. However, if rain is falling there is no way to determine whether the clouds formed in a clean environment or if the rain cleaned the environment. CloudSat detects lower echo bases if rain is falling. Rain tends to scour aerosols. Therefore, if it is raining, the environment is likely to be clean. In the absence of rain (which means CloudSat would detect a higher echo base), aerosol would not be washed out, leading to a higher value of AI. This is just one possible explanation. The lower echo bases could also be surface contamination,

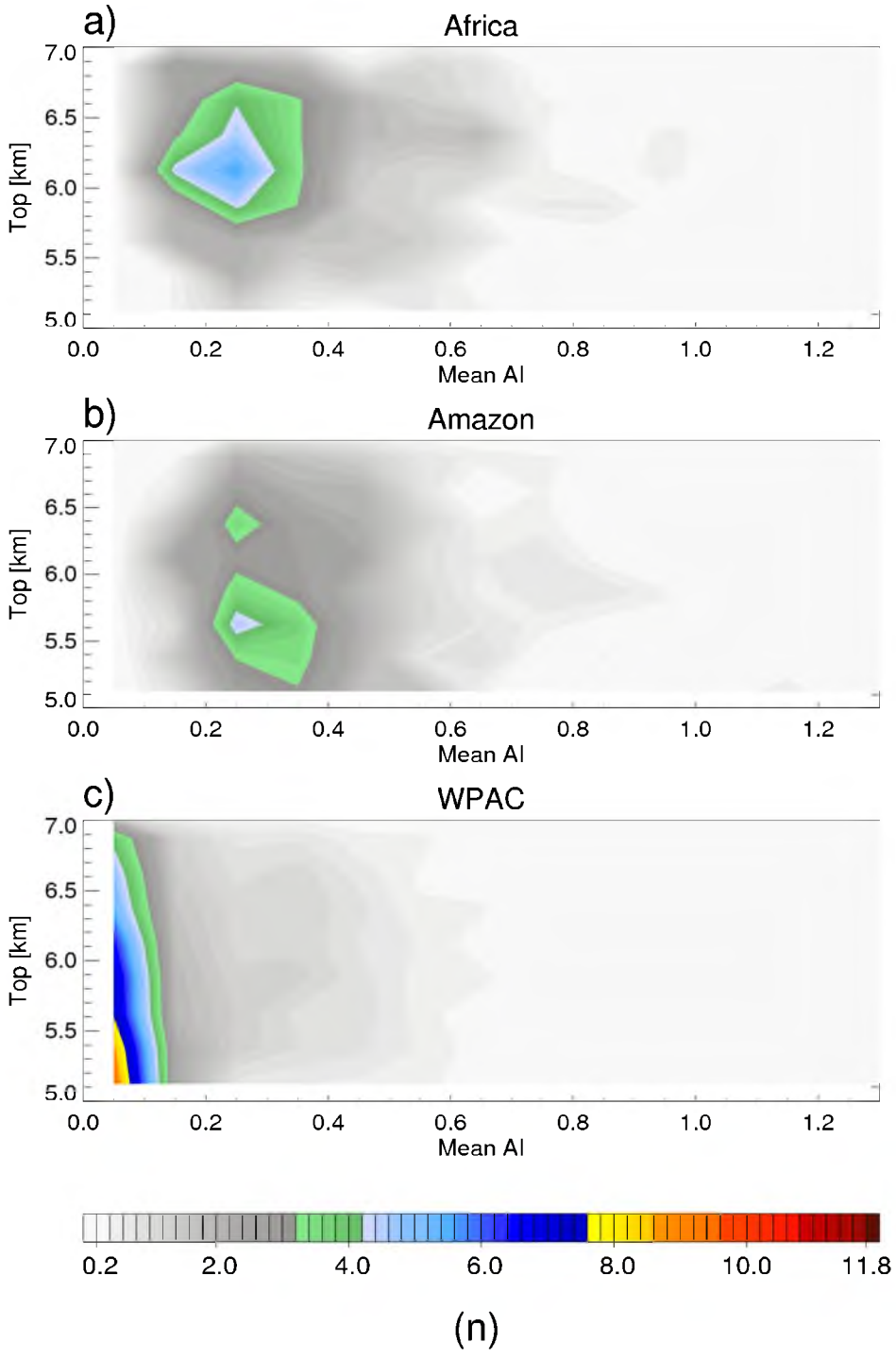

Figure 44: Two-dimensional histograms of cloud top with increasing AI for a) Africa, b) Amazon, and c) WPAC regions. Number is contoured in color.

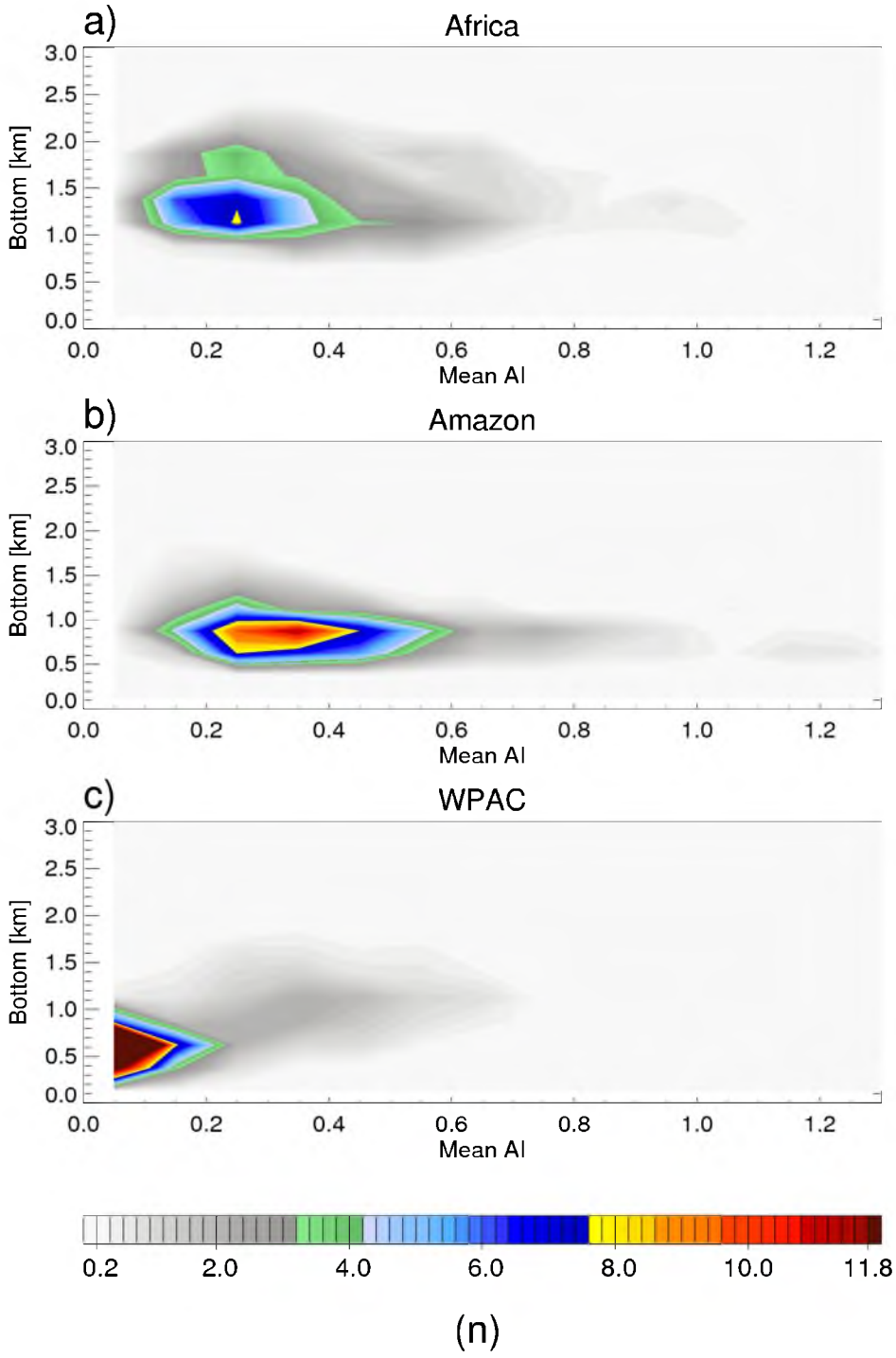

Figure 45: Two-dimensional histograms of cloud base with increasing AI for a) Africa, b) Amazon, and c) WPAC regions. Number is contoured in color.

which can happen below 1 km with CloudSat, although generally precipitation can be detected above noise down to around 0.5 km (Mace et al. 2007).

In Chapter 4 differences in land and ocean congestus were observed. One possible explanation for these differences is the presence of additional CCN in land congestus. Figure 46 shows the changes in cloud width with height. The differences between clean and dirty widths are not statistically significant at any level in Africa, the Amazon, or the WPAC regions. In Africa, dirty clouds are smaller above 4 km and wider below 4 km. The Amazon shows the opposite trend, with dirty congestus being narrower below 4 km and wider above 4 km. The WPAC region shows almost no differences.

Panel (d) shows the difference in occurrence of dirty and clean profiles for all ocean congestus, with the median lines overlaid. The differences in the mean of congestus width for clean and dirty ocean congestus is statistically significant at the 99% level using a T-test at all levels except for 3 km. For all ocean, groups of congestus in dirty environments tend to be wider above 4 km and smaller below this level. This is consistent with the shape of groups of land congestus, which have more CCN. Adding CCN to a group of ocean congestus could make the shape more muffin-like. Again, these congestus are multiple clouds grouped together. Adding CCN to a cloud could suppress warm rain and allow congestus to grow taller and expand as the updrafts detrain in the mid-troposphere, leading to a muffin-shape if multiple clouds are located close together.

One of the most prominent differences between clean and dirty congestus can be seen in reflectivity (Figure 43a). Figure 47 shows profiles of maximum reflectivity with height for all three regions. In all three regions, and for all ocean congestus (shown in

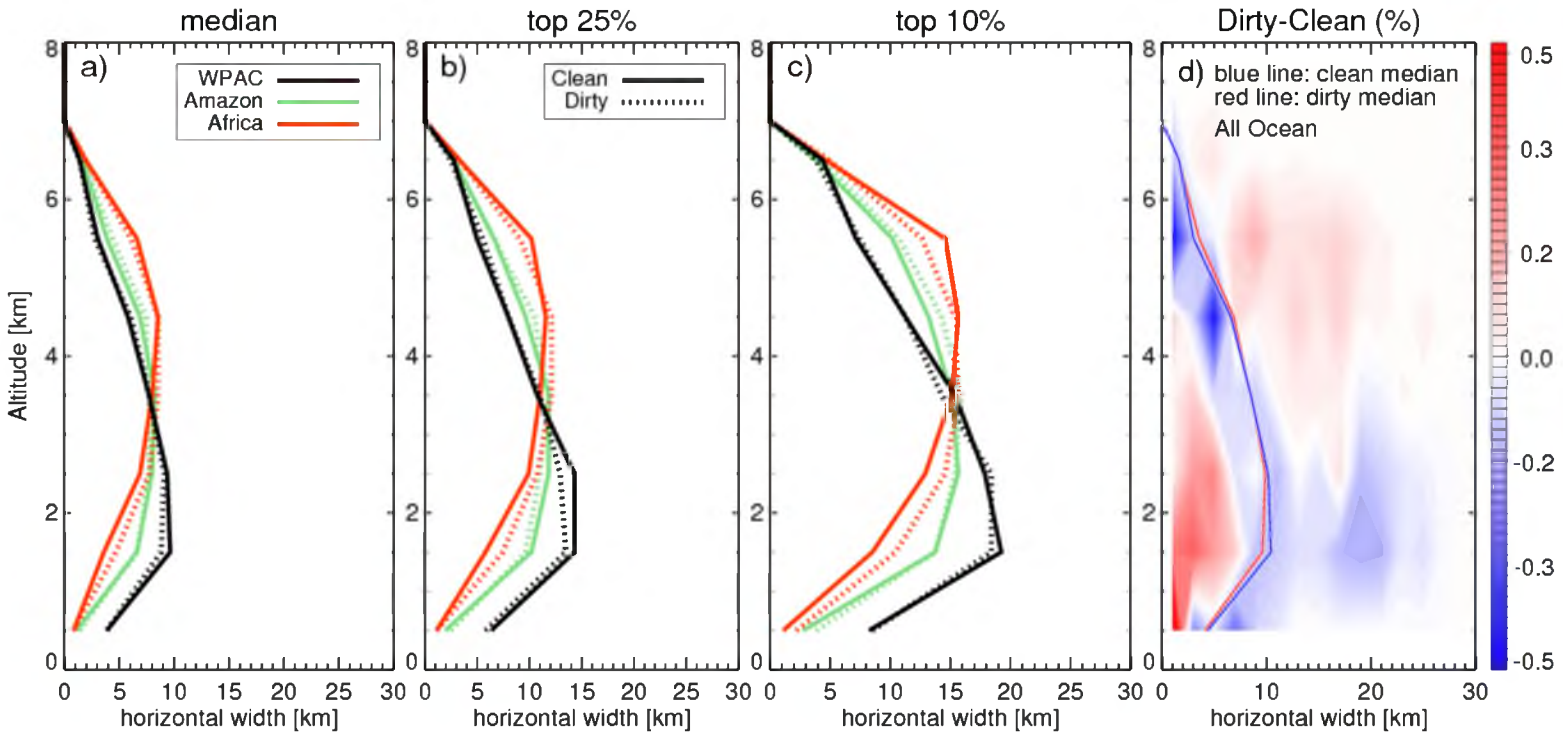

Figure 46: Profiles of the a) median, b) top 25%, and c) top 20% number of -20 dBZ pixels at each level for clean and dirty congestus in the three regions of interest. Panel (d) shows the differences between dirty and clean occurrence for all ocean congestus, with the median lines for clean (blue) and dirty (red) congestus. The differences between the means of clean and dirty widths are not statistically different using a T-test, although the means of the clean and dirty ocean widths are different at the 99% level everywhere except at 3 km.

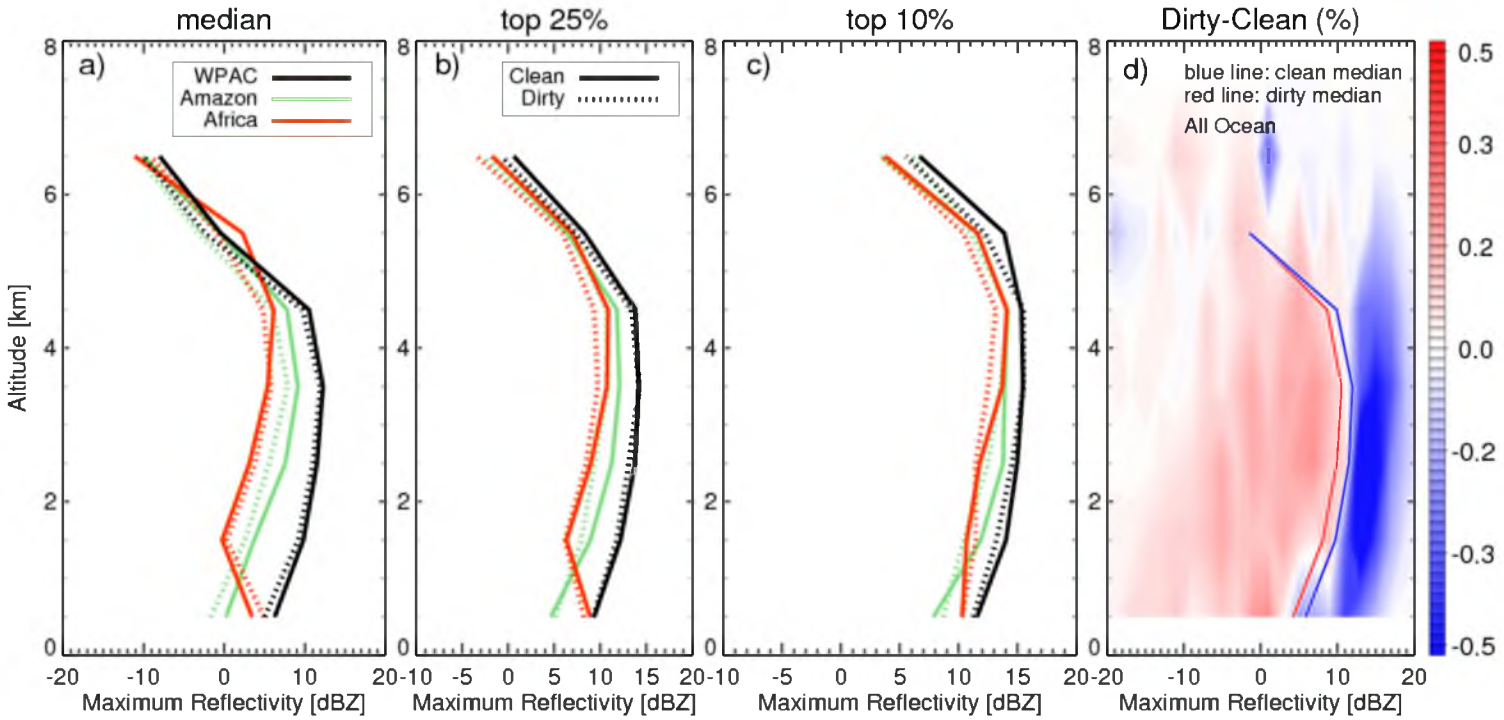

Figure 47: Profiles of the a) median, b) top 25%, and c) top 20% of maximum reflectivity at each level for clean and dirty congestus in the three regions of interest. Panel (d) shows the differences between dirty and clean occurrence for all ocean congestus, with the median lines for clean (blue) and dirty (red) congestus. . The differences between the means of clean and dirty maximum reflectivity are not statistically different using a T-test, although the means of the clean and dirty ocean maximum reflectivity are different at the 99% level everywhere except at 5 km.

panel d), clean congestus have higher values of reflectivity than dirty congestus, with the exception of the lowest levels in Africa. This result is straightforward- clean congestus should have fewer CCN and larger cloud droplets or rain, resulting in a higher reflectivity. Unfortunately, the means of clean and dirty reflectivities for individual regions are not significantly different at the 99% level. However, differences in clean and dirty reflectivities for all ocean features are significantly different at the 99% level for each vertical level except 5 km.

In using CloudSat to answer these questions about the microphysical effects of aerosols on clouds, using radar reflectivity alone could be misleading because many combinations of drop size distributions and number concentration can create the same value of reflectivity. We can gain some insight by using a radar simulator, making simple assumptions about drop size and liquid water content. Figure 48 shows simulated reflectivity from a 94 GHz radar associated with droplets of different sizes assuming a monodisperse distribution of droplets between 1-5 km. This plot was created using the Quickbeam radar simulator (Haynes et al. 2007). According to Glickman (2000), 0.2 mm diameter has been suggested as an upper limit for cloud droplets. Using this metric, the cool colors on the plot show cloud droplets, while the warm colors show rain drops.

A few important conclusions can be derived from this figure. First, the transition between Mie and Raleigh scattering at the wavelength of the CloudSat CPR can be observed. Cloud droplets are small enough to be within the regime of Raleigh scattering. As the cloud droplet size increases, the reflectivity increases as D^6. Larger rain drops are big enough to be Mie scatterers. In a Mie scattering regime (which would occur with particle diameter approaching 1/6 or more of the CloudSat wavelength of around 3 mm),

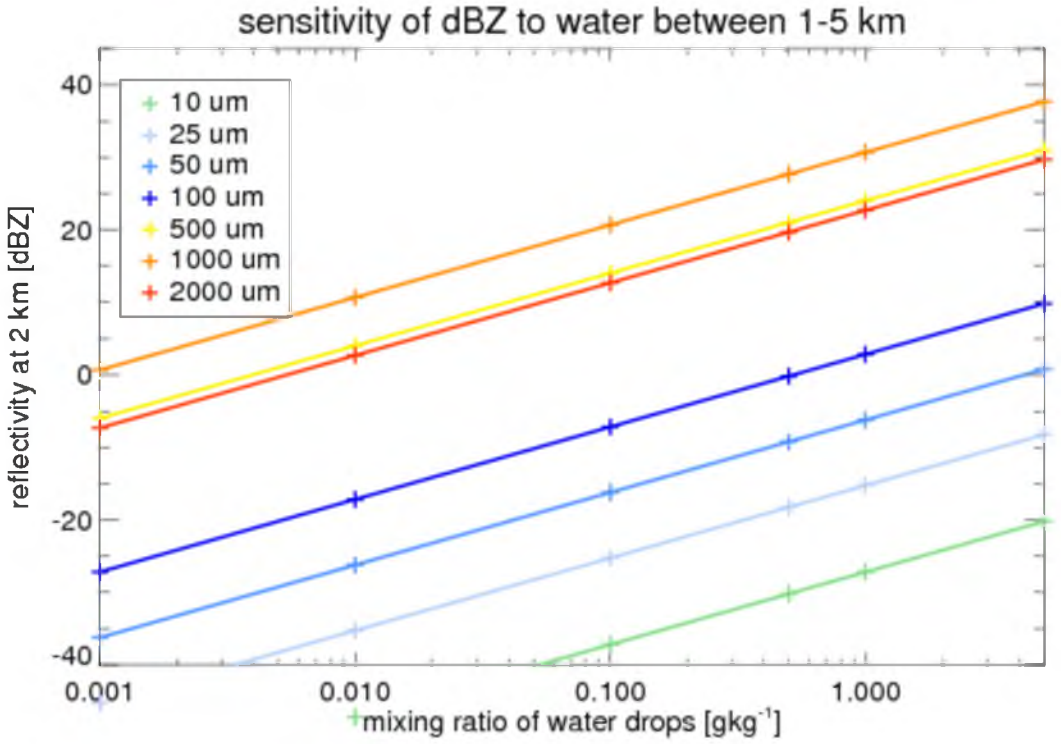

Figure 48: Dependence of 2 km simulated reflectivity at the 94 GHz frequency on mixing ratio and diameter of water drops for a monodisperse distribution between 1-5 km.

a greater amount of forward scattering reduces the amount of radiation scattered back to the radar, thus decreasing the reflectivity observed by the radar. As drop size gets larger within the Mie regime, observed reflectivity oscillates based on constructive and destructive interference within the radiation but generally increases as D^2. The top three lines in this plot show drops of diameter 0.5 mm, 1 mm, and 2 mm. For a given water content, reflectivity increases for drop sizes from 0.5 mm to 1 mm, but the value of reflectivity for 2 mm drops and is similar to that for 0.5 mm diameter drops.

This plot also demonstrates the difference in reflectivity between cloud droplets and rain drops. Over 1 gkg^{-1} of cloud droplets are required to reach 5 dBZ, but the same reflectivity could be achieved by only around 0.01 gkg^{-1} of rain drops. The congestus used in this study are only required to reach -5 dBZ. At -5 dBZ, it is quite possible for a congestus to consist of only cloud droplets. For higher reflectivities (most congestus in this study reach 0 dBZ and many exceed 8 dBZ, see Figure 36) CloudSat is almost certainly observing rain drops. Many smaller clouds that could be considered congestus are likely omitted from this study by requiring a minimum reflectivity of -5 dBZ. If 10 dBZ is used as a threshold for raining congestus, Figure 43 shows that a greater number of the population of congestus over the WPAC are raining, matching the results found with VIRS (Figure 33).

The wavelength of the CloudSat radar causes other difficulties in observing congestus as well. Attenuation of the CloudSat radar in precipitation is a known difficulty (Battaglia et al. 2008). Attenuation can be determined as in TRMM by using the surface reference technique, in which the difference between the observed peak in surface reflectivity and the expected surface reflectivity is used to estimate path integrated

attenuation. Many cross sections of the congestus used in this study are observed to have areas where the surface reflectivity is lower than expected due to attenuation. A discussion of attenuation issues with millimeter wave radars can be found in Stephens and Wood (2007).

Path integrated attenuation also helps to determine the amount of multiple scattering occurring within the CloudSat footprint. Increases in reflectivity due to multiple scattering can partially compensate for losses due to attenuation (Battaglia et al. 2008). Battaglia and Simmer (2008) found that the surface return of CloudSat is significantly contaminated at rain rates above 5 mmh^{-1}. It is likely that some of the congestus used in this study are affected by multiple scattering. Attenuation could explain the decreases in maximum reflectivity profiles of the congestus (Figures 39, 47) below 4 km.

Thus far the results with CloudSat have been restricted to differences in maximum reflectivity and cloud envelope shape. Cleaner congestus have higher reflectivities in all regions, although differences between clean and dirty maximum reflectivities within regions are not statistically significant. Adding CCN to a cluster of clean ocean congestus causes it to achieve a more muffin-like shape of the cloud envelope, which is more typical of groups of land congestus. In the WPAC region, changes in the lowest detected echo or cloud base could point to warm rain suppression. There is no evidence for invigoration, as seen in the TRMM RPFs. The population of congestus used here has more in common with shallower, warm rain clouds than with deeper convective clouds. Unfortunately CloudSat can yield only limited information about the microphysical

processes within the cloud- the CloudSat detected cloud top is above the freezing level, but the amount of ice within the cloud is unknown.

Environments of Clean and Dirty Congestus

So far the differences in clean and dirty congestus are small at best. The most systematic difference is seen in reflectivity- clean congestus clusters have higher values of reflectivity. Are there any differences in the mean environments of clean and dirty congestus? Clearly differences exist in Africa and Amazon, because the clean and dirty congestus occur in very different parts of this region (Figure 41), although this is partially due to the typical locations of biomass burning. Figure 49 shows wind roses for the three regions. In the Amazon region there are only slight differences in the distribution of 850 hPa wind directions, and in the WPAC the distributions are nearly identical. In Africa, the distributions are very similar, but there is a large peak for dirty cases with northwesterly winds. A similar peak is not apparent for clean cases, which occur more frequently with easterly winds. These wind roses show no preferred wind direction for clean or dirty cases.

The mean environmental soundings for these regions are shown in Figure 50. There are virtually no differences in mean wind direction for the Amazon for clean and dirty congestus, and differences in Africa are limited to the lowest levels. The mean profiles of temperature and dewpoint are very similar and the differences in the means are only statistically significant at a few levels in the Amazon and one level in the WPAC. CDFs of CAPE and convective inhibition (not shown) show similar distributions, with clean profiles having slightly more CAPE than dirty profiles in the Amazon, and dirty

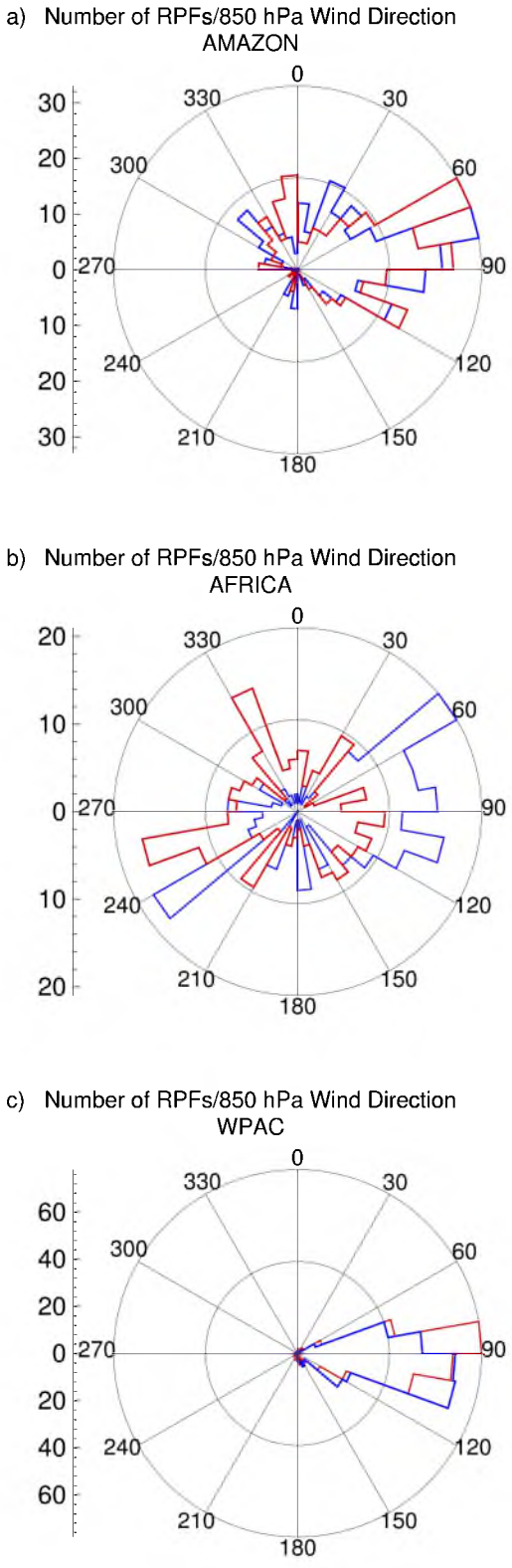

Figure 49: Wind roses for the a) Amazon, b) Africa, and c) WPAC regions. The azimuth indicates wind direction, while the range indicates number of clean (blue) and dirty (red) congestus at each direction.

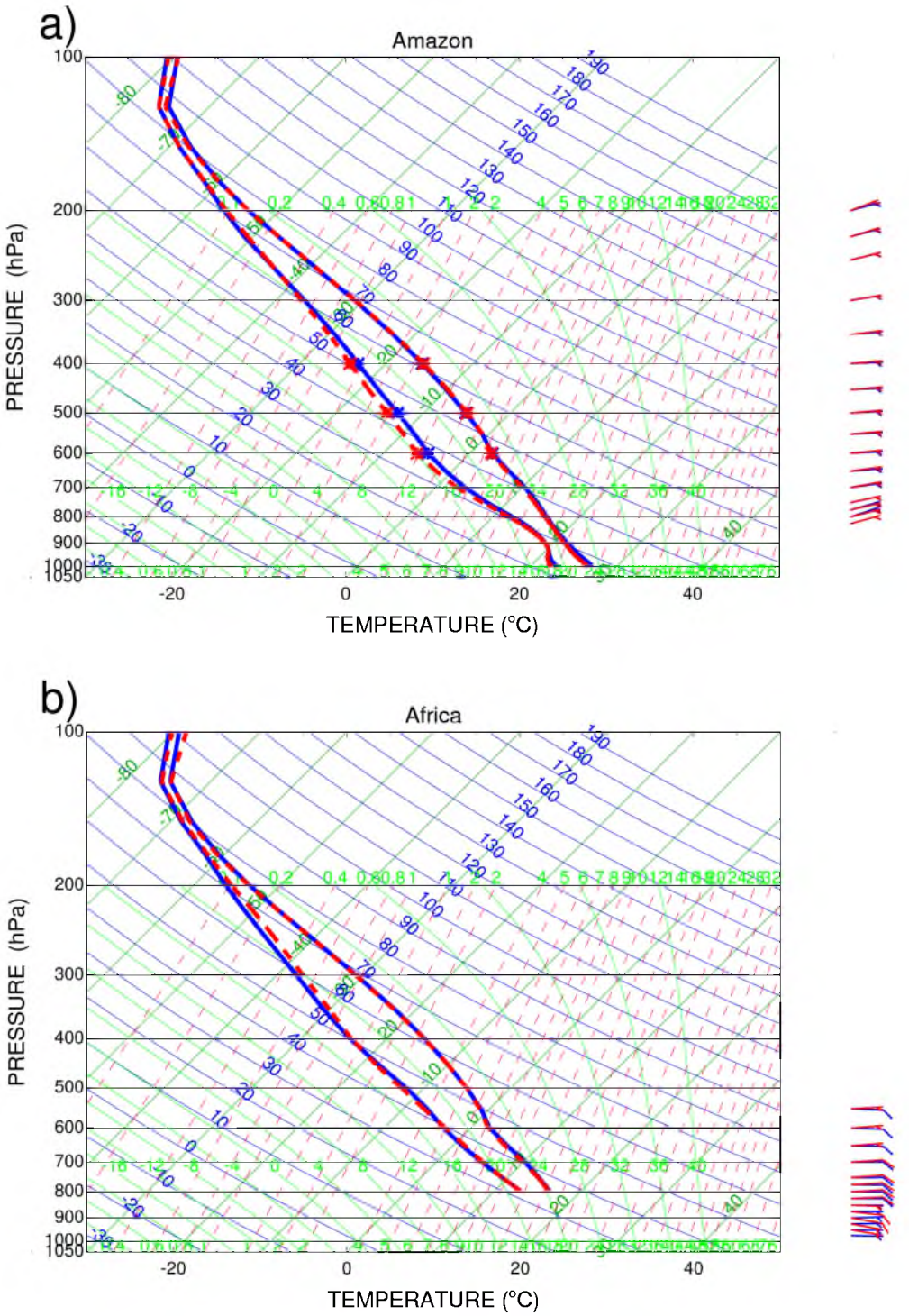

Figure 50: Thermodynamic soundings for clean (blue) and dirty (red) congestus in the a) Amazon, b) Africa, and c) WPAC regions. The dots indicate levels at which the difference in means between clean and dirty profiles of temperature and relative humidity are statistically significant at the 99% level.

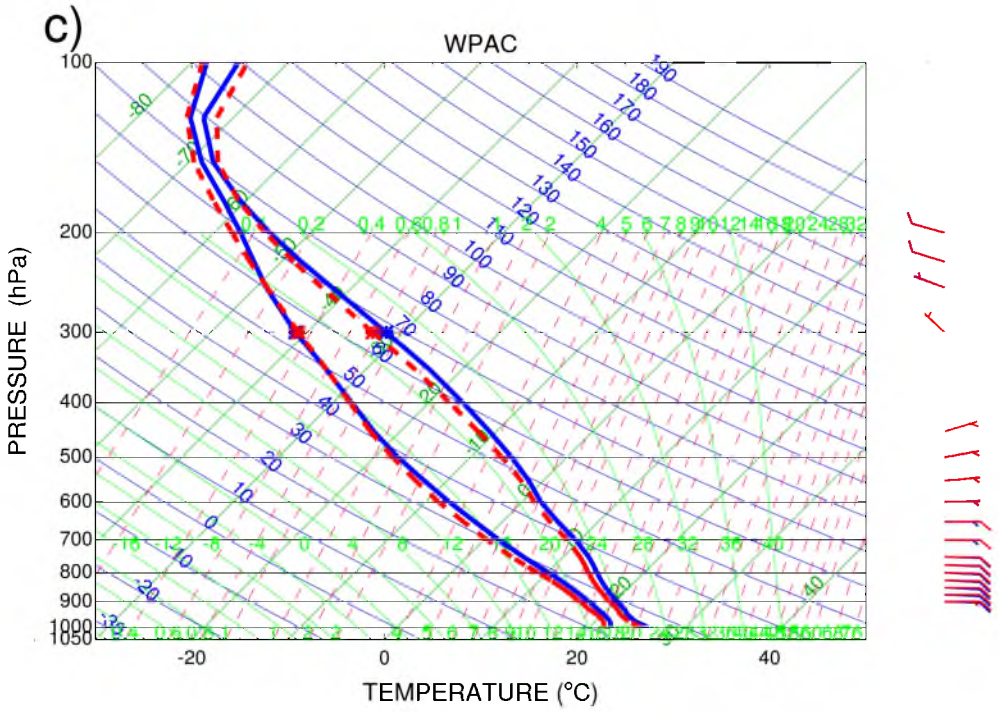

Figure 50, cont'd.

profiles having slightly larger CAPE than clean profiles in Africa. In the Amazon region, dirty congestus tend to have slightly drier air between 700 hPa and 400 hPa. For the WPAC region, dirty soundings are slightly cooler and drier.

The similarity of the clean and dirty soundings for these regions and the lack of statistically significant differences suggest that any differences between clean and dirty congestus could be due to aerosol indirect effect. Since the only significant difference observed thus far is higher reflectivities in clean congestus when compared to dirty congestus over the entire ocean, and this finding is consistent with larger cloud drop size or rain that would be expected in clean clouds, this is likely an observation of aerosol indirect effect. The observations of cloud top and echo bottom do not show any trends with increasing AI, except for echo base in the WPAC, which is small and could be explained by mechanisms other than the aerosol indirect effect. Overall the differences between land and ocean congestus are much larger than differences caused by aerosols, although a difference in the number of available CCN is one difference between land and ocean regions since land regions have much higher values of AI than ocean regions.

Sample size is one issue with these CloudSat results. While nothing in this study points to glaring aerosol indirect effects, these results do suggest that further analysis is warranted with a larger sample size. A larger sample size would undoubtedly lead to more robust statistics. Additionally the use of a better method of aerosol detection would help the analysis. Congestus are a smaller-scale phenomenon than the TRMM features observed, and small changes in aerosol concentration may not be adequately represented in the MODIS products used here.

CHAPTER 6

CONCLUSIONS

Summary and Discussion

The indirect effects of aerosols on convective clouds have been well studied using a variety of models, but observations of clouds in clean and dirty environments are critical to verifying these effects. In this study, TRMM, CloudSat, and MODIS data have been utilized in an attempt to isolate aerosol indirect effects on convective clouds. MODIS AI is used to estimate background aerosol concentration. Because the MODIS sensor cannot detect aerosols within cloud, values from a rather large area are averaged to obtain AI. When identifying clouds occurring in clean and dirty environments, only the top and bottom quartiles are used. This should ensure that the estimate is representative of a fairly large area surrounding the target cloud at the time of MODIS overpass.

Assuming that the value of MODIS AI represents the environment around the features remains the Achilles heel of the methods used in this study. Assumptions within the MODIS algorithms (particularly assuming that aerosols are spherical) can introduce uncertainty in the value of AI. Additionally, when collocating AI with TRMM RPFs and CloudSat congestus, lengthy periods of time can exist between the different overpasses. On the whole, saying that satellite-based estimates of AI can correctly represent the CCN

concentration on meso- and micro- scales is a significant leap; however, the products and methodology used here are commonly used and represent the best of our satellite remote-sensing abilities for aerosols at this time.

Assuming that the MODIS aerosol estimates are reasonable, and despite difficulties in collocation, differences are observed in TRMM RPFs in clean and dirty environments. RPFs, representing deeper convection, in dirty environments consistently have higher reflectivities, taller echo tops, and more lightning in the Amazon and Africa regions. These regions are influenced by biomass burning, which releases black carbon as well as other particulates. In the NAM region, RPFs in clean environments actually have more flashes, and this is thought to be a result of the aerosol source. If the observed aerosol is dust being lofted by outflow from monsoonal thunderstorms, dirty environments may actually represent monsoon burst periods, which are characterized by widespread convection. Weaker convection could be affecting the lightning statistics. In the Atlantic region, slightly lower echo tops are observed in dirty clouds. Aerosol in the Atlantic region is likely to be a mix of dust and anthropogenic pollution from Europe, which is transported from the Sahara to the northeast (Garrett et al. 2003). The distribution of aerosol index in the Atlantic is very narrow, and the lower limit for "dirty" values of AI is low. Because the difference in AI is comparatively small between "clean" and "dirty" RPFs in the Atlantic region, it is possible that aerosol indirect effects are hidden by these definitions.

Examining the mean environments of these regions shows that environment is very important when attempting to draw conclusions about aerosol indirect effects. Because convective clouds are driven by buoyancy forces, which are extremely sensitive

to small differences in their environment, it is very difficult to separate out the effects of aerosols. When comparing clean and dirty thermodynamic soundings, each region shows statistically significant differences between the two profiles. In the NAM region, the dirty sounding is much more moist. The dirty and clean soundings look remarkably like burst and break soundings, respectively. In the Atlantic, which has the least differences of all the regions, a layer of dry air at mid-levels is present in the mean dirty sounding, indicative of the Saharan Air Layer, which is likely the source of the dust causing increased values of AI. In Africa, dirty soundings are drier at mid-levels and much more unstable. The differences between clean and dirty soundings in Africa are the greatest of any region. The Amazon shows small thermodynamic differences between clean and dirty, a fact noted by Freud et al. (2008), but there is still a layer of drier air at the mid-levels in the mean dirty sounding. These environmental differences make it impossible to attribute the changes in clean and dirty RPFs to aerosol indirect effect alone.

Separating the RPFs into different environments did not show any remarkable results, either. There is no environment in which differences between clean and dirty RPFs are maximized, and there are no systematic differences between the distributions of clean and dirty convective parameters in different environments. Modeling studies have shown that, all else equal, the aerosol indirect effect is more apparent in environments with low CAPE. Finding environments that differ only by CAPE is, of course, impossible observationally, and manually separating RPFs by mid-level relative humidity, shear vector, and CAPE do not elucidate the ideas regarding the effects of aerosols in different environments.

While the impacts of aerosols on these deeper convective clouds are not shown convincingly by the TRMM RPFs, some argument can be made that buffering by the environment is acting to hide the aerosol signal. Buffering refers to the idea that changes in an isolated cloud could be cancelled out or compensated for by opposing changes that become evident when the system is examined as a whole (Stevens and Feingold 2009). The changes over the life of a cloud system due to aerosols may end up being negligible as the environment compensates in ways that cannot be detected in this study. Because of some of these difficulties, congestus clouds are examined. Congestus clouds are smaller, less complicated structurally, and may exhibit aerosol indirect effects more visibly.

The CloudSat radar is an excellent tool for defining congestus. In this study, congestus are defined as having tops between 5-8 km, bases within 1.5 km of the terrain height, a maximum reflectivity reaching -5 dBZ, thickness of at least 4 km, and a horizontal (along track) width of less than 30 CloudSat pixels (around 33 km). Using this population to determine properties of congestus as well as the effects of aerosols on congestus is important, as they contribute around 18% of the population of low clouds in South America, central Africa, and the Maritime Continent. The congestus identified in this manner are not single clouds, but rather groups of congestus clouds, smeared together by the CloudSat footprint.

Congestus over the ocean have different properties and are shaped differently from congestus over land, although congestus in this case can refer to groups of congestus clouds. Oceanic congestus tend to have higher maximum reflectivities, lower echo bases, and lower cloud tops than land congestus. Additionally, oceanic congestus are more "bell-shaped" while land congestus are more "muffin-shaped". When

examining congestus occurring over the ocean in clean and dirty environments, dirty ocean congestus have wider tops and are shaped more like land congestus. If 10 dBZ is used as a threshold to separate raining congestus from those that may not be raining, more of the ocean congestus are raining.

The effects of aerosols on congestus manifest themselves almost solely in the reflectivities observed by CloudSat. Clean congestus have higher reflectivities, as would be expected in a cleaner cloud with fewer CCN and larger cloud droplets and rain. In some regions, differences in echo base height or thickness are observed, but the sample size of CloudSat congestus is much smaller than the number of TRMM RPFs. These results are interesting enough to warrant further study with other instrumentation that can produce a larger sample size, which would lead to more robust statistics. Additionally, the effects of aerosols on congestus would be better studied using a method that can detect aerosols on a smaller scale than the MODIS product used here.

The effects of aerosols on smaller clouds, such as the congestus features identified by CloudSat, and larger, deep clouds with ice processes, such as the RPFs observed using TRMM, are expected to be different. For warm rain clouds, a reduction of rainfall is expected, as coalescence and collision processes are suppressed. For deeper clouds that contain significant quantities of ice, an increase in convective intensity is expected. One goal of using congestus that reach above the freezing level was to investigate the change in between these categories. What is the tipping point that a cloud must reach in order to move from suppression by aerosols to invigoration by aerosols? This question was not answered by this study, but is worth further investigation. Perhaps limiting the sample to congestus with tops above -10°C would elucidate this matter.

The primary conclusions of this study can be summed up by the following statements:

On aerosol indirect effects upon TRMM RPFs (deeper convective features):

- In the regions studied, sufficient environmental differences exist between clean and dirty RPFs observed by TRMM to suggest that environment is responsible for some of these differences, and that invigoration cannot be attributed to aerosol indirect effect alone.
- When similar environments are grouped, there is no environment in which the differences between clean and dirty features are systematically larger (or smaller).

On defining congestus:

- Congestus are found most frequently in the Tropics, particularly along the ITCZ and make up anywhere from 0-12% of clouds. A significant maximum in the occurrence of congestus is observed in the Amazon.
- Groups of congestus occurring over land are shaped differently from groups of congestus over the ocean and have different properties.

On congestus and the aerosol indirect effect:

- Congestus occurring in clean environments have higher maximum reflectivities than congestus occurring in dirty environments.
- Due to the problems in separating out environmental effects from those of aerosols, it is very difficult to conclusively show the aerosol indirect effect using observations.

Aerosols must have some effects on convective clouds. The indirect effect has been observed in case studies (Rosenfeld et al. 1999, Williams et al. 1999). Other satellite-based studies show invigoration by aerosols (Lin et al. 2006, Jiang et al. 2008, Koren et al. 2010, Heiblum et al. 2012, Storer et al. 2013). Some of these studies do not include an in depth look at environment, which is critical to isolating the indirect effect. Either the effects of buffering are restricting our ability to observe aerosol indirect effects or the signal of the aerosol indirect effect in a large, satellite-based dataset is simply too small to be observed conclusively using these methods. This signal could be hiding in the assumptions of the aerosol algorithms, in the technique used to identify mean background aerosol index, or in the time lag between satellite overpasses. Perhaps the aerosol indirect effect is too small to exert any significant changes for the temporal and spatial scales analyzed in this study. The true magnitude of the aerosol indirect effect remains elusive on a global scale.

Future Work

This study appears to point very clearly to the inadequacies of current satellite instruments and algorithms to observe aerosols at the level needed to determine aerosol indirect effects on convective clouds. At this point, further investigation by satellites would not be as useful as improving ground-based measurements of aerosols in the vicinity of a radar with the ability to obtain full life cycles of convective clouds or implementing a larger-scale field study involving the collocation of ground-based radars with aircraft equipped with aerosol sensors. The satellites used in this study only view a snapshot of these clouds, but modeling studies point to aerosol effects on cloud lifetime.

Observations are critical to verifying these modeling studies, but current observational networks are inadequate to answer these important questions. Collocation of aerosol sensors that can resolve aerosol size and composition with cloud and precipitation radars are necessary to make strides in this field. Additional measurements of cloud droplet size distribution and drop size distribution would also help verify the microphysical effects of aerosols on clouds.

Aerosol composition is one important factor in aerosol indirect effect that is frequently overlooked. Measurements of AOD and AI provide information about the amount of scattering caused by aerosols, which is related to aerosol amount, but aerosol composition and aerosol size are also important. Perhaps through a detailed study comparing ground-based aerosol measurements to MODIS fine- and course- mode AOD, an algorithm can be determined to provide more information about aerosol composition, in addition to aerosol size.

REFERENCES

Ackerman, S. A., K. I. Strabala, W. P. Menzel, R. A. Frey, C. C. Moeller, and L. E. Gumley, 1998: Discriminating clear sky from clouds with MODIS. *J. Geophys. Res.*, **103**, doi: 10.1029/1998JD200032.

Albrecht, B. A., 1989: Aerosols, cloud microphysics, and fractional cloudiness. *Science*, **245**, 1227-1230. doi:10.1126/science. 245.4923.1227.

Andreae, M. O., D. Rosenfeld, P. Artaxo, A. A. Costa, G. P. Frank, K. M. Longo, and M. A. F. Silva-Dias, 2004: Smoking rain clouds over the Amazon, *Science*, **303**, 1337-1342. doi:10.1126/ science.1092779.

Artaxo, P., L. V. Rizzo, M. Paixão, S. de Lucca, P. H. Oliveira, L. L. Lara, K. T. Wiedemann, M. O. Andreae, B. Holben, J. Schafer, A. L. Correia, and T. M. Pauliquevis, 2009: Aerosol particles in Amazonia: Their composition, role in the radiation balance, cloud formation, and nutrient cycles, in *Amazonia and Global Change*, *Geophys. Monogr. Ser.*, vol. 186, edited by M. Keller et al., pp. 233–250, AGU, Washington, D. C., doi:10.1029/2008GM000778.

Awaka, J., T. Iguchi, H. Kumagai, and K. Okamoto, 1997: Rain type Classification Algorithm for TRMM Precipitation Radar. *Proc. IEEE 1997 In. Geoscience and Remote Sensing Symp*. Sinagapore, Japan, Institute of Electrical and Electronics Engineers, 1633-1635.

Battaglia, A., and C. Simmer, 2008: How does multiple scattering affect the spaceborne W-band radar measurements at ranges close to and crossing the sea surface range?, *IEEE Trans. Geosci. Remote Sens.*, **46(6)**, 1644 – 1651. doi:10.1109/TGRS.2008.916085

Battaglia, A., J. M. Haynes, T. L'Ecuyer, and C. Simmer, 2008: Identifying multiple-scattering-affected profiles in CloudSat observations over the oceans, *J. Geophys. Res.*, **113**, D00A17, doi:10.1029/2008JD009960.

Berg, W., T. L'Ecuyer, C. Kummerow, 2006: Rainfall Climate Regimes: The Relationship of Regional TRMM Rainfall Biases to the Environment. *J. Appl. Meteor. Climatol.*, **45**, 434–454. doi: 10.1175/JAM2331.1.

Berg, W., T. L'Ecuyer, and S. van den Heever, 2008: Evidence for the impact of aerosols on the onset and microphysical properties of rainfall from a combination of satellite observations and cloud resolving model simulations. *J. Geophys. Res.*, **113**, D14S23. doi:10.1029/2007JD009649.

Berg, W., T. L'Ecuyer, J. M. Haynes, 2010: The Distribution of Rainfall over Oceans from Spaceborne Radars. *J. Appl. Meteor. Climatol.*, **49**, 535–543. doi: 10.1175/2009JAMC2330.1

Bluestein, H. B., 1993: *Synoptic–Dynamic Meteorology in Midlatitudes (Vol. II): Observations and Theory of Weather Systems.* Oxford University Press, 594 pp.

Brennan, J. I., Kaufman, Y. J., Koren, I., & Li, R. R., 2005: Aerosol-cloud interaction-misclassification of MODIS clouds in heavy aerosol. *Geoscience and Remote Sensing, IEEE Transactions on*, ***43.4***, pp. 911. doi: 10.1109/TGRS.2005.844662.

Bretherton, Christopher S., Piotr K. Smolarkiewicz, 1989: Gravity Waves, Compensating Subsidence and Detrainment around Cumulus Clouds. *J. Atmos. Sci.*, **46**, 740–759. doi: 10.1175/1520-0469(1989)046<0740:GWCSAD>2.0.CO;2

Casey, S., A. Dessler, and C. Schumacher, 2007: Frequency of tropical precipitating clouds as observed by the Tropical Rainfall Measuring Mission Precipitation Radar and ICESat/Geoscience Laser Altimeter System. *J. Geophys. Res.*, **112.**D14215, doi:10.1029/2007JD008468.

Casey, S. P. F., Fetzer, E. J., and Kahn, B. H., 2011: Revised identification of tropical oceanic cumulus congestus as viewed by CloudSat, *Atmos. Chem. Phys. Discuss.*, **11**, 14883-14902, doi:10.5194/acpd-11-14883-2011.

Chen, Q.,Y. Yin, L. Jin, H. Xiao, S. Zhu, 2011: The effect of aerosol layers on convective cloud microphysics and precipitation. *Atmos. Res.*, **101**, 327-340. 10.1016/j.atmosres.2011.03.007. doi: 10.1016/j.atmosres.2011.03.007.

Chin, M., T. Diehl, P. Ginoux, W. and Malm, 2007: Intercontinental transport of pollution and dust aerosols: implications for regional air quality, *Atmos. Chem. Phys.*, 7, 5501-5517, doi:10.5194/acp-7-5501-2007.

Cifelli, R., S. W. Nesbitt, S. A. Rutledge, W. A. Petersen, S. Yuter, 2007: Radar Characteristics of Precipitation Features in the EPIC and TEPPS Regions of the East Pacific. *Mon. Wea. Rev.*, **135**, 1576–1595, doi:10.1175/MWR3340.1.

Dusek, U., G. P. Frank, L. Hildebrandt, J. Curtius, J. Schneiger, S. Walter, D. Chand, F. Drewnik, S. Hings, D. Jung, S Borrmann, M. O. Andreae, 2006: Size matters more than chemisty for cloud-nucleating ability of aerosol particles. *Science*, **312**, 1375-1378, doi: 10.1126/science.1125261

Ellis, T. D., T. L'Ecuyer, J. M. Haynes, and G. L. Stephens, 2009: How often does it rain over the global oceans? The perspective from CloudSat, *Geophys. Res. Lett.*, **36**, L03815, doi:10.1029/2008GL036728.

Emanuel, K. A., 1997: The problem of convective moistening. *The Physics and Parameterization of Moist Atmospheric Convection,* R. K. Smith, Ed., NATO ASI Series, Kluwer Academic, 447–462.

Fan, J. R., R. Zhang, G. Li, W.-K. Tao, 2007: Effects of aerosols and relative humidity on cumulus clouds. *J. Geophys. Res.*, **112**, D14204. doi:10.1029/2006JD008136.

Fan, J., T. Yuan, J. Comstock, S. Ghan, A. Khain, L.R. Le- ung, Z. Li, J. V. Martins, and M. Ovchinnikov, 2009: Dominant role by vertical wind shear in regulating aerosol effects on deep convective clouds. *J. Geophys. Res.*, **114**, D22206. doi:10.1029/2009JD012352.

Freud, E., D. Rosenfeld, M. O. Andreae, A. A. Costa, and P. Artaxo, 2008: Robust relations between CCN and the vertical evolution of cloud drop size distribution in deep convective clouds. *Atmos. Chem. Phys.*, ***8***, 1661-1675. doi: hal.archives-ouvertes.fr:hal-00296497.

Fridland, A. M., A. Ackerman, E. Jensen, A. Heymsfeld, M. Poellot, D. Stevens, D. Wang, L. Miloshevich, D. Baumgardner, R.P. Lawson, J. C. Wilson, R. C. Flagan, J. H. Seinfeld, H. H. Jonsson, T. M. VanReken, V. Varutbangkul, T. Rissman, 2004: Evidence for the predomi- nance of mid-tropospheric aerosols as subtropical anvil cloud nuclei. *Science*, **304**, 718–722.

Garrett, T. J., L. M. Russell, V. Ramaswamy, S. F. Maria, and B. J. Huebert,2003: Microphysical and radiative evolution of aerosol plumes over the tropical North Atlantic Ocean, *J. Geophys. Res.*, **108(D1)**, 4022, doi:10.1029/2002JD002228.

Gassó, S., D. A. Hegg, D.S Covert, D. Collins, D., K. J. Noone, E. Öström,, B. Schmit, P. B. Russell, J. M. Livingston, P. A. Durkee, and H. Jonsson, 2000: Influence of humidity on the aerosol scattering coefficient and its effect on the upwelling radiance during ACE-2. *Tellus B*, **52**, 546–567. doi: 10.1034/j.1600-0889.2000.00055.x

Glickman, T. S., 2000: *AMS Glossary of Meteorology*, American Meteorology Society, Boston, USA, 855 pp.

Gunn, R, and B. B. Phillips, 1957: An experimental investigation of the effent of air pollution on the initiation of rain. *J. Meteor.*, **14**, 272–280. doi: 10.1175/1520-0469(1957)014<0272:AEIOTE>2.0.CO;2

Gunthe, S. S., S.M. King, D. Rose, Q. Chen, P. Roldin, D. K. Farmer, J. L. Jimenez, P. Artaxo, M. O. Andreae, S. T. Martin, U. and Pöschl, 2009: Cloud condensation nuclei in pristine tropical rainforest air of Amazonia: size-resolved measurements

and modeling of atmospheric aerosol composition and CCN activity, *Atmos. Chem. Phys.*, **9**, 7551-7575, doi:10.5194/acp-9-7551-2009.

Hall, T. J., and T. H. Vonder Haar, 1999: The diurnal cycle of west Pacific deep convection and its relation to the spatial and temporal variation of tropical MCSs, *J. Atmos. Sci.*, **56**, 3401-3415, doi: 10.1175/1520-0469(1999)056<3401: TDCOWP>2.0.CO;2.

Hahn, C. J., W. B. Rossow, S. G. Warren, 2001: ISCCP Cloud Properties Associated with Standard Cloud Types Identified in Individual Surface Observations. *J. Climate*, **14**, 11–28. doi: 10.1175/1520-0442(2001)014<0011:ICPAWS >2.0.CO;2

Han, Q., W. B. Rossow, and A. A. Lacis, 1994: Near-global survey of effective droplet radii in liquid clouds using ISCCP data, *J. Climate*, **7**, 465-497. doi:10.1175/1520-0442(1994) 007<0465:NGSOED>2.0.CO;2.

Haynes, J.M., R.T. Marchand, Z. Luo, A. Bodas-Salcedo, and G.L. Stephens, 2007: A multi-purpose radar simulation package: QuickBeam. *Bull. Amer. Meteor. Soc.*, **88**, 1723-1727.

Heiblum, R. H., I. Koren, and O. Altaratz, 2012: New evidence of cloud invigoration from TRMM measure- ments of rain center of gravity, *Geophys. Res. Lett.*, **39**, L08803, doi:10.1029/2012GL051158.

Hohenegger, C. and B. Stevens, 2013: Preconditioning Deep Convection with Cumulus Congestus. *J. Atmos. Sci.*, **70**, 448–464. doi: 10.1175/JAS-D-12-089.1

Huang, J., A. Adams, C. Wang, C. Zhang, 2009: Black Carbon and West African Monsoon precipitation: observations and simulations. *Ann. Geophys.*, **27**, 4171-4181, doi:10.5194/angeo-27-4171-2009.

Iguchi, T., T. Kozu., R. Meneghini, J. Awaka, and K. Okamoto, 2000: Rain-profiling algorithm for the TRMM precipitation radar. *J. Appl. Meteor.*, **39**, 2038-2052. doi: 10.1175/1520-0450(2001)040<2038:RPAFTT >2.0.CO;2.

Jensen, M. P., A.D. Del Genio, 2006: Factors Limiting Convective Cloud-Top Height at the ARM Nauru Island Climate Research Facility. *J. Climate*, **19**, 2105–2117, doi:10.1175/JCLI3722.1.

Jiang, J. H., H. Su, M. R. Schoeberl, S. T. Massie, P. Colarco, S. Platnick, and N. J. Livesey, 2008: Clean and polluted clouds: Relationships among pollution, ice clouds, and precipitation in South America, *Geophys. Res. Lett.*, LI4804. doi:10.1029/2008GL034631.

Johnson, R. H., T. M. Rickenbach, S. A. Rutledge, P. E. Ciesielski, W. H. Schubert, 1999: Trimodal Characteristics of Tropical Convection. *J. Climate*, **12**, 2397–2418, doi: 10.1175/1520-0442.

Jones, T. A. and S. A. Christopher, 2010: Statistical properties of aerosol-cloud-precipitation interactions in South America, *Atmos. Chem. Phys.*, **10**, 2287-2305, doi:10.5194/acp-10-2287-2010.

Karydis, V. A., P. Kumar, D. Barahona, I. N. Sokolik, and A. Nenesk, 2011: On the effect of dust particles on global cloud condensation nuclei and cloud droplet number, *J. Geophys. Res.*, **116**, D23204, doi:10.1029/2011JD016283.

Kaufman, Y. J., D. Tanré, L. A. Remer, E. Vermote, A. Chu, and B. N. Holben, 1997: Operational remote sensing of tropospheric aerosol over land from EOS moderate resolution imaging spectroradiometer, *J. Geophys. Res.*, **102**, 17051–17067. doi:10.1029/96JD03988.

Kemball-Cook, S. R., B. C. Weare, 2001: The Onset of Convection in the Madden–Julian Oscillation. *J. Climate*, **14**, 780–793, doi: 10.1175/1520-0442(2001)014<0780: TOOCIT>2.0.CO;2 .

Kikuchi, K. and Y. N. Takayabu, 2004: The development of organized convection associated with the MJO during TOGA COARE IOP: Trimodal characteristics, *Geophys. Res. Lett.*, **31**, L10101, doi:10.1029/2004GL019601.

Kiladis, G. N., K. H. Straub, P. T. Haertel, 2005: Zonal and Vertical Structure of the Madden–Julian Oscillation. *J. Atmos. Sci.*, **62**, 2790–2809. doi: 10.1175/JAS3520.1.

Khain, A. P., 2009: Notes on state-of-the-art investigations of aerosol effects on precipitation: a critical review. *Environ. Res. Lett.*, **4**, 015004, doi:10.1088/1748-9326/4/1/015004.

Khain, A., A. Pokrovsky, 2004: Simulation of Effects of Atmospheric Aerosols on Deep Turbulent Convective Clouds Using a Spectral Microphysics Mixed-Phase Cumulus Cloud Model. Part II: Sensitivity Study. *J. Atmos. Sci.*, **61**, 2983–3001, doi:10.1175/JAS-3350.1.

Khain, A. P., A. Pokrovsky, M. Pinsky, A. Seifert, and V. Phillips, 2004: Simulation of effects of atmospheric aerosols on deep turbulent convective clouds using a spectral microphysics mixed-phase cumulus cloud model. Part I: Model description and possible applications. *J. Atmos. Sci.*, **61**, 2963–2982, doi:10.1175/JAS-3281.1.

Khain, A. P., D. Rosenfeld, and A. Pokrovsky, 2005: Aerosol impact on the dynamics and microphysics of deep convective clouds. *Quart. J. Roy. Meteor. Soc.*, **131**, 2639–2663, doi:10.1256/ qj.04.62.

Khain, A. P., N. BenMoshe, and A. Pokrovsky, 2008: Factors determining the impact of aerosols on surface precipitation from clouds: An attempt at classification. *J. Atmos. Sci.*, **65**, 1721– 1748, doi:10.1175/2007JAS2515.1.

King, M.D. W. P. Menzel, Y. J. Kaufman, D. Tanre, B. Gao; S. Platnick, S. A. Ackerman, L.A. Remer, R. Pincus, P.A. Hubanks, 2003: Cloud and aerosol properties, precipitable water, and profiles of temperature and water vapor from MODIS, *IEEE Trans. Geosci. Remote Sens.*, **41**, 442- 458, doi: 10.1109/TGRS.2002.808226.

Koren I., Martins J. V., Remer L. A., and Afargan H., 2008: Smoke invigoration versus inhibition of clouds over the Amazon, *Science,* **321**, 946–949, doi:10.1126 /science.1159185.

Koren, I., G. Feingold, and L. A. Remer, 2010: The invigoration of deep convective clouds over the Atlantic: aerosol effect, meteorology, or retrieval artifact?, *Atmos. Chem. Phys.*, **10**, 8855-8872, doi:10.5194/acp-10-8855-2010.

Koren, I., O. Altaratz, L. A. Remer, G. Feingold, J. V. Martins, and R. H. Heiblum, 2012: Aerosol-induced intensification of rain from the tropics to the mid-latitudes. *Nature Geosci.*, 1752-0908, doi:10.1038/ngeo1364.

Kummerow, C., W. Barnes, T. Kozu, J. Shiue, and J. Simpson, 1998: The Tropical Rainfall Measuring Mission (TRMM) Sensor Package. *J. Atmos. Oceanic Technol.*, **15**, 809-817, doi: 10.1175/1520-0426(1998)015<0809: TTRMMT>2.0.CO;2.

Lebsock, M. D., G. L. Stephens, and C. Kummerow, 2008: Multisensor satellite observations of aerosol effects on warm clouds. *J. Geophys. Res.,* **113**, D15205, doi:10.1029/2008JD009876.

Lebsock, M. D. and T. S. L'Ecuyer, 2011: The retrieval of warm rain from CloudSat, *J. Geophys. Res.,* **116**, D20209, doi:10.1029/2011JD016076.

Lee, S. S., 2011: Dependence of aerosol-precipitation interactions on humidity in a multiple-cloud system. *Atmos. Chem. Phys.* **11**, 2179-2196 , doi:10.5194/acp-11-2179-2011.

Lee, S. S., L. J. Donner, V. T. J. Phillips, and Y. Ming, 2008: The dependence of aerosol effects on clouds and precipitationon cloud-system organization, shear, and stability, *J. Geophys. Res.*, **113**, D16202 , doi:10.1029/2007JD009224.

Levy, R. C., L. A. Remer, D. Tanré, Y. J. Kaufman, C. Ichoku, B. Holben, J. M. Livingston, P. B. Russell, H. Maring, 2003: Evaluation of the Moderate-Resolution Imaging Spectroradiometer (MODIS) retrievals of dust aerosol over the ocean during PRIDE. *J. Geophys. Res.*, **108**, 8594, doi: 10.1029/2002JD002460.

Li, Z., X. Zhao, R. Kahn, M. Mishchenko, L. Remer, K.-H. Lee, M. Wang, I. Laszlo, T. Nakajima, and H. Maring, 2009: Uncertainties in satellite remote sensing of aerosols and impact on monitoring its long-term trend: a review and perspective. *Ann. Geophys.*, **27**, 2755-2770 , doi:10.5194/angeo-27-2755-2009.

Lin, J. C., T. Matsui, R. A. Pielke, Sr., C. Kummerow, 2006: Effects of biomass-burning-derived aerosols on precipitation and clouds in the Amazon Basin: a satellite-based empirical study. *J. Geophys. Res.*, **111**, D19204 , doi:10.1029/2005JD 006884.

Liousse, C., B. Guillaume, J. M. Grégoire, M. Mallet, C. Galy, V. Pont, A. Akpo, M. Bedou, P. Castéra, L. Dungall, E. Gardrat, C. Granier, A. Konaré,F. Malavelle, A. Mariscal, A. Mievill, R. Rosset, D. Serça, F. Solmon, F. Tummon, E. Assamoi, V. Yoboué, and P. Van Velthoven, 2010: Updated African biomass burning emission inventories in the framework of the AMMA-IDAF program, with an evaluation of combustion aerosols, *Atmos. Chem. Phys.*, **10**, 9631-9646, doi:10.5194/acp-10-9631-2010.

Liu, C. and E. J. Zipser, 2008: Diurnal cycles of precipitation, clouds, and lightning in the tropics from 9 years of TRMM observations, *Geophys. Res. Lett.*, **35**, L04819, doi:10.1029/2007GL032437.

Liu, C., E. J. Zipser, D. J. Cecil, S. W. Nesbitt, and S. Sherwood, 2008: A cloud and precipitation feature database from 9 years of TRMM observations. *J. Appl. Meteor. Climate*, **47**, 2712-2728. doi:10.1175/2008JAMC1890.1.

Liu, C., E. J. Zipser, G.G. Mace, and S. Benson, 2008: Implications of the differences between daytime and nighttime CloudSat observations over the tropics. *J. Geophys. Res.*, **113**, D00A04, doi:10.1029/2008JD009783.

Liu, C., E. J. Zipser, 2009: "Warm Rain" in the Tropics: Seasonal and Regional Distributions Based on 9 yr of TRMM Data. *J. Climate*, **22**, 767–779. doi: 10.1175/2008JCLI2641.1.

Liu, C., D. J. Cecil, E. J. Zipser, K. Kronfeld, and R. Robertson, 2012: Relationships between lightning flash rates and radar reflectivity vertical structures in thunderstorms over the tropics and subtropics. *J. Geophys. Res.*, **117**, doi:10.1029/2011JD017123.

Luo, Z., G. Y. Liu, and G. L. Stephens, 2008: CloudSat adding new insight into tropical penetrating convection, *Geophys. Res. Lett.*, **35**, L19819, doi:10.1029/2008 GL035330.

Luo, Z., G. Y. Liu, G. L. Stephens, and R. H. Johnson, 2009: Terminal versus transient cumulus congestus: A CloudSat perspective, *Geophys. Res. Lett.*, **36**, L05808, doi:10.1029/2008GL036927.

Mace, G. G., R. Marchand, Q. Zhang, and G. Stephens, 2007: Global hydrometeor occurrence as observed by CloudSat: Initial observations from summer 2006, *Geophys. Res. Lett.*, **34**, L09808, doi:10.1029/2006GL029017.

Malkus, J. S. and Riehl, H., 1964: Cloud structure and distributions over the tropical Pacific Ocean. *Tellus*, **16**: 275–287. doi:10.1111/j.2153-3490.

Marchand, R., G. Mace, T. Ackerman, G. Stephens, 2008: Hydrometeor Detection Using CloudSat- An Earth-Orbiting 94-GHz Cloud Radar, *J. Atmos. Oceanic Technol.*, **25**, 519-533, doi:10.1175/2007JTECHA1006.1

Massie, S. T., A. Heymsfeld, C. Schmitt, D. Muller, and P. Seifert, 2007: Aerosol indirect effects as a function of cloud top pressure. *J. Geophys. Res.*, **112**, D06202, doi:10.1029/2006JD007383.

Morrison, H. and W. W. Grabowski, 2011: Cloud-system resolving model simulations of aerosol indirect effects on tropical deep convection and its thermodynamic environment, *Atmos. Chem. Phys. Discuss.*, **11**, 15573-15629, doi:10.5194/acpd-11-15573-2011.

Nakajima T, Higurashi A, Kawamoto K, Penner JE, 2001: A possible correlation between satellite-derived cloud and aerosol microphysical parameters. *Geophys Res Lett* **28**,1171–1174. doi:10.1029/2000GL012186.

Nesbitt, S. W., E. J. Zipser, and D.J. Cecil, 2000: A Census of Precipitation Features in the Tropics Using TRMM: Radar, Ice Scattering, and Lightning Observations. *J. Climate*, **13**, 4088-4106. doi:10.1175/1520-0442(2000)013<4087:ACOPFI>2.0.CO;2.

Niu, F. and Z. Li, 2011: Cloud invigoration and suppression by aerosols over the tropical region based on satellite observations. *Atmos. Chem. Phys. Discuss.*, **11**, 5003-5017 , doi:10.5194/ acpd-11-5003-2011.

Rangno, A. L. and Hobbs, P. V., 2005: Microstructures and precipitation development in cumulus and small cumulonimbus clouds over the warm pool of the tropical Pacific Ocean. *Q.J.R. Meteorol. Soc.*, **131**, 639–673. doi: 10.1256/qj.04.13

Raymond, David J., Alan M. Blyth, 1986: A Stochastic Mixing Model for Nonprecipitating Cumulus Clouds. *J. Atmos. Sci.*, **43**, 2708–2718. doi:10.1175/1520-0469(1986)043<2708:ASMMFN>2.0.CO;2

Redelsperger, J-L., D. B. Parsons, F. Guichard, 2002: Recovery Processes and Factors Limiting Cloud-Top Height following the Arrival of a Dry Intrusion Observed during TOGA COARE. *J. Atmos. Sci.*, **59**, 2438–2457, doi:10.1175/1520-0469(2002)059.

Remer, L. A., Y. J. Kaufman, D. Tanré, S. Mattoo, D. A. Chu, J. V. Martins, R.-R. Li, C. Ichoku, R. C. Levy, R. G. Kleidman, T. F. Eck, E. Vermote, and B. N. Holben, 2005: The MODIS Aerosol Algorithm, Products, and Validation. *J. Atmos. Sci.*, **62**, 947–973, doi:10.1175/JAS3385.1.

Remer L., D. Tanré, and Y. J. Kaufman, 2006: Algorithm for remote sensing of tropospheric aerosols from MODIS: Collection 5 Product (MOD02) Algorithm Theoretical Basis Document, http://modis.gsfc.nasa.gov/data/atbd/atbd_mod02.pdf, accessed 2012.

Remer, L. A., R. G. Kleidman, R C. Levy, Y. J. Kaufman, D. Tanré, S. Mattoo, J. V. Martins, C. Ichoku, I Koren, H. Yu, B. N. Holben, 2008: Global aerosol climatology from the MODIS satellite sensors, *J. Geophys. Res.*, **113**, D14S07, doi:10.1029/2007JD009661.

Riley, E. M., *and* B. E. Mapes 2009*:* Unexpected peak near −15°C in CloudSat echo top climatology, Geophys. Res. Lett., 36, *L09819, doi:* 10.1029/2009GL037558.

Riley, E. M., B. E. Mapes, S. N. Tulich, 2011: Clouds Associated with the Madden–Julian Oscillation: A New Perspective from CloudSat. *J. Atmos. Sci.*, **68**, 3032–3051. doi: 10.1175/JAS-D-11-030.1.

Robe, F. R., K. A. Emanuel, 2001: The Effect of Vertical Wind Shear on Radiative–Convective Equilibrium States. *J. Atmos. Sci.*, **58**, 1427–1445. doi: 10.1175/1520-0469(2001)058<1427:TEOVWS>2.0.CO;2.

Robinson, F. J., S. C. Sherwood, D. Gerstle, C. Liu, D. J. Kirshbaum, 2011: Exploring the Land–Ocean Contrast in Convective Vigor Using Islands. *J. Atmos. Sci.*, **68**, 602–618, doi:10.1175/2010JAS3558.1.

Rosenfeld, D., 1999: TRMM observed first direct evidence of smoke from forest fires inhibiting rainfall. *Geophys. Res. Lett.*, **26**, 3105–3108 , doi:10.1029/1999GL006066.

Rosenfeld, D., and I. M. Lensky, 1998: Satellite-based insights into precipitation formation processes in continental and maritime convective clouds. *Bull. Amer. Meteor. Soc.*, **79**, 2457–2476, doi:10.1175/1520-0477(1998)079<2457:SBIIPF>2.0.CO;2.

Rosenfeld, D., and G. Feingold, 2003: Explanation of the discrepancies among satellite observations of the aerosol indirect effects, *Geophys. Res. Lett.*, **30(14)**, 1776, doi: 10.1029/2003GL017684.

Rosenfeld, D., et al., 2007b. The Chisholm firestorm: observed microstructure, precipitation and lightning activity of a pyro-cumulonimbus. *Atmos. Chem. Phys.* 7, 645–659. doi: 10.1016/j.earscirev.2008.03.001.

Rosenfeld, D., U. Lohmann, G. Raga, C. O'Dowd, M. Kulmala, S. Fuzzi, A. Reissell, M. Andreae, 2008: Floor or drought: How do aerosols affect precipitation?, Science, 321, 1309, doi:10.1126/ science.1160606.

Rossow, W. B., R.A. Schiffer, 1991: ISCCP Cloud Data Products. Bull. Amer. Meteor. Soc., 72, 2–20, doi: 10.1175/1520-0477(1991)072.

Rotunno, R., J. B. Klemp, and M. L. Weisman, 1988: A theory for strong, long-lived squall lines. *J. Atmos. Sci.*, **45**, 463–485. doi: 10.1175/1520-0469(1988)045<0463:ATFSLL>2.0.CO;2.

Salomonson, V. V., W. L. Barnes, P.W. Maymon, H. E. Montgomery, and H. Ostrow, 1989: MODIS: Advanced facility instrument for studies of the earth as a system. *IEEE Trans. Geosci. Remote Sens.*,**27**,145–153. doi: 10.1109/36.20292.

Schumacher, C., R. A. Houze, 2003: The TRMM Precipitation Radar's View of Shallow, Isolated Rain. *J. Appl. Meteor.*, **42**, 1519–1524, doi:10.1175/1520-0450(2003)042.

Schumacher, C., M. H. Zhang, P. E. Ciesielski, 2007: Heating Structures of the TRMM Field Campaigns. *J. Atmos. Sci.*, **64**, 2593–2610. doi:10.1175/JAS3938.1

Seifert, A., and K. D. Beheng, 2006: A two-moment cloud microphysics parameterization for mixed-phase clouds. Part 2: Maritime vs continental deep convective storms. Meteor. Atmos. Phys., **92**, 67–82, , doi:10.1007/s00703-005-0113-3.

Seigel, R. B. and S. C. van den Heever, 2012: Dust Lofting and Ingestion by Supercell Storms. *J. Atmos. Sci.*, **69**, 1453-1473. doi: 10.1175/JAS-D-11-0222.1.

Seinfeld, J. H. and S. N. Pandis, 1998: *Atmospheric Chemisty and Physics.* Wiley-Interscience Publishing, 1326 pp.

Sekiguchi, M., T. Nakajima, K. Suzuki, K. Kawamoto, A. Higurashi, D. Rosenfeld, I. Sano, and S. Mukai, 2003: A study of the direct and indirect effects of aerosols using global satellite data sets of aerosols and cloud parameters. *J. Geophys. Res.*, **108**, D22, doi:10.1029/2002JD003359.

Sheffield, A. M., S. C. van den heever, and S. M. Saleeby, 2013: Growth of cumulus congestus clouds when impacted by aerosols. *J. Atmos. Sci.*, in review.

Silva Dias, M. A. F., and Coauthors, 2002: Cloud and rain processes in a biosphere–atmosphere interaction context in the Amazon region. *J. Geophys. Res.*, **107**, 8072, doi:10.1029/2001JD000335.

Simmons, A., Uppala, S., Dee, D., & Kobayashi, S. (2007). ERA-Interim: New ECMWF reanalysis products from 1989 onwards. *ECMWF newsletter*, *110*, 25-35.

Squires, P., 1956: The microstructure of cumuli in maritime and continental air. *Tellus*, **8**, 443–444. doi: 10.1111/j.2153-3490.1956.tb01246.x.

Stephens, G. L., and Coauthors, 2002: The CloudSat Mission and the A-Train. *Bull. Amer. Meteor. Soc.*, **83,** 1771–1790. doi:10.1175/BAMS-83-12-1771.

Stephens, G. L., N. B. Wood, 2007: Properties of Tropical Convection Observed by Millimeter-Wave Radar Systems. *Mon. Wea. Rev.*, **135**, 821–842, doi: 10.1175/MWR3321.1.

Stevens, B. and G. Feingold, 2009: Untangling aerosol effects on clouds and precipitation in a buffered system. *Nature*, **461**, 607-613. doi: 10.1038/nature08281.

Storer, R. L., S. C. van den Heever, G. L. Stephens, 2010: Modeling Aerosol Impacts on Convective Storms in Different Environments. *J. Atmos. Sci.*, **67**, 3904–3915. doi: 10.1175/2010JAS3363.1.

Storer, R.L., S.C. van den Heever, and T.L. L'Ecuyer, 2013: Aerosol induced convective invigoration observed in the tropical East Atlantic. In review.

Storer, R. L., S. C. van den Heever, 2013: Microphysical Processes Evident in Aerosol Forcing of Tropical Deep Convective Clouds. *J. Atmos. Sci.*, **70**, 430–446. doi: 10.1175/JAS-D-12-076.1

Takayabu, Y. N., S. Shige, W.-K. Tao, N. Hirota, 2010: Shallow and Deep Latent Heating Modes over Tropical Oceans Observed with TRMM PR Spectral Latent Heating Data. *J. Climate*, **23**, 2030–2046. doi: 10.1175/2009JCLI3110.1

Takemi, T., O. Hirayama, and C. Liu, 2004:, Factors responsible for the vertical development of tropical oceanic cumulus convection, *Geophys. Res. Lett.*, **31**, L11109, doi:10.1029/2004GL020225.

Tanré, D., Y. J. Kaufman, M. Herman, and S. Mattoo, 1997: Remote sensing of aerosol properties over oceans using the MODIS/EOS spectral radiances, *J. Geophys. Res.*, **102**, 16971–16988. doi:10.1029/96JD03437.

Tao, W. K., 2007: Cloud resolving modeling. *J. Met. Soc. Japan*, **85B**, 305-330., doi:10.2151/jmsj.85B.305.

Tao, W.-K., J.-P. Chen, Z. Li, C. Wang, and C. Zhang, 2012: Impact of Aerosols on Convective Clouds and Precipitation, *Rev. Geophys.*, doi:10.1029/2011RG 000369, in press.

Toracinta, E. R., D. J. Cecil, E. J. Zipser, S. W. Nesbitt, 2002: Radar, Passive Microwave, and Lightning Characteristics of Precipitating Systems in the Tropics. *Mon. Wea. Rev.*, **130**, 802-824. doi: http://10.1175/1520-0442(2000)013<4087:ACOPFI>2.0 .CO;2.

Twomey, S., T. A. Wojciechowski, 1969: Observations of the Geographical Variation of Cloud Nuclei. *J. Atmos. Sci.*, **26**, 648–651, doi: 10.1175/1520-0469.

Twomey, S., 1977: The influence of pollution on the short wave albedo of clouds, J. *Atmos. Sci.*, **34**, 1149–1152, doi:10.1175/ 1520-0469(1977)034<1149:TIOPOT >2.0.CO;2.

van den Heever, S. C., G. G. Carrio´ , W. R. Cotton, P. J. DeMott, and A. J. Prenni, 2006: Impacts of nucleating aerosol on Florida storms. Part I: Mesoscale simulations. *J. Atmos. Sci.*, **63**, 1752–1775, doi:10.1175/JAS3713.1.

van den Heever, S. C., W. R. Cotton, 2007: Urban Aerosol Impacts on Downwind Convective Storms. *J. Appl. Meteor. Climatol.*, **46**, 828–850. doi: 10.1175/JAM2492.1

van den Heever, S., G. L. Stephens, and N. B. Wood, 2011: Aerosol indirect effects on tropical convection characteristics under conditions of radiative-convective equilibrium. *J. Atmos. Sci.*, **68**, 699-718 , doi:10.1175/2010JAS3603.1.

Waite, M. L., B. Khouider, 2010: The Deepening of Tropical Convection by Congestus Preconditioning. *J. Atmos. Sci.*, **67**, 2601–2615. doi: 10.1175/2010JAS3357.1.

Williams, E. R., D. Rosenfeld, N. Madden, C. Labrada, J. Gerlach, and L. Atkinson, 1999: The role of boundary layer aerosol in the vertical development of precipitation and electrification: Another look at the contrast between lightning over land and over ocean. *Proc. 11th Int. Conf. on Atmospheric Electricity,* Huntsville, AL, NASA, 754–757.

Yang, G.-Y, and J. Slingo, 2001: The diurnal cycle in the tropics, *Mon. Wea. Rew.*, **129**, 784-801, doi:10.1175/1520-0493(2001)129<0784:TDCITT>2.0.CO;2.

Yu, H., R. E. Dickinson, M. Chin, Y. J. Kaufman, B. N. Holben, I. V. Geogdzhayez, M. I. Mishchenko, 2003: Annual cycle of global distribution of aerosol optical depth from integration of MODIS retrievals and GOCART model simulations. *Geophys. Res. Lett.*, **108**, NO. D3, 4128, doi:10.1029/2002JD002717.

Yuan, T., L. A. Remer, K. E. Pickering, and H. Yu, 2011: Observational evidence of aerosol enhancement of lightning activity and convective invigoration, *Geophys. Res. Lett.*, **38**, L04701, doi:10.1029/2010GL046052.

Zipser, E. J., M. A. LeMone, 1980: Cumulonimbus Vertical Velocity Events in GATE. Part II: Synthesis and Model Core Structure. *J. Atmos. Sci.*, **37**, 2458–2469 doi: 10.1175/1520-0469(1980)037.

Zipser, E. J., K. R. Lutz, 1994: The Vertical Profile of Radar Reflectivity of Convective Cells: A Strong Indicator of Storm Intensity and Lightning Probability?. *Mon. Wea. Rev.*, **122**, 1751–1759. doi: 10.1175/1520-0493(1994)122<1751: TVPORR>2.0.CO;2.

Zipser, E. J., 2003: Some Views On "Hot Towers" after 50 Years of Tropical Field Programs and Two Years of TRMM Data. *Meteorological Monographs*, **29**, 49–58. doi: 10.1175/0065-9401(2003)029<0049:CSVOHT>2.0.CO;2.